



УНИВЕРЗИТЕТ У НОВОМ САДУ
ФАКУЛТЕТ ТЕХНИЧКИХ НАУКА У
НОВОМ САДУ



Slobodan Dražić

**Shape Based Methods for Quantification
and Comparison of Object Properties
from Their Digital Image Representations**

DOCTORAL DISSERTATION

Слободан Дражић

**Методе засноване на облику за
квантитативни опис и поређење
облика објеката приказаних
дигиталним сликама**

ДОКТОРСКА ДИСЕРТАЦИЈА


Нови Сад, 2018



УНИВЕРЗИТЕТ У НОВОМ САДУ • ФАКУЛТЕТ ТЕХНИЧКИХ НАУКА
21000 НОВИ САД, Трг Доситеја Обрадовића 6

КЉУЧНА ДОКУМЕНТАЦИЈСКА ИНФОРМАЦИЈА

Редни број, РБР :	
Идентификациони број, ИБР :	
Тип документације, ТД :	Монографска документација
Тип записа, ТЗ :	Текстуални штампани запис
Врста рада, ВР :	Докторска дисертација
Аутор, АУ :	Слободан Дражић
Ментор, МН :	Проф. др Јоаким Линдبلاد и проф. др Тибор Лукић
Наслов рада, НР :	Методе засноване на облику за квантитативни опис и поређење облика објеката приказаних дигиталним сликама
Језик публикације, ЈП :	Енглески
Језик извода, ЈИ :	Српски, енглески
Земља публикавања, ЗП :	Република Србија
Уже географско подручје, УГП :	
Година, ГО :	2018
Издавач, ИЗ :	Ауторски репринт
Место и адреса, МА :	Нови Сад, Факултет техничких наука, Трг Доситеја Обрадовића 6
Физички опис рада, ФО : (поглавља/страна/ цитата/табела/слика/графика/прилога)	5/126/136/5/59/15/0
Научна област, НО :	Примењена математика
Научна дисциплина, НД :	Рачунарска обрада слика
Предметна одредница/Кључне речи, ПО :	Рачунарска обрада слика, анализа облика, дескриптор, Фереов дијаметар, математичка морфологија, растојања, морфолошка растојања
УДК	
Чува се, ЧУ :	Библиотеци Факултета техничких наука, Трг Доситеја Обрадовића 6, Нови Сад
Важна напомена, ВН :	
Извод, ИЗ :	У тези су размотрени развој, побољшање и евалуација метода за квантитативну карактеризацију објеката приказаних дигиталним сликама, као и мере растојања између дигиталних слика. Методе за квантитативну карактеризацију објеката представљених дигиталним сликама се све више користе у применама у којима грешка може имати критичне последице, а традиционалне методе за квантитативну карактеризацију су мале прецизности и тачности. У тези се показује да се коришћењем информације о покривеност пиксела обликом може значајно побољшати прецизност и тачност оцене растојања између две најудаљеније тачке облика мерено у датом правцу. Веома је пожељно да мера растојања између дигиталних слика може да се веже за одређену особину облика и морфолошке операције се користе приликом дефинисања растојања у ту сврху. Ипак, растојања дефинисана на овај начин показују се недовољно осетљива на релевантне податке дигиталних слика који представљају особине облика. У тези се показује да идеја адаптивне математичке морфологије може успешно да се користи да би се превазишао поменути проблем осетљивости растојања дефинисаних користећи морфолошке операције.
Датум прихватања теме, ДП :	28.12.2017
Датум одбране, ДО :	

	УНИВЕРЗИТЕТ У НОВОМ САДУ • ФАКУЛТЕТ ТЕХНИЧКИХ НАУКА 21000 НОВИ САД, Трг Доситеја Обрадовића 6	
	КЉУЧНА ДОКУМЕНТАЦИЈСКА ИНФОРМАЦИЈА	

Чланови комисије, КО:	Председник:	др Татјана Давидовић, научни саветник	
	Члан:	др Љиљана Теофанов, ванредни професор	
	Члан:	др Лидија Чомић, доцент	Потпис ментора
	Члан, ментор:	др Јоаким Линдблад, истраживач	
	Члан, ментор:	др Тибор Лукић, ванредни професор	

Образац Q2.НА.06-05- Издање 1

Accession number, ANO :	
Identification number, INO :	
Document type, DT :	Monographic publication
Type of record, TR :	Textual printed material
Contents code, CC :	PhD thesis
Author, AU :	Slobodan Dražić
Mentor, MN :	Prof. dr Joakim Lindblad and prof. dr Tibor Lukić
Title, TI :	Shape Based Methods for Quantification and Comparison of Object Properties from Their Digital Image Representations
Language of text, LT :	English
Language of abstract, LA :	Serbian, English
Country of publication, CP :	Republic of Serbia
Locality of publication, LP :	
Publication year, PY :	2018
Publisher, PB :	Author's reprint
Publication place, PP :	Novi Sad, Faculty of Technical Sciences, Trg Dositeja Obradovića 6
Physical description, PD : <small>(chapters/pages/ref./tables/pictures/graphs/appendixes)</small>	5/126/136/5/59/15/0
Scientific field, SF :	Applied Mathematics
Scientific discipline, SD :	Digital image processing
Subject/Key words, S/KW :	Digital image processing, shape analysis, descriptor, Feret' s diameter, mathematical morphology, distances, morphological distances
UC	
Holding data, HD :	Library of the Faculty of Technical Sciences, Trg Dositeja Obradovića 6, Novi Sad
Note, N :	



УНИВЕРЗИТЕТ У НОВОМ САДУ **ФАКУЛТЕТ ТЕХНИЧКИХ НАУКА**
21000 НОВИ САД, Трг Доситеја Обрадовића 6

КЉУЧНА ДОКУМЕНТАЦИЈСКА ИНФОРМАЦИЈА

Abstract, AB:	The thesis investigates development, improvement and evaluation of methods for quantitative characterization of objects from their digital images and similarity measurements between digital images. Methods for quantitative characterization of objects from their digital images are increasingly used in applications in which error can have critical consequences, but the traditional methods for shape quantification are of low precision and accuracy. In the thesis is shown that the coverage of a pixel by a shape can be used to highly improve the accuracy and precision of using digital images to estimate the maximal distance between objects furthest points measured in a given direction. It is highly desirable that a distance measure between digital images can be related to a certain shape property and morphological operations are used when defining a distance for this purpose. Still, the distances defined in this manner turns out to be insufficiently sensitive to relevant data representing shape properties in images. We show that the idea of adaptive mathematical morphology can be used successfully to overcome problems related to sensitivity of distances defined via morphological operations when comparing objects from their digital image representations.		
Accepted by the Scientific Board on, ASB:	December 28, 2017		
Defended on, DE:			
Defended Board, DB:	President:	dr Tažana Davidović, research professor	
	Member:	dr Ljiljana Teofanov, associate professor	
	Member:	dr Lidia Čomić, assistant professor	Menthor's sign
	Member, Mentor:	dr Joakim Lindblad, researcher	
	Member, Mentor:	dr Tibor Lukić, associate professor	

Образец **Q2.HA.06-05** - Izdanje 1

Svoj naučni rad posvećujem svom ocu.

Neizmernu zahvalnost dugujem Jani, Svetlani i deda Sveti.

Rezime

Slike objekata već dugo vremena nisu samo način za predstavljanje svetlosti koja se reflektuje od njihove površine, već pružaju mogućnost za izdvajanje, opisivanje i evaluaciju mnogih osobina objekata koji su slikama predstavljeni. Upečatljiv primer za to su rendgenske slike koje nisu samo korisne u istraživanju objekata, već otkako ih je 1895. prvi put sistematski predstavio Vilhem Rendgen, omogućuju istraživanje na jedan efikasan način koji nije bio moguć pre njihovog otkrića.

Mogućnost da se slikama obuhvate osobine objekata važne za njihovo istraživanje nameću mnoge probleme koji su vezani za izdvajanje, vizualizaciju i manipulaciju takvim osobinama na osnovu slika. Nakon pojave računarske tehnologije u Drugom svetskom ratu intenzivno se istražuju mogućnosti da se slike obrađuju računarski. Ovo istraživanje rezultuje 1957. godine nastankom računara pod nazivom "Standard Eastern Automatic Computer" ili "SEAC" koji može biti programiran, a istovremeno omogućuje da se slike pohranjuju u njegovu memoriju. Na ovaj način nastaje nova naučna oblast pod nazivom *digitalna obrada slike*, tj. obrada slike digitalnim računarima. Računari nastavljaju snažno da se razvijaju posle svog nastanka, a taj razvoj se neće zaustaviti u budućnosti. Istovremeno, snažno se razvijaju i uređaji za dobijanje slike. Digitalna kamera, magnetna rezonanca i CT skener su samo neki pojmovi koji su sastavni deo svakodnevnog života. Ovakvi uređaji obezbeđuju sve verodostojnije predstavljanje sve raznovrsnijih objekata u sve različitijim uslovima. Sve navedeno uzrokovalo je prodor digitalne obrade slike u skoro sva naučna polja, a izučavanje objekata na osnovu njihovih slika postalo je standardna procedura u naučnom istraživanju.

Da bi se razmatrale osobine objekata na osnovu slika, ona se može posmatrati kao signal, tj. kao promena jedne ili više veličina (najčešće energije koja potiče od elektromagnetnog zračenja) koja nosi neku informaciju. Zbog toga se slika često i modeluje na isti način kao signal, tj. kao realna funkcija: $f : D \rightarrow \mathbb{R}$, $D \subset \mathbb{R}^n$, gde su $(x_1, x_2, \dots, x_n) \in D$ prostorne koordinate, a $f(x_1, x_2, \dots, x_n)$ izražava količinu energije koja se apsorbuje ili reflektuje u tački $\mathbf{x}(x_1, x_2, \dots, x_n)$ [36]. Domen D je ograničen jer se samo ograničeni deo prostora može predstaviti slikom, a skup intenziteta je ograničen jer se može koristiti samo ograničena količina zračenja u procesu dobijanja slike.

Digitalne slike

Nakon dobijanja slike, obrada slike računarom je nerazdvojiva od dodatnog gubitka informacija o objektima budući da računar može da obrađuje samo binarne podatke. Proces prevođenja slike u podatke koji se mogu zapisati putem binarnog zapisa naziva se digitalizacija. Nakon digitalizacije i domen i skup vrednosti postaju konačni skupovi budući da su ograničeni i diskretni. Slika čija funkcija ima konačan domen i konačan skup vrednosti naziva se *digitalna slika*.

Da bi se diskretizovao domen, prostorne koordinate slike se najčešće aproksimiraju vrednostima koje su pravilno raspoređene u digitalnoj rešetki. Broj takvih, uzorkovanih vrednosti po jedinici se naziva *prostorna rezolucija*. Svaka tačka rešetke nakon uzorkovanja predstavlja deo prostora koji se sastoji od svih tačaka bližih njoj nego bilo kojoj drugoj tački rešetke. Takav deo prostora naziva se *Voronoi oblast* date tačke po Georgiju Feodoševiču Voronoju (1868-1908) koji je dao neprocenjiv doprinos teoriji regularnih podela prostora. U digitalnoj obradi slike, Voronoi oblasti koje odgovaraju tačkama rešetke se nazivaju pikseli za dvodimenzionalne slike, *vokseli* za trodimenzionalne slike ili *spelovi* u opštem slučaju. Slično kao prostorne koordinate, tokom digitalizacije, vrednosti intenziteta najčešće uzimaju vrednosti pravilno raspoređene u unapred utvrđenom intervalu $[a, b] \subseteq \mathbb{R}$. Taj proces se naziva *kvantizacija*. Broj vrednosti koje funkcija slike može uzeti po jedinici naziva se *rezolucija sivih vrednosti*.

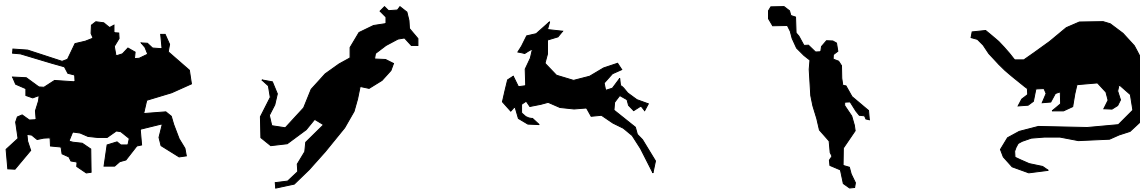
Poređenje objekata na osnovu njihovih digitalnih slika

Jedan od fundamentalnih postupaka nad objektima koji se pojavljuju na slikama je njihovo poređenje. Neki referentan objekat se poredi sa drugima za probleme identifikacije i prepoznavanja. Objekti se porede jedan sa drugim za problem klasifikacije. Jedan objekat može se porediti sa samim sobom u različitim vremenskim trenucima da bi se pratile promene u njegovom položaju ili obliku. Broj primena poređenja objekata je daleko veći i ovo su samo neki od primera.

U zavisnosti od količine podataka koji se koriste, poređenje objekata na osnovu njihovih digitalnih slika može se vršiti na dva načina. Kada je to moguće, jeftinije je sa aspekta angažovanja računarskih resursa da se porede samo neke osobine objekata, nego kompletni podaci digitalnih slika koji ih predstavljaju. Da bi se to postiglo, često se samo takve, pogodne, osobine izdvajaju iz digitalnih slika i koriste u daljoj obradi. Ukoliko se neka osobina oblika može opisati brojem, tj. kvantifikovati, pretpostavlja se da je poređenje na osnovu nje jednostavno i ne zahteva veliku računarsku snagu. Postoje situacije u kojima objekti moraju biti poređeni direktnim poređenjem njihovih digitalnih slika. To je uobičajeno kada su kompletni podaci bitni za razmatranje i kada izdvajanje samo nekih osobina vodi do gubljenja elementarnih informacija.

Oblik

U obradi slike, formalna definicija oblika ne postoji. Oblik je osnovno svojstvo svakog objekta, kao boja ili tekstura. Uvek je predstavljen ograničenim skupom tačaka sa koordinatama iz \mathbb{R}^n koji izdvaja geometrijski sadržaj objekta od svih drugih osobina. Oblik je invarijantan u odnosu sa translaciju, rotaciju, (uniformno) skaliranje i osnu simetriju. Zbog toga se može posmatrati i kao klasa ekvivalencije u odnosu na transformacije sličnosti u skupu svih objekata [105]. Često se posmatra i kao silueta nekog objekta. U literaturi se takođe navodi i kao oblast. Primeri nekih planarnih oblika dati su na Slici 1.



Slika 1: Primeri oblika realnih objekata.

Opis problema

Metode za kvantitativnu karakterizaciju objekata na osnovu njihovih digitalnih slika se sve više koriste u svrhe u kojima greška može imati kritične posledice kao što su medicinske slike ili autonomna kontrola vozila. Budući da se koriste samo konačni skupovi podataka da bi se kvantifikovali stvarni objekti, ove metode često u proseku *precenjuju* ili *potcenjuju* tačne vrednosti. Time nastaje određeno odstupanje od prave, tačne, vrednosti koje se naziva *pristrasnost* metoda. Od velikog je značaja da je pristrasnost mala, odnosno da metod ima veliku *tačnost* i da u ponovnim, višestrukim, primenama pod nepromenjenim uslovima isti metod daje vrednosti koje su blizu jedna druge, tj. da ima veliku *preciznost*. Dakle, tačnost metoda odnosi se na to koliko je rezultat nekog metoda u proseku blizak tačnoj vrednosti, a preciznost se odnosi na to koliko se vrednosti rezultata rasipaju prilikom ponavljanja metoda u nepromenjenim uslovima.

Veoma često korišćena osobina za kvantitativnu karakterizaciju objekata je rastojanje između njegove dve najudaljenije tačke mereno u datom pravcu. Takvo rastojanje naziva se *Fereov dijametar* objekta. Estimacija Fereovog dijametra iz digitalnih slika pripada tradicionalnim metodama koje se izvršavaju na binarnim slikama čije vrednosti mogu biti samo 0 ili 1. Prilikom diskretizacije vrednost 1 se dodeljuje spelovima koji odgovaraju uzorkovanim tačkama koje pripadaju unutrašnjosti ili rubu objekta, a vrednost 0 spelovima koji odgovaraju uzorkovanim

tačkama koje pripadaju spoljašnjosti objekta. Na taj način, spelovi su grubo podeljeni na one koji predstavljaju objekat i one koji predstavljaju njegovu pozadinu. Pretpostavka da je spel ili deo objekta ili njegove pozadine uzrokuje nedostatak preciznosti i tačnosti metoda jer su spelovi oblasti i mogu delom biti u unutrašnjosti, a delom u spoljašnjosti.

Kada se porede kompletni podaci digitalne slike koriste se mere rastojanja. Veoma je poželjno da se neka mera rastojanja između digitalnih slika može vezati za određenu osobinu oblika objekata koji se upoređuju. Da bi se izdvojile relevantne geometrijske strukture iz neke slike koriste se morfološke operacije *dilatacije* i *erozije*. Prilikom dilatacije digitalne slike svakom spelu se dodeljuje maksimalna vrednost u nekoj njegovoj okolini. Pre dodeljivanja maksimalne vrednosti, intenziteti slike u okolini mogu se povećati. Okolina spela koja se posmatra tokom dilatacije naziva se *ravan strukturni element*, a povećanje u okolini je definisano *neravnin strukturnim elementom* ili *strukturnom funkcijom*. Ravan strukturni element, kao i strukturna funkcija mogu biti *rigidni* ako su isti za sve spelove digitalne slike ili *adaptivni* ukoliko menjaju svoj oblik ili vrednosti u zavisnosti od spela. *Erozija* je operacija slična dilataciji, ali se dodeljuje minimalna vrednost umesto maksimalne i umesto da strukturna funkcija povećava vrednosti u okolini, ona ih smanjuje. Morfološke operacije dilatacije i erozije koriste se prilikom definisanja rastojanja da bi ona bila vezana za određenu osobinu oblika objekata. Rastojanja definisana na ovakav način u digitalnoj obradi slike nazivaju se *morfološka rastojanja*.

Postojeća morfološka rastojanja zasnivaju se na upotrebi ravnog, rigidnog strukturnog elementa i imaju brojne nedostatke. Uopšteno govoreći, ona su nedovoljno osetljiva na relevantne podatke digitalne slike koji predstavljaju oblik.

Cilj teze

Pored toga što ima veliku moć diskriminacije između objekata, oblik ima i velik broj osobina koje se mogu izraziti brojem i zbog toga je od ključnog značaja prilikom poređenja objekata. Ipak, podaci koje pružaju digitalne slike ne koriste se u potpunosti kada se vrši poređenje objekata na osnovu oblika i ima prostora za poboljšanje. Ovo je uzrok opisanih problema vezanih za preciznost i tačnost kvantitativne karakterizacije objekata i neosetljivost morfoloških rastojanja. Glavni cilj teze je razvoj i unapređenje metoda zasnovanih na obliku koji koriste digitalne slike za poređenje objekata da bi se bolje iskoristili podaci koji su na raspolaganju i prevazišli opisani problemi.

Pregled sadržaja i strukture teze

Teza je podeljena na pet poglavlja. U uvodnom poglavlju opisan je predmet, cilj i značaj istraživanja. U drugom poglavlju je dato više detalja o pojmovima,

metodama i modelima koji se u tezi koriste. Treće poglavlje istražuje ocenu Fereovog dijametra iz digitalnih slika, a četvrto izračunavanje morfoloških rastojanja između digitalnih slika. U petom poglavlju dat je zaključak teze i diskusija rezultata, kao i pravci budućeg istraživanja.

Drugo poglavlje

Pregled U poglavlju 2.1 je dat pregled i značaj analize oblika kao oblasti. U poglavlju 2.2 su opisani tradicionalni modeli za predstavljanje oblika digitalnim slikama. Model zasnovan na pokrivenosti svakog spela oblikom dat je u poglavlju 2.3. Kratak pregled matematičke morfologije kao oblasti i njenih osnovnih pojmova koji se u tezi koriste dati su u poglavlju 2.4. Rastojanja koja se često koriste u obradi slike i koja se u tezi razmatraju data su u poglavlju 2.5.

Da bi se neka osobina oblika mogla kvantifikovati, najpre se sam oblik mora izdvojiti od ostalih komponenata digitalne slike. Takav postupak izdvajanja vrši se najčešće na osnovu homogenosti spelova koji predstavljaju objekat i njihovim različitostima od spelova koji predstavljaju ostale komponente i naziva se *segmentacija slike*. Pregledi raznih metoda za segmentaciju dati su u [6, 32, 80, 104].

Postupak *analize oblika* najčešće počinje *reprezentacijom*. Reprezentacija oblika podrazumeva dalje uprošćavanje podataka dobijenih segmentacijom. Rezultat je višedimenzionalni vektor koji predstavlja oblik tačno ili približno, ali očuvava osobine oblika bitne za dalju obradu. Neke metode za reprezentaciju oblika mogu se pronaći u [53, 86, 95, 133]. Proces kvantifikacije osobina oblika se naziva *deskripcija*, a sama osobina koja se kvantifikuje naziva se *deskriptor*. Na primer, obim i površina su dobro poznate osobine oblika čije izračunavanje iz digitalnih slika je dobro izučeno u literaturi [10, 16, 107, 110], gde se navode kao deskriptori. Budući da se istražuje ocena Fereovog dijametra iz digitalne slike, u tezi se daje njegova formalna definicija. Pored toga, daju se definicije nekih od brojnih deskriptora koji se na osnovu Fereovog dijametra mogu izračunati.

Deskripcija je veoma složen proces, a većina teškoća potiče iz činjenice da treba dati meru stvarnog objekta na osnovu konačnih podataka. Zbog toga analiza oblika pripada *analizi slike*, tj. izdvajanju relevantnih informacija iz digitalne slike. Pregled različitih modela digitalizacije dat je u [117] gde su oni generalizovani na proizvoljnu dimenziju i nazivaju se metodama za uzorkovanje. *Uzorkovanje podskupa* podrazumeva uzimanje u obzir samo tačaka digitalne rešetke koje se nalaze unutar oblika. Uzorkovanje na osnovu *superpokrivenosti* je alternativni metod koji podrazumeva izdvajanje svih tačaka digitalne rešetke čije Voronoi oblasti imaju neprazan presek sa oblikom koji se posmatra. Kada se primenjuje u kvadratnoj digitalnoj rešetki za planarne oblike, uzorkovanje podskupa naziva se *Gausova digitalizacija* po poznatom matematičaru Karlu Fridrihu Gausu (1777-1855) koji ju je koristio za izučavanje oblika. Prva vrsta Gausove digitalizacije podrazumeva da

se razmatra unija svih piksela čiji centri pripadaju skupu koji je uzorkovan, a druga samo tačke digitalne rešetke unutar oblika. Postoje i druge vrste digitalizacije, ali se veoma retko koriste u praksi prilikom poređenja objekata na osnovu oblika.

Da bi se razumeli i formalizovali uslovi za dobre performanse nekog metoda analize oblika, prirodno se nameće pitanje: Koja informacija o obliku je očuvana nakon digitalizacije? Postoji opširna literatura nastala u pokušaju da se odgovori na ovo pitanje [81, 84, 102, 118, 122] i u svim ovim radovima fundamentalnu ulogu ima pojam *R-regularnog skupa*, tj. skupa za čiju svaku tačku ruba postoje dve lopte koje imaju zajedničku tangentu sa skupom u datoj tački (*oskulatorne* lopte). Jedna u unutrašnjosti, a druga u spoljašnjosti skupa. U [118] se uvodi relacija *jake r-sličnosti* za dva skupa $X, Y \subset \mathbb{R}^n$ da bi se dokazala osobina koja obuhvata sve ostale koje se mogu očuvati prilikom digitalizacije i pominju se u literaturi. X i Y su jako r -slični ako postoji homeomorfizam $f : \mathbb{R}^n \rightarrow \mathbb{R}^n$ tako da $\mathbf{x} \in X \Leftrightarrow f(\mathbf{x}) \in Y$ i $\mathbf{x} \in \partial X \Rightarrow |\mathbf{x} - f(\mathbf{x})| \leq r$. U istom radu dokazano je da je R -regularan dvodimenzionalan oblik jako r -sličan sa svojom digitalizacijom dobijenom uzorkovanjem podskupa u bilo kojoj dvodimenzionalnoj rešetki u kojoj je veličina piksela $r < R$.

Relacija *jake r-sličnosti* između nekog dvodimenzionalnog oblika i njegove digitalizacije uzorkovanjem podskupa u bilo kojoj dvodimenzionalnoj rešetki obezbeđuje da konačan skup koji aproksimira oblik konvergira ka obliku kada prostorna rezolucija teži beskonačnosti. Ipak, ovo nije dovoljno da neki deskriptor konvergira ka svojoj tačnoj vrednosti sa povećanjem rezolucije. Zbog toga se istražuje problem *multigrid* konvergencije, tj. konvergencije vrednosti deskriptora ocenjene iz digitalne aproksimacije oblika ka tačnoj vrednosti deskriptora sa povećanjem prostorne rezolucije [17, 46, 56, 58, 112]. Problem *multigrid* konvergencije svodi se na problem davanja gornje granice apsolutne greške metoda pri datoj rezoluciji i, pored same konvergencije, od velikog je značaja jer omogućuje da znamo grešku metoda pri datoj rezoluciji u realnim primenama.

Nedostatak preciznosti i tačnosti metoda analize oblika zbog grube podele piksela u binarnim slikama navodi istraživače na traženje načina za korišćenje drugih, dodatnih informacija da bi se preciznost i tačnost poboljšale. Glavni pravac ovog istraživanja je upotreba informacije o tome koliko je svaki spel pokriven oblikom [52, 54, 61, 78]. U okviru fazi skupova razvija se i dobro definisan matematički model za izdvajanje i dalje korišćenje informacije o pokrivenosti spelova oblikom [109]. Model omogućuje razvoj i poboljšanje mnogih metoda analize oblika. U [107, 110, 111] se pokazuje da model, u poređenju sa binarnim slikama, značajno povećava preciznost ocene površine, obima i deskriptora koji se naziva kompaktnost očuvavajući preciznost na istom, visokom nivou. U [106] je predstavljen metod koji poboljšava ocenu momenata oblika. U [12, 49] model zasnovan na pokrivenosti

spela oblikom se koristi za poboljšanje ocene signatura. Razvija se i nekoliko algoritama za segmentaciju koji omogućuju upotrebu navedenih metoda u različitim realnim uslovima. U [107] je dat algoritam za izračunavanje pokrivenosti spelova oblikom koji se zasniva na dvostrukom trešholdingu koji je pogodan za korišćenje kada su oblik i pozadina dobro separabilni i uređaj za dobijanje slike ima linearan odgovor. U [64, 108] je predložen metod koji se zasniva na lokalnom razdvajanju koji izračunava pokrivenost svakog spela iz neke binarne slike. Teorijski okvir za ovakvu segmentaciju dat je u [69] na grafovima.

Pored analize oblika, matematička morfologija je još jedno polje digitalne obrade slike koje se bavi oblikom. Njen izvorni problem se javio u rudarstvu kada je trebalo ukloniti spelove koji predstavljaju šupljine u stenama nebitne za izučavanje tako da na digitalnim slikama ostanu samo spelovi koji predstavljaju stene. Glavnu ideju za rešenje ovog problema uvode sredinom 1960. godine francuski naučnici Džordž Materon i Žan Sera [71, 101, 102]. Ideja se zasniva na zbiru i razlici Minkovskog [73] dva skupa.

Tokom 1960-tih i većeg dela 1970-tih matematička morfologija se zasniva na teoriji klasičnih skupova. Uobičajeno, spelovi sa vrednošću 1 smatraju se elementima skupa, a spelovi sa vrednošću 0 elementima komplementa, kao na primer u [101]. Ovo ograničava matematičku morfologiju samo na binarne slike. Ograničenje se prevazilazi uvođenjem operacija matematičke morfologije u [102] i daljim razmatranjem njihovih osobina u [119].

Kada su dilatacija i erozija počele da se koriste, strukturni elementi bili su fiksni, tj. jedan strukturni element se koristio za sve spelove slike. Takav strukturni element uobičajeno se naziva *rigidan* [19]. Podaci digitalne slike koje predstavljaju neku osobinu objekta mogu se menjati, iako se ta osobina ne menja u stvarnosti. Na primer, identični objekti mogu se na slici pojaviti kao različiti u veličini u različitim delovima slike zbog perspektive, ili se intenziteti koji ih predstavljaju mogu menjati zbog različitog osvetljenja. Zbog toga nastaje potreba da se definišu strukturni elementi koji se prilagođavaju, menjaju u zavisnosti od lokalnih osobina na slici. Takvi strukturni elementi koji mogu menjati svoju veličinu, oblik i vrednosti za različite spelove nazivaju se *adaptivni* strukturni elementi [11, 19, 21].

Rastojanje je funkcija $d : D \times D \rightarrow [0, \infty)$, gde je D neprazan skup. Rastojanje d se naziva *metrika* ako zadovoljava osobine *separabilnosti*, *simetrije* i *nejednakosti trougla*. Par (D, d) se uobičajeno naziva metrički prostor. Nije neophodno da neko rastojanje bude metrika da bi se koristilo u obradi slike. Ukoliko zadovoljava simetriju i nejednakost trougla rastojanje se naziva *pseudometrika*. Ukoliko zadovoljava *separabilnosti* i *simetriju* naziva se *semimetrika*.

Rastojanja su jedan od najstarijih i najviše korišćenih alata u digitalnoj obradi slike. Rastojanje koje je pogodno u svim situacijama kada se porede digitalne slike ne postoji. Koje rastojanje je najbolje u određenoj situaciji zavisi od mnogo

činilaca. Poređenje raznih osobina objekata, raznovrsni objekti predstavljeni digitalnim slikama, različiti uslovi dobijanja digitalnih slika su samo neki od činilaca koji su uzrokovali upotrebu velikog broja različitih rastojanja u digitalnoj obradi slike. Opširan pregled postojećih rastojanja dat je u [25]. Budući da se upotreba rastojanja u obradi slike konstantno širi, postoji neprekidna potreba za originalnim pristupima da se definišu nova i modifikuju postojeća.

Među najčešće korišćenim rastojanjima u digitalnoj obradi slike su *rastojanja Minkovskog* ili L_p *metrike*. L_p metrika je *Euklidsko* rastojanje za $p = 2$. Rastojanja između elemenata skupa D koriste se da se definiše rastojanje od nekog elementa do podskupa skupa D . Rastojanja od elementa do skupa nazivaju se *rastojanja od tačke do skupa* i koriste se da se definišu *rastojanja od skupa do skupa*. Rastojanje od skupa do skupa koje se smatra najstarijim u obradi slike je *Hausdorfovo rastojanje* [38, 82]. Iako je jedno od najviše korišćenih u obradi slike, Hausdorfovo rastojanje je previše osetljivo na spelove koji predstavljaaju anomalije na slici. Da bi se takav nedostatak otklonio, rastojanja od tačke do skupa se često sumiraju za sve tačke i skupove i računa se njihov prosek. Jedno rastojanje definisano na ovaj način koje se često koristi u digitalnoj obradi slike je *zbir najmanjih rastojanja* [30, 79]. Jedno rastojanje koje se često koristi u obradi slike, a ne zasniva se na rastojanju od tačke do skupa je *simetrična razlika* [55] između dva konačna skupa.

Postojeća morfološka rastojanja između dva skupa podrazumevaju *Hausdorfovo rastojanje dilatacijom i erozijom* [103], *rastojanje dilatacijom za binarne slike* [93] i *rastojanja dilatacijom i erozijom za sive slike* [92]. Kao i Hausdorfovo rastojanje dilatacijom i erozijom, rastojanje dilatacijom za binarne slike je previše osetljivo na anomalije na slici. Zbog toga se u definiciji rastojanja dilatacijom i erozijom za sive slike koriste sume, ali to istovremeno dovodi do drugih nedostataka.

Treće poglavlje

Pregled Ovo poglavlje zasniva se na radovima "Precise estimation of the projection of a shape from a pixel coverage representation" [27] i "Estimation of Feret's Diameter from pixel coverage representation of a shape" [28]. U Poglavlju 3.1 opisuje se značaj Fereovog dijametra. U Poglavlju 3.2 daje se opis ocene Fereovog dijametra iz digitalnih slika na tradicionalan način. U Poglavlju 3.2.1 opisuje se detaljnije problemi vezani za ovakvu ocenu, a u Poglavlju 3.2.2 ispituje se greška i multigrad konvergencija. U Poglavlju 3.3 dat je novi metod za ocenu Fereovog dijametra iz digitalnih slika koji koristi pokrivenost svakog piksela oblikom. Analiza greške i multigrad konvergencija ovog metoda su dati u Poglavlju 3.3.1 i Poglavlju 3.3.2, a dalje poboljšanje na osnovu analize greške metoda u Poglavlju 3.3.3. U Poglavlju 3.4 pored se performanse metoda na sintetičkim i realnim primerima.

Predstavljanje nekog oblika binarnom slikom u praksi odgovara njegovoj Gausovoj digitalizaciji. Obe varijante Gausove digitalizacije mogu se naći u literaturi [14, 15, 31, 33]. Kada se Fereov dijametar ocenjuje iz binarnih slika, koristi se Gausova digitalizacija oblika [48, 129]. U analizama gornje granice greške koristi se Gausova digitalizacija za aproksimaciju oblika konačnim skupom tačaka [17, 46, 56, 58, 112].

Kada se Fereov dijametar ocenjuje iz binarnih slika, najudaljenije tačke u datom pravcu aproksimiraju se temenima piksela, ako se koristi prva varijanta Gausove digitalizacije, ili centrima piksela, ako se koristi druga varijanta. U digitalnoj rešetki u kojoj je veličina piksela r , ovo dovodi do velike maksimalne apsolutne greške koja iznosi $\frac{\sqrt{2}}{2} \cdot \frac{1}{r}$ u prvom slučaju i $\frac{1}{r}$ u drugom slučaju za R -regularne oblike. Iako je ocena Ferevog dijametra iz binarnih slika multigrigrid konvergentna sa brzinom konvergencije $\mathcal{O}(\frac{1}{r})$, velika apsolutna greška je ozbiljno ograničenje [48, 129]. Problem je posebno naglašen pri manjin rezolucijama.

U [27] predlaže se algoritam za ocenu Ferevog dijametra koji se zasniva na pokrivenosti piksela oblikom. U eksperimentima je pokazano da je preciznost i tačnost ovog algoritma veća u poređenju sa ocenom iz binarnih slika. Ipak, u proseku, on ne daje tačnu vrednost, tj. ima određenu pristrasnost. Zbog toga se ocenjuje maksimalna apsolutna greška za dati R -regularan oblik u digitalnoj rešetki u kojoj je veličina piksela manja od R . Ovakav uslov obezbeđuje da se rub oblika u nekom pikselu nalazi između tangente i oskulaturnog kruga u datoj tački, što je važno za razmatranje. U suprotnom, ne mogu se odrediti tačke preseka piksela i ruba, a samim tim ni pokrivenost piksela oblikom.

Empirijskom analizom dolazi se do izraza kojim se popravljaju estimacija Ferevog dijametra iz digitalne slike tako da maksimalna apsolutna greška bude značajno manja. Algoritam je multigrigrid konvergentan sa brzinom konvergencije $\mathcal{O}(\frac{1}{r^2})$. Dakle, značajno brže u poređenju sa ocenom iz binarnih slika.

U sprovedenim eksperimentalnim istraživanjima na sintetičkim primerima u kojima je pretpostavljena tačna vrednost pokrivenosti piksela objektom pokazano je da je maksimalna apsolutna greška za različite položaje u digitalnoj rešetki smanjena u proseku 192 puta kada se ocenjuje maksimalan i 16 puta kada se ocenjuje prosečan Fereov dijametar za sve pravce. U realnim primerima, gde su primenjeni metodi za segmentaciju koji daju ocenu pokrivenosti piksela objektom, pokazano je da je greška smanjena približno 7 puta za slike snimljene jednostavnim kućnom kamerom pri maloj rezoluciji i približno 6 puta za mikroskopske slike ćelijskog jezgra pri različitim rezolucijama.

Četvrto poglavlje

Pregled Ovo poglavlje zasniva se na radu "Advanced morphological distances based on dilation and erosion" [26]. U Poglavlju 4.1 opisuje se značaj morfoloških

rastojanja. U Poglavlju 4.2 kratko opisujemo matematički model koji koristimo za razmatranja. U Poglavlju 4.3 analiziramo probleme vezane za izračunavanje rastojanja dilatacijom za sive slike. Definicije novih rastojanja kojima se problemi prevazilaze date su u Poglavlju 4.4. Eksperimentalna evaluacija na sintetičkim i realnim primerima data je u Poglavlju 4.5.

Da bi se jasno predstavili i analizirali problemi, slika se posmatra kao realna funkcija $f : [a, b] \rightarrow \mathbb{R}$. Svi zaključci mogu se direktno preneti na dvodimenzionalne diskretne funkcije. Najveći nedostatak rastojanja dilatacijom za sive slike, d_{dilate} , je to što ne može da se primeni na parove slika određenog tipa jer ne daje konačnu vrednost. Nedovoljno jasno objašnjenje za to dato je u [92]. U tezi se dokazuje potreban i dovoljan uslov da $d_{dilate}(f_1, f_2) \in [0, \infty)$, za dve slike f_1, f_2 . Iz uslova sledi da se d_{dilate} ne može izračunati za velik broj parova slika čije vrednosti su ograničene. Pored toga, postoje očigledni primeri da se f_1 i f_2 mogu značajno menjati, što modeluje značajne promene osobina objekata koje funkcija slike predstavlja, a da se $d_{dilate}(f_1, f_2)$ ne menja.

Problemi vezani za izračunavanje morfoloških rastojanja između sivih slika prevazilaze se uvođenjem adaptivne strukturne funkcije koja menja svoje vrednosti u zavisnosti od $x \in [a, b]$. Nova morfološka rastojanja definisana su korišćenjem istog koncepta kao i za definisanje rastojanja dilatacijom i erozijom, ali se strukturna funkcija vezuje za $|f_1(x) - f_2(x)|$, $x \in [a, b]$. Predložena rastojanja mogu se primeniti na proizvoljan par slika. Pored toga, imaju veću mogućnost da se vežu za određenju osobinu oblika nego sva ostala morfološka rastojanja. Kada razlike u objektima rastu, ona se povećavaju, a kada se smanjuju i rastojanja postaju manja. Predložena rastojanja su semimetrike.

U eksperimentalnoj evaluaciji na sintetičkim primerima koji simuliraju realne promene u osvetljenju jedne čestice u realnim uslovima za dobijanje slike pokazujemo da predložena rastojanja dobro prate promene u sivim vrednostima i daju važne informacije na osnovu njih. Na sintetički generisanim primerima koji simuliraju promene položaja čestica pokazujemo da predložena rastojanja mogu da se koriste za složen problem praćenja čestica. To istovremeno pokazuje da dobro prate promene položaja objekta u prostoru. Na realnom primeru satelitskog snimka pokazujemo da nova rastojanja imaju bolje performanse u poređenju sa svim ostalim rastojanjima jer se mogu jednostavno vezati za osobinu oblika od interesa izborom strukturnog elementa.

Peto poglavlje

U tezi je poboljšan način korišćenja digitalnih slika kada se porede objekti na osnovu svojih osobina oblika. Razmotrena su oba problema ključna za poređenje: kvantifikacija oblika i poređenje kompletnih podataka digitalne slike.

Dobijeni rezultati pokazuju da teoretski modeli i praktični metodi razvijeni za korišćenje pokrivenosti piksela oblikom, kao i modeli adaptivne matematičke morfologije mogu da se koriste za efikasnije poređenje objekata predstavljenih digitalnim slikama kada se poređenje zasniva na obliku.

Istraživanje predstavljeno u tezi može biti nastavljeno u mnogo pravaca, a neki od njih su spomenuti u petom poglavlju.

Abstract

A fundamental process performed over objects in many image processing tasks is their comparison. These tasks include object identification, recognition, classification and tracking. Generally, comparing objects based on their digital image representations can be conducted in two ways depending on the amount of used image data. The first one is to extract suitable objects characteristics that can be quantified and perform comparison just based on them. The second is to compare complete digital image data representing objects. For both ways the shape of objects of interest plays a crucial role because it has a great discriminating power between objects and allows many numerical quantifications.

The proposed thesis investigates development, improvement and evaluation of methods for quantitative characterization of objects from their digital images and similarity measurements between digital images. The digital image data used to represent objects is not fully exploited when shape based comparison is performed. Methods for quantitative characterization of objects from their digital images are increasingly used in applications in which error can have critical consequences such as medical imaging or autonomous vehicle control, but the traditional methods for shape quantification are of low precision and accuracy. It is highly desirable that a distance measure between digital images can be related to a certain shape property and morphological operations are used when defining a distance for this purpose. Still, the distances used in image processing defined in this manner turn out to be insufficiently sensitive to relevant data representing shape properties in images. The main goal of the thesis is the development and the improvement of methods for comparison and quantification of objects from their digital image representation in order to more successfully exploit data having at disposal and overcome mentioned problems.

The theoretical framework and practical methods developed for utilizing pixel coverage by an object are successfully used to overcome problems of lacking precision and accuracy of different methods for shape quantification. We show that the framework and methods can be used to highly improve the accuracy and precision of using digital images to estimate the maximal distance between objects two furthest points measured in a given direction. Adaptive mathematical morphology

is a field developing rapidly to deal with extracting relevant geometrical structures from an image. We show that the idea of adaptive mathematical morphology can be used successfully to overcome problems related to sensitivity of distances defined via morphological operations when comparing objects from their digital image representations. Superiority of methods proposed in the thesis comparing to existing is shown on theoretical toy examples, synthetic and real images.

Work presented in the thesis provides many directions for further research. We found particular motivation for conducting this research in high outperformance of the proposed methods comparing to other used for the same purpose in experimental evaluations as well as in fundamental role of comparing objects in many image analysis tasks.

Contents

Rezime	i
Abstract	xiii
Contents	xv
Notation	xvii
Abbreviations	xvii
1 Introduction	1
2 Background	9
2.1 Shape Analysis	10
2.2 Traditional Digital Representation of a Shape	14
2.3 Pixel Coverage Representation	21
2.4 Mathematical Morphology	27
2.5 Distances in Image Processing	34
3 Feret’s Diameter	43
3.1 Importance of Feret’s diameter	43
3.2 Estimation from Binary Images	44
3.2.1 Examples and Motivation for Improvement	45
3.2.2 Error analysis and multigrid convergence	46
3.3 Estimation from Pixel Coverage Representation	48
3.3.1 Lower and upper error bounds of Algorithm 1	53
3.3.2 Empirical analysis of the error	56
3.3.3 Improved method for estimation of Feret’s diameter	57
3.4 Evaluation	59
3.4.1 Synthetic data	60
3.4.2 Real data	61

4	Advanced morphological distances	67
4.1	Importance of morphological distances	67
4.2	Model description	68
4.3	Examples and motivation for improvement	69
4.3.1	Necessary and sufficient conditions for computing d_{dilate}	69
4.3.2	Insensitivity of d_{dilate} to changes in gray values	70
4.4	New morphological dilation and erosion distances	73
4.4.1	Metric properties for d'_{dilate} and d'_{erode}	77
4.5	Experimental evaluation	79
4.5.1	Behavior depending on changes in gray levels	79
4.5.2	Particle tracking	81
4.5.3	Satellite images	83
5	Conclusion and discussion	89
	Bibliography	91

Notation

\mathbb{R} - the set of real numbers

\mathbb{Z} - the set of integer numbers

\mathbb{N} - the set of natural numbers

n - a natural number

(x_1, x_2, \dots, x_n) - an ordered n -tuple

$|x|$ - the absolute value of a number x

$|X|$ - the cardinal number of a set X

$\max_{x \in X} f(x)$ - maximum of a function f over a set X

$\inf(x_1, x_2, \dots, x_n)$ - the infimum of a n -tuple

$\sup(x_1, x_2, \dots, x_n)$ - the supremum of a n -tuple

$Per(S)$ - the perimeter of an object S

∂S - the border of an object S

$A(S)$ - the area of an object S

$A(f)$ on D - the definite integral of a function f on D : $A(f) = \int_{x \in D} f(x) dx$

$V(S)$ - the volume of an object S

$\mathcal{G}_1(S)$ - the first type of Gauss digitization of an object S

$\mathcal{G}_2(S)$ - the second type of Gauss digitization of an object S

X^c - the complement of a set X

\check{X} - the reflection of a set of position vectors X , $\check{X} = \{\mathbf{x} \mid -\mathbf{x} \in X\}$

$\text{int}(X)$ - the interior of a set X

$\text{cl}(X)$ - the closure of a set X

$Des(X)$ - A descriptor of a set of points X

$[x]$ - the nearest smaller integer of x

mod - the modulo operation

Abbreviations

CT - computer tomography

RGB - red, green, blue

px - pixels

cm - centimeters

mm - millimeters

m - meters

μm - micrometre

$BAP1$ - binary approach 1

$BAP2$ - binary approach 2

COV - coverage approach

COV^{corr} - coverage approach corrected

$\oplus nO$ - n subsequently performed dilations by a structuring element O

$\ominus nO$ - n subsequently performed erosions by a structuring element O

JAXA - Japan Aerospace Exploration Agency

Chapter 1

Introduction

For a long time, imaging has been a possibility for extracting, describing and evaluating many properties of objects and scenes instead just being the way for capturing the light reflected by a two-dimensional surface. A striking and illustrative example of using images for exploring properties of imaged objects are X-ray images. X-rays are not just helpful in exploration, but since the first time systematically presented by Wilhelm Röntgen in 1895, they have enabled exploration in an efficient manner, which was not possible before their discovery.

The capability of images to capture valuable information about observed objects imposed many problems related to extraction, visualization and manipulation of objects and their properties. After the emergence of the computer technology in World War II, researchers were intensively exploring possibilities for using computers to process image data. This resulted in the development of the first programmable computer (Standards Eastern Automatic Computer or SEAC) that allowed images to be fed into its memory. The computer was developed by a computer pioneer Russell Kirsch and his colleagues at National Bureau of Standards (NBS, now known as the National Institute of Standards and Technology, or NIST) in 1957. In this way arose a new scientific field named *digital image processing*, i.e. processing of images by digital computers. The computer technology continued its rapid development after the emergence and it will not stop to develop in the future. In parallel, imaging devices are rapidly evolving. They provide more and more credible digital image depiction of increasingly different objects in increasingly different conditions. Digital cameras, magnetic resonance imaging or computerized axial tomography scanners are just some notions integrated in daily life. The great possibilities to capture object properties by images and process them by computers have caused a breakthrough of digital image processing into almost all scientific fields and studying objects based on their digital image representations has become a standard procedure in scientific research.

To enable considering physical properties of real world objects based on their

digital images, a mathematical formalization of the data represented by an image is needed. For this purpose, an image can be observed as a change of one or more quantities (usually energy that originates from the electromagnetic radiation or ultrasound) that carries some information about objects being imaged, that is as a *signal*. A signal is observed as a function, so the same can be used to model an image as:

$$f : D \longrightarrow \mathbb{R}, \quad D \subset \mathbb{R}^n, \quad (1.1)$$

where $(x_1, x_2, \dots, x_n) \in D$ are *spatial coordinates* and represent a point $\mathbf{x}(x_1, x_2, \dots, x_n)$ in the observed space at which the signal is perceived. $f(x_1, x_2, \dots, x_n)$ expresses the reflected or absorbed energy by an environment being imaged at \mathbf{x} and is named *image intensity* or *gray value* at $\mathbf{x}(x_1, x_2, \dots, x_n)$ [36]. The domain of an image function is bounded as only a limited portion of the space can be imaged and the set of image intensities is bounded as only a limited amount of radiation can be used.

A wide range of imaging techniques enable research of different physical properties by observing their images and we list just some examples. The intensity of X -rays decreases exponentially with the distance from their source and the density of passed material. When this is expressed by $f(x_1, x_2, \dots, x_n)$, the internal structure of a tissue can be studied. In [74] such an image function is used to study morphological properties of cells. In [100] the data expressed in the same manner is used to provide quantitative measurements of fibres of biomaterials such as bones or teeth. Atmospheric pollutant can be studied when $f(x_1, x_2, \dots, x_n)$ expresses the intensity of electromagnetic radiation from the Sun that is absorbed and reemitted by the Earth and atmosphere. On the basis of this, in [29] is given a number of different measures suitable for tracking pollutant plumes.

Digital images

Processing by a computer is inherent with the loss of information about objects provided by an image. This is due to the fact that an image function has to be translated into a form which can be represented in a computer with finite memory. This process is named *digitization* and involves two steps, *discretization* and *quantization*. After a digitization, the domain and set of intensity values of an image are discrete sets. Whereas they are bounded, they are both finite. An image function with finite domain and finite set of intensity values represents a *digital image*.

To discretize an image domain, spatial coordinates are usually approximated with values regularly distributed in a grid. The number of these sample values per unit is called *spatial resolution* of a digital image. The process of taking just some, sample, values to represent real coordinates is called *sampling*. After sampling, a

point in a grid represents a regular portion of the space \mathbb{R}^n consisting of all the points of \mathbb{R}^n which are closer to it than to any other grid point. Such portion is named the *Voronoi region* of the point under consideration, after Georgy Feodosievich Voronoy (1868-1908) who gave unprecedented contribution in the theory of the regular partition of spaces. In digital image processing, Voronoi regions that correspond to grid points are called *pixels* (picture elements) for two-dimensional images, *voxels* (volume elements) for three-dimensional images or *spels* (spatial elements) in general.

Similarly to spatial coordinates, intensity values are usually allowed to be just values equally distributed in a predetermined interval $[a, b] \subseteq \mathbb{R}$. The number of allowed values per unit is called *gray level resolution*. The process of taking only some discrete values from the real interval is called *quantization*. It is frequently performed such that values can be suitably represented by a binary code adapted to the computer memory. In the most of digital images in daily use, an image function is allowed to take $2^8 = 256$ values from \mathbb{R} which corresponds to the number of values that can be represented by one byte.

Comparing objects from their digital images

The fundamental process performed over objects in many image processing tasks is their comparison. A reference object is compared to other objects for the problem of identification and recognition. Objects are compared with each other for the problem of classification. One object can be compared to itself in different time moments to inspect changes in its position or shape. We listed just some of the numerous situations when comparing is performed, but, generally, comparing objects based on their digital image representations can be conducted in two ways depending on the amount of image data used for that purpose.

When possible, it is computationally less expensive to compare just some object characteristics than to compare the complete image data representing objects. Due to this, only such, suitable, characteristics are frequently extracted from digital images and used in further processing. For instance, if the two cells presented in Figure 1.1 should be compared, internal patterns and color may be considered as non-informative for a particular application. Intensity values expressing internal patterns and color can be neglected and objects efficiently compared by considering only properties of their shapes presented in Figure 1.1(c) and Figure 1.1(d). For example, properties such as area or perimeter can be used. one such shape property is presented in Chapter 3 and methods for its accurate extraction from digital images are developed.

There are situations in which properties of imaged objects are compared by the direct comparison of their digital images. This is common when the complete image data is relevant for consideration and extracting just some characteristics

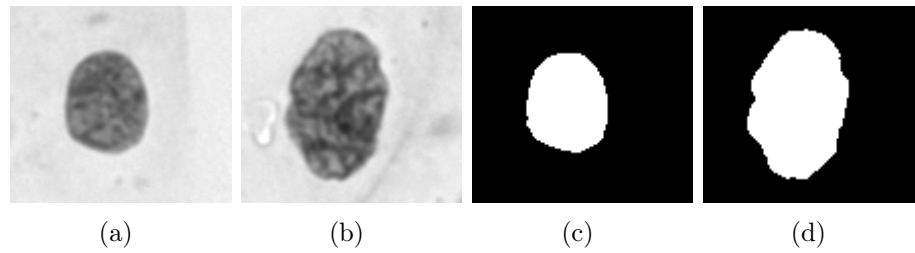


Figure 1.1: Cell nuclei in a) and b) can be compared by comparing just their shapes presented in c) and d).

leads to the loss of principal information. For instance, in Figure 1.2, taken from [29], intensity values express the number of nitrogen dioxide molecules per square centimetre over the same area in different time periods. If the density of this prominent indicator of pollution in different time intervals should be compared by comparing presented digital images, rejection of some intensity values or some spatial information about them would lead to loss of the principal data under consideration. In situations like this, distance measures between images are used for comparing objects of interest. For example, the sum of absolute differences between image intensities can be computed to follow changes in pollution during time. One such developed distance measure with particularly appealing properties for comparing objects by comparing their digital image representations is presented in Chapter 4.

Problem description

Methods for quantitative characterization of object properties extracted from digital images are increasingly used in applications in which an error can have critical consequences. The examples of such applications are medical imaging or autonomous vehicle control. Because only a finite set of data is used to quantify a real world object, these methods usually *overestimate* or *underestimate* true value. Usually, a method on average has a certain deviation, named *bias*, from the true value. Due to the negative consequences of relying on incorrect measurements, it is of a great importance that the bias is low, i.e. that that the *accuracy* is high and that in repetitions in unchanged conditions a method provides values which are close to each other, i.e. that it has high *precision*.

A widely used property for quantitative characterization of an object is the distance between its two furthest points measured in a given direction. This distance is named *Feret's diameter* of an object. Estimation of Feret's diameter from digital images belongs to methods which are traditionally performed on binary images in which intensity values can only be 0 or 1. Binary images are in contrast

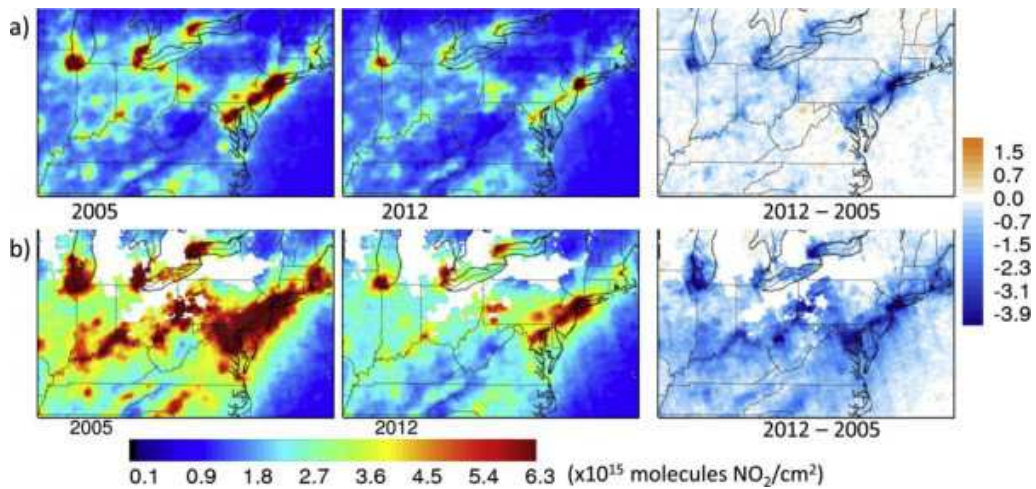


Figure 1.2: Image taken from [29]. a) From left to right, average nitrogen dioxide density ($\frac{\text{molecules}}{\text{cm}^2} \cdot 10^{15}$) for the period May-September in 2005, 2012 and the difference of these two images. b) The same, but as the annual average (January-December)

to *gray scale* images where other values are allowed. Value 1 is assigned to the spels which correspond to the sample points considered to belong to the interior or the border of an object and value 0 is assigned to the spels which correspond to sample points considered to belong to the exterior. In this manner, spels are sharply divided into those which represent an object and those which represent the background. The assumption that a pixel is a part of an object or its background in binary images, although pixels are regions and may be not completely part of an object nor completely part of its background, causes lack of accuracy and precision of traditional methods. The problem is particularly pronounced when pixel regions represent significant parts of an object under consideration, i.e. additional resolution is needed. For example, in satellite images a pixel can represent a larger part of land, or in microscopic images a pixel can represent a considerable part of a cell. In this thesis, this issue of lacking accuracy and precision will be addressed by using additional information, provided by gray scale images, about coverage of every pixel by an object.

Distances between images are widely used in applications in which it is highly desired to follow a certain geometrical property of objects over time. For instance, it is needed to follow changes in position of objects in object tracking or it is frequently needed to follow changes in the shape of different physical phenomena such as lakes or elevation structures in geographical information science. Besides, disturbances such as noise or outliers are often present in digital images. If a distance

is sensitive to such irrelevant data it often becomes useless in real applications. Due to this, it is highly desirable that a distance measure between digital images can be related to a certain shape property of objects to be compared without being disturbed by irrelevant data.

To extract the relevant geometrical structure from an image, morphological *dilation* and *erosion* can be used. The dilation of an image is an operation which assigns the maximal value in a neighborhood to every image spel. Before assigning the maximal value, intensity values in a neighborhood can be increased. A spel neighborhood considered during a dilation is called a *flat structuring element* and its increase in values is defined via a *non flat structuring element* or a *structuring function*. A flat structuring element as well as a structuring function can be *rigid* if they are the same for all spels or *adaptive* if they change their shapes and values depending on a spel in an image. The erosion of an image is similar to dilation, but the minimal value in a neighborhood is assigned instead of the maximum and a structuring function decreases values instead of increasing them. To denote the collection of distances between digital images which are defined using dilation or erosion to be related to a certain geometrical property, the notion *morphological distances* is used.

The existing morphological distances are based on flat, rigid structuring elements. Defined in this manner, they turn out to be insufficiently sensitive to relevant data representing shape properties in images. More particularly, the morphological distances mainly used for binary images are highly sensitive to disturbances in images such as noise and outliers. The morphological distances mainly used for gray scale images do not provide finite value when computed for a large number of digital image pairs with finite image intensities. Besides, it is possible that dissimilarities between compared objects strongly grow and the distances do not change their value when computed for digital images representing such changes, i.e., they are too insensitive in many situations. In the thesis, the problem of the insensitivity will be addressed by introducing an adaptive structuring element to define morphological distances.

Thesis goal

The shapes of objects are of the crucial importance for their comparison, but the digital image data used to represent objects is not fully exploited when shape based comparison is performed and there is room for improvements. This causes problems with the accuracy and precision of methods for quantitative characterization of object properties and insensitivity of morphological distances to shape properties. The main goal of the thesis are the development and improvement of methods for comparison and quantification of objects from their digital image

representations in order to exploit more successfully data at disposal and overcome described problems.

Publications and the structure of the thesis

Chapter 2 presents the overviews of shape analysis, mathematical morphology and distances used in image processing together with definitions and basic notions to be used in the thesis.

The problem of accuracy and precision of Feret's diameter estimation from digital images is addressed in Chapter 3 which is based on [27, 28]. The problem is addressed by considering gray scale instead of binary images. The considered gray values provide additional information about the coverage of every pixel by the object under consideration. By comparing method that utilizes such information with traditional methods, it is shown that it significantly outperforms them in accuracy and precision. The comparison is performed on real and synthetic examples.

The problem of computing morphological distances between digital images is addressed in Chapter 4. The foundation of the chapter is [26]. The problem is addressed by introducing adaptive structuring functions in defining morphological distances. By comparing morphological distances based on flat rigid structuring elements and morphological distances based on adaptive structuring functions, increased applicability of the latter is shown. That the new morphological distances highly outperform existing ones is shown on toy examples, as well as synthetic and real digital images.

Chapter 5 concludes the thesis and discusses current and future work.

Chapter 2

Background

The research subject of the thesis, in its broadest context, belongs to *morphology* because the methods to be explored are based on shape. The word morphology comes from Greek words *morph* and *logia*. *Morph* means *shape, form* and *logia* means *study of*. So, morphology is the study of the shape. In image processing, morpho-logy is represented in two fields, *shape analysis* and *mathematical morphology* and we widely use models and methods existing in these fields in our research.

During formation of an object, many different influences leave inscription in its shape. This makes the shape of a real world object a comprehensive source of information which is constantly explored to reveal and interpret such inscriptions. The significance of shape reflects in the fact that it takes a central place in many scientific fields. An example of such field is *morphology in archaeology* which studies grouping archaeological artifacts into time periods based on their shapes. One more example of studying object properties based on the shape is *morphology in biology* dealing with drawing inferences about various properties of organisms from their shapes.

Image analysis belongs to the fields in which morphology is of great importance too. As it is breaking through a great variety of research tasks, image analysis faces with more and more demanding criteria when dealing with shapes. Problems that arise are numerous and vary from task to task.

Shape analysis covers a broad collection of methods based on shapes of objects for reducing digital image data to form suitable for further processing. Mathematical morphology covers a broad collection of methods for extraction and exploration of morphological properties of sets. Further on, we give basics of shape analysis and mathematical morphology.

Since shape analysis methods will be explored, we give an overview of the field of shape analysis and criteria and conditions for efficiency of shape analysis methods. Since a morphological distance will be presented, we give an overview

of the field of mathematical morphology and distances in image processing with special emphasis on morphological distances.

2.1 Shape Analysis

In image analysis, the formal definition of the shape of an object does not exist. It is a basic property of every object, like color and texture. The shape of an object is always represented by a bounded set of points with coordinates in \mathbb{R}^n that extracts just the geometrical extent of the object while all the other properties such as color or texture are ignored. Two sets of points represent the same shape if there exists a similarity transformation that maps one set onto another. Therefore, a shape can be understood as an equivalence class under the similarity transforms in the set of all objects [105]. It is frequently considered as a silhouette of an object if ignoring its size, rotation and position. In the literature, it is also referred to as a region. In image processing, a planar shape is traditionally presented by binary images. As an illustration, some examples of binary images representing planar shapes of objects are given in Figure 2.1.



Figure 2.1: Some examples of shapes of objects

About the pivotal role of shapes in discerning between objects can be concluded from the importance of shapes for the human visual system. The theories of human visual system are frequently considered when shape analysis methods are discussed. For a survey of such theories related to shape analysis, we refer to [67]. The human visual system is one of the most sophisticated and the most versatile existing visual systems and is not surpassed by any similar artificial system. In that system, it is undeniable that shapes of objects have the principal weight in discerning between them, before other properties such as color, texture and shades. In [60] it is shown that children classify objects primarily based on shapes and secondarily based on other properties. In [8,39] it is shown that other object properties do not contribute to the speed and accuracy of discerning between objects having different shapes. An established theory is that humans recognize objects based on the combinations of small elementary shapes named *geons* [7]. One of aims of exploring the human visual system is to follow it when developing artificial systems.

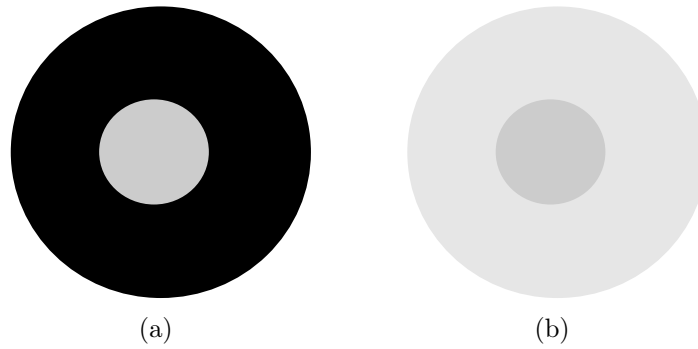


Figure 2.2: Two inner disks have the same image intensity, but the disk in b) appears darker as background becomes brighter

The human visual system has the ability to adjust perception of the light in order to single out a shape that is of interest in an image. To illustrate this, let us consider Figure 2.2 where the inner discs have equal image intensities, but the one in b) appears darker as the background becomes brighter. *Image segmentation* is the process of subdivision of an digital image into its component regions that extracts the shape of interest out of other components in a digital image. During a segmentation, the subdivision is commonly preformed based on the homogeneity of pixels representing an object and their dissimilarity with other image components. The most widely used method for segmentation is *thresholding*. It comprises determination of a threshold value such that the image intensities representing object points are greater or equal to the value and the image intensities representing background are lower, or vice versa. In [104] is given an overview of techniques used for thresholding. In [32] is given a comparative study on *region growing* segmentation which implies iterative addition of neighboring points to a set of seed points according to a predefined similarity property. *Region splitting and merging* is similar to region growing, but it begins with a division of an image into regions and then splits or merges regions according to a set of predefined criteria. This approach is often more efficient when objects and the background are roughly indicated by a user as presented in [80] for instance. *Boundary-based segmentation* implies detecting edges, lines and isolated points. An overview of boundary based techniques is given in [6].

After segmentation, the shapes of objects are well defined and extraction of shape properties by a shape analysis method is enabled. The process of shape analysis commonly begins with a method for *shape representation*. Shape representation entails further reduction of the image data obtained by segmentation.

It results in a high-dimensional vector that encodes a shape truthfully or approximately, but preserves shape characteristics which are relevant for further processing. Which characteristics are relevant depends on a particular application. The high-dimensional vector provides a good visual interpretation and compression. Further on, we give short overview of some methods for shape representation.

Representing shape by an one-dimensional function computed from shape boundary points is a classical shape representation method named *signature*. Very frequently used signature is *centroid distance function*:

$$C(t) = \sqrt{(x(t) - x_c)^2 + (y(t) - y_c)^2}, \quad (2.1)$$

where $(x(t), y(t))$, $t \in [a, b] \subset \mathbb{R}$ are border points and (x_c, y_c) is the centroid of the shape under consideration. The examples of some other signatures existing in the literature are *tangent angle* and *cumulative angle*. Properties of signatures are presented in [53, 133] and they are shown to be sensitive to noise when estimated from binary images. *Polygonal approximation* of a shape is a polygon that represents it in the best way according to a pre-selected criterion, as the minimization of sum of distances of polygon vertices to border of approximated shape, for instance. An evaluation of different methods for polygonal approximation is given in [86]. The representation of a shape by the string of the neighboring border pixels is called *chain code*. Efficiency of different algorithms for computation of chain codes is examined in [95].

Because shape is known to have a strong discriminating power, a number of shape characteristics have been developed to capture this power. A suitably chosen characteristic for consideration is preferable to be quantified. For instance, a shape can be convex or not in geometry. In shape analysis, convexity is the shape property for which is developed probably the largest number of methods for measuring and expressing by a number to which degree a shape is convex. In [68] one method for computing convexity of a given shape is to, for randomly chosen two points of the shape, compute the probability that the line segment determined by the points is completely contained in the shape. Another method for computing convexity from [68] is to compute the ratio of the shape area and the area of its convex hull. In [87] the convex polygon that fits best a polygonal shape is computed instead of the convex hull and the ratio of the shape area and the polygon is proposed as a convexity measure of a polygonal shape. In [136], as a convexity measure of a polygon, is proposed the ratio of the perimeter of the minimal rectangle having the edges parallel to coordinate axes which includes the polygon and the perimeter of the polygon. These are just some methods for computing convexity of shapes in shapes analysis. They differ in terms of computation complexity, sensitivity to noise, sensitivity to changes at the border or interior of a shape. We emphasize that, although all being methods for computing convexity, every of them gives a

different number for the same shape and that there is a permanent demand for new methods for quantifying the same shape property. The aim is to uniquely characterize a shape by numbers.

The process of quantification of shape properties is named *description* and a shape property quantified by a number is named *descriptor*. Besides convexity, many other descriptors exist in the literature, and we list just a few. Area and perimeter are well known features of shapes used as descriptors and exhaustively studied in the literature. For different methods for estimation of area and perimeter of shapes from digital images and their evaluation we refer to [10, 16, 107, 110]. Some other descriptors are defined exclusively for the purpose of shape analysis. A polygon is *rectilinear* if its interior angles belong to the set $\{\frac{\pi}{2}, 3\pi/2\}$. Similarity measure of a polygonal shape to a rectilinear polygon as a shape descriptor called *rectilinearity* is studied in [89]. Similarly, descriptors which expresses how similar a shape is to a perfect ellipse is called *ellipticity* and is studied in [134]. For an exhaustive overview of shape analysis techniques, we refer to [67, 133, 135].

Since the estimation of shape descriptors from digital images is investigated in the thesis, we shortly illustrate the basic concept of shape description. Let us observe the shapes given in Figure 2.1. The problem consists of providing a description expressed by a number for every shape in the figure such that we can discern between shapes just based on such number. Such number can be, for example, the size of a shape along the direction 60° . This number, would be the largest for the second shape, thereafter for the fifth, the first, the third and smallest for the fourth shape. To more clearly discern between the first and the fifth shape, some other, additional, descriptor can be considered. The numbers expressing descriptors can be used for recognition, classification or identification of objects.

Feret's diameter

To give a formal definition of the descriptor which is investigated in the thesis, we consider projections of points of bounded planar sets onto a given line that passes through the origin. We are interested in the maximal distance between pairs of such projection points.

Definition 2.1.1. *The scalar projection of the position vector of a point $\mathbf{p}(x, y)$ onto the unit vector in the direction given by angle φ is:*

$$\text{proj}_\varphi(x, y) = (x, y) \cdot (\cos \varphi, \sin \varphi) = x \cdot \cos \varphi + y \cdot \sin \varphi. \quad (2.2)$$

For a given bounded set X , by $\text{proj}_\varphi(X)$ we denote the set of scalar projections of position vectors of all points in X .

We refer to a point of X for which an extremal projection value $\min(\text{proj}_\varphi(X))$, or $\max(\text{proj}_\varphi(X))$, is attained, as an *extremal point* of X in the direction φ .

Definition 2.1.2. *Feret's diameter of a closed and bounded set X in the direction φ is the difference between maximal and minimal value of $\text{proj}_\varphi(X)$:*

$$\mathcal{F}_\varphi(X) = \max(\text{proj}_\varphi(X)) - \min(\text{proj}_\varphi(X)). \quad (2.3)$$

Some authors use the term width function [121] instead of Feret's diameter. These two notions represent the same concept. When computed for multiple angles Feret's diameter can be used for computing other shape descriptors. For instance, classic diameter, $\text{diam}(X)$, of a set X and elongation $\mathcal{E}(X)$ can be estimated using following formulas:

$$\text{diam}(X) = \max_\varphi(\mathcal{F}_\varphi(X)), \quad (2.4)$$

$$\mathcal{E}(X) = \max_{\varphi \in [0, \pi]} \frac{\mathcal{F}_\varphi(X)}{\mathcal{F}_{\varphi + \frac{\pi}{2}}(X)}. \quad (2.5)$$

To estimate the perimeter of a convex shape the following theorem can be used:

Theorem 2.1.3. *(Cauchy's theorem) [72] The perimeter of a convex shape X is given by: $\text{Per}(X) = \pi \cdot \bar{\mathcal{F}}$, where $\bar{\mathcal{F}}$ is the average Feret's diameter over all directions.*

2.2 Traditional Digital Representation of a Shape

The concept of shape description appears simple because shapes have a great number of properties which have a great discriminating power between objects and which can be easily measured. Still, shape analysis is a complex task and there are many aspects to be taken into account when it is addressed. The majority of these aspects is related to the fact that a shape analysis method should provide a measure of a real world object based on a digital image. This places shape analysis in the domain of *image analysis*, i.e. extracting relevant information from data represented by digital images. In following, we give an overview and shortly discuss the mostly used ways to represent a shape by digital data and describe a property which a shape should have in order for its basic characteristic be preserved after digitization. This is followed by a description of a framework for the error of estimation of a shape descriptor from digital data.

Digitization

A single real world object can have many digital approximations of its shape. To study such approximations many different digitization models are defined in the literature. For an overview of different approaches for digitizing objects we refer to [117] where they are generalized to an arbitrary dimension. We here state methods that are mainly used for digitization of shapes. The *subset* sampling is

the simplest, most widely used in practice, and the model with the most studied theoretical properties. It assumes taking into account grid points contained in a shape. The *supercover* sampling is an alternative model that assumes taking into account grid points whose Voronoi regions have a non-empty intersection with a shape under consideration.

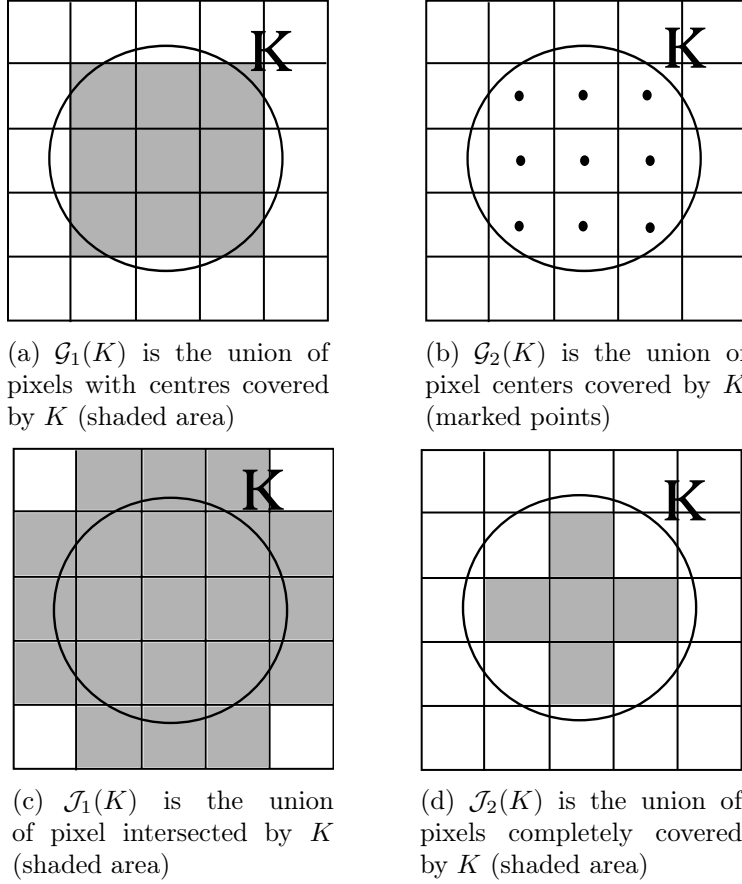


Figure 2.3: Different types of digitization of a disk K here visualized only as its circular boundary.

When used for planar objects in a square digital grid, the subset sampling is named the *Gauss digitization* after well known mathematician Carl Friedrich Gauss (1777-1855) who was using it for studying shapes. We will use two variants of Gauss digitization in the thesis:

Definition 2.2.1. For an object $S \subset \mathbb{R}^2$, inscribed into an integer grid with pixels $p_{i,j}$, the Gauss digitization of S is any of the following:

$$\mathcal{G}_1(S) = \{p_{i,j} \mid (i,j) \in \mathbb{Z}^n \wedge (i,j) \in S\} , \quad (2.6)$$

$$\mathcal{G}_2(S) = \{(i,j) \mid (i,j) \in \mathbb{Z}^n \wedge (i,j) \in S\} . \quad (2.7)$$

Famous mathematician C. Jordan (1838-1922) used supercover sampling to study the volume of objects in the three dimensional space and two types of digitization are named after him. The union of pixels, for two-dimensional shapes, or voxels, for three-dimensional shapes, that corresponds to supercover sampling is named *Jordan outer digitization*. The union of pixels or voxels that corresponds to the set of points which are not in the supercover sampling of the complement of a shape under consideration is named *Jordan inner digitization*. Jordan inner digitization consists of all the pixels or voxels completely contained in the shape. We denote Jordan outer digitization with \mathcal{J}_1 and Jordan inner digitization with \mathcal{J}_2 . Illustrations of mostly used types of digitization of shapes are given in Figure 2.3, where digitizations of a disk by these methods are presented.

Theoretical considerations of some other methods for digitization exist in the literature, but they are rarely used in practice. Among them, we mention Hausdorff digitization [84] that minimizes the distance between the border of a shape and the border of the union of Voronoi regions used to represent the shape. The Hausdorff digitization is not used in practice because it is defined globally and heavily depends on the alignment of the digital grid and a shape.

Even in the same model for digitization, a shape has many different digitizations. For instance, in [47] authors show that there is approximately $3\pi R^2 + R^{\frac{330}{208}}(\log R)^{\frac{18627}{8320}}$ different Gauss digitizations of a simple shape as the disk with radius R . After a digitization, the original shape is irretrievably lost and it is approximated by another set of points, i.e. another shape. The approximation does not necessarily preserve properties of the original shape and an error in computation of shape descriptor from its digital image representation is inevitable in the vast majority of cases.

To illustrate an error of computing a shape descriptor introduced by digitization, let us observe Figure 2.4(a) of a disk and the Euclidean distance $d(\mathbf{x}, \mathbf{y}) = \sqrt{(x_2 - x_1)^2 + (y_2 - y_1)^2}$ between points $\mathbf{x}(x_1, x_2)$ and $\mathbf{y}(y_1, y_2)$. The radius of the disk is $2.5 px$ and the center is positioned at $(x_c, y_c) = (4.5, 4.5)$ in the digital grid. The diameter of \mathcal{G}_1 digitization representing the disk given in Figure 2.4(b) is $\sqrt{34} \approx 5.83 px$. If the center is translated to the point with coordinates $(5, 5)$, \mathcal{G}_1 of the disk changes to the one presented in Figure 2.4(c), and the diameter becomes $4\sqrt{2} \approx 5.66 px$. Figure 2.4(d) illustrates \mathcal{G}_1 of the disk at the position $(x_c, y_c) = (4.25, 4.75)$ for which the diameter amounts $\sqrt{34} \approx 5.83 px$, again. If there exists a position of the circle center for which the diameter is $5 px$, the estimation would be accurate and if it did not depend on the position, but provided always the same value, it would be precise.

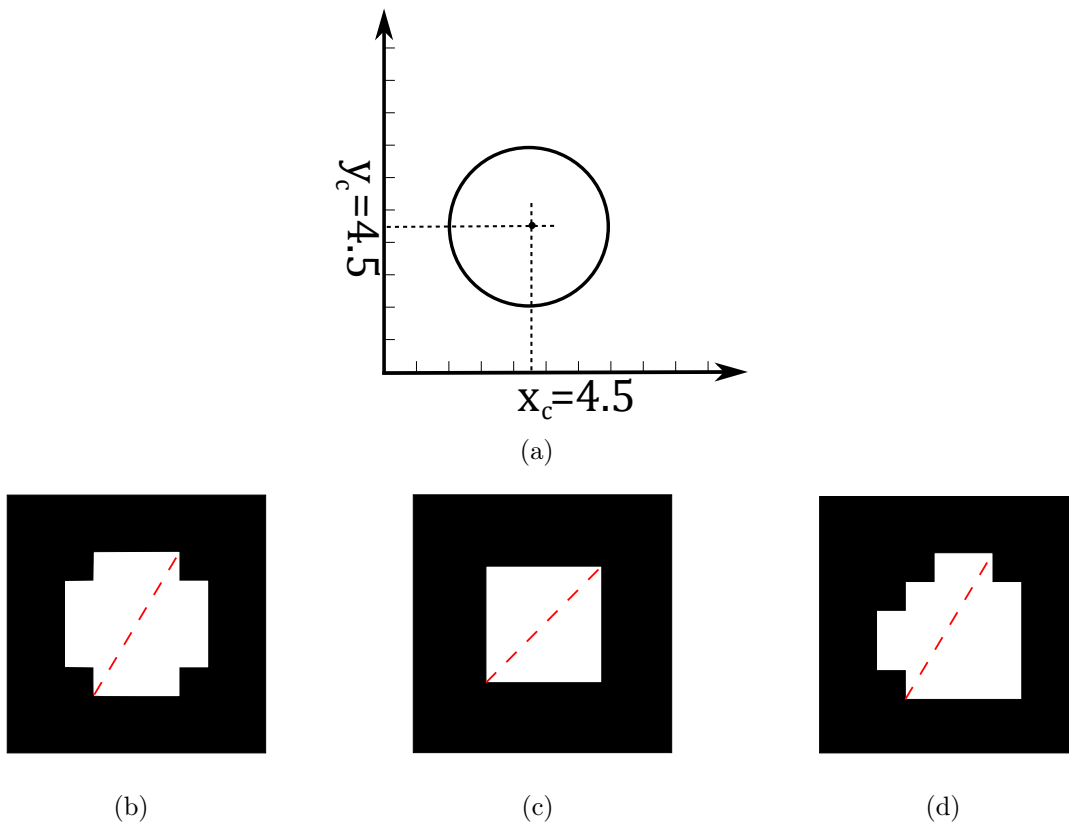


Figure 2.4: A disk with radius $r = 2.5 \text{ px}$ in a digital grid and some of its possible binary image representations depending on the position in the digital grid. Estimated from the given binary images, a simple descriptor as diameter changes its value and amounts $\sqrt{34} \approx 5.83 \text{ px}$, $4\sqrt{2} \approx 5.66 \text{ px}$, and $\sqrt{34} \approx 5.83 \text{ px}$, respectively. An estimation of the diameter is marked with the red dashed line.

R-regularity

To understand and formalize the conditions of a good performance of a shape analysis method, a question naturally arises : Which shape information is preserved during a digitization? There is an extensive literature as a result of the effort to answer this question. In all these papers the concept of *R-regular sets*, given in sequel after the notion of *osculating disk*, has a fundamental role.

Definition 2.2.2. *Let ∂X be the smooth boundary of a shape $X \subset \mathbb{R}^n$. A ball that shares a tangent hyperplane with ∂X at a point $\mathbf{p} \in \partial X$ is referred to as an *osculating ball of X at \mathbf{p} .**

Definition 2.2.3. [118] *A compact set $X \subset \mathbb{R}^n$ is *R-regular* iff for each boundary point of X there exist two osculating open balls of radius R , such that one is entirely*

in X and the other entirely in X^c .

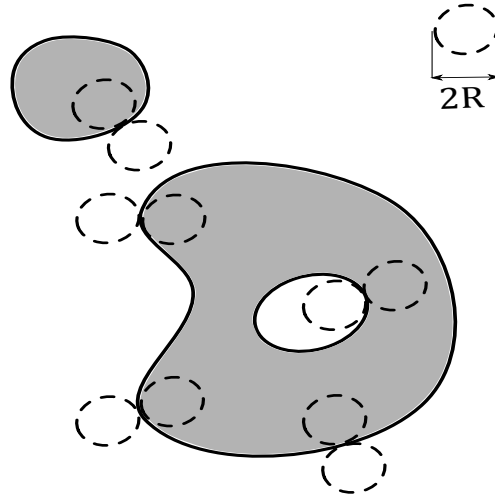


Figure 2.5: An R -regular two dimensional set

An illustration of an R -regular shape in two dimensions is given in Figure 2.5. We give an overview of the existing work on preserving shape properties when an R -regular shape is digitized in sequel.

In [81] is shown following:

Theorem 2.2.4. *There exists a bijective function $f : S \rightarrow \mathcal{G}_1(S)$, where f, f^{-1} are continuous, for an R -regular shape $S \subset \mathbb{R}^2$ and pixel size less than $\sqrt{2} \cdot R$.*

The bijective function is named *homeomorphism* and the existence of a homeomorphism between two sets is *topological equivalence* of these sets.

The existence of a tree whose nodes are connected components of S and the nodes are connected if connected components share a part of their borders is explored in [102]. The tree is named *homotopy tree* and the following is shown:

Theorem 2.2.5. *S and the set of pixels obtained by subset sampling of S have the same homotopy tree for any hexagonal grid with pixel size less than R .*

[84] considers an arbitrary dimension and the following is shown:

Theorem 2.2.6. *The Hausdorff digitization of a shape converges towards the shape when pixel size converges to zero for arbitrary dimension and arbitrary digital grid.*

In addition, the same authors show [122]:

Theorem 2.2.7. *There exists a homeomorphism between a two dimensional R -regular shape and its Hausdorff digitization if pixel size is less than $\frac{R}{2}$.*

The existence of a homeomorphism, a homotopy tree and a small distance between shape border and the border of the set consisting of sampling points

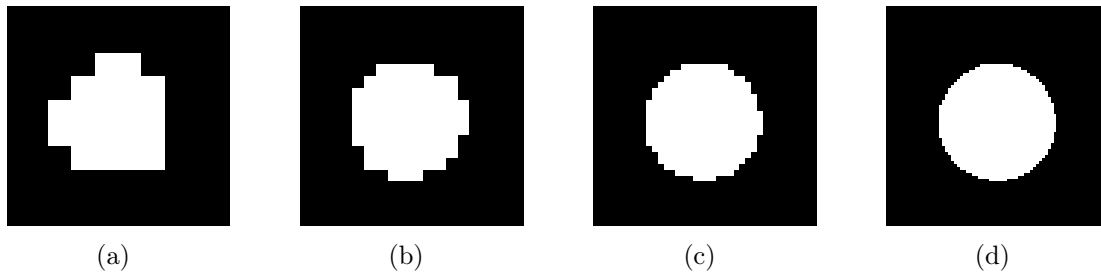


Figure 2.6: The disk from Figure 2.4(d) at two times (b), four times (c) and eight times (d) higher resolution.

provided by the Hausdorff digitization are criteria for preserving shape properties after digitization, but there are examples in which they do not provide even visual similarity. To address this problem, [118] introduce the term of strong r -similarity:

Definition 2.2.8. *Two sets $X, Y \subset \mathbb{R}^n$ are called strongly r -similar if there exists a homeomorphism $f : \mathbb{R}^n \rightarrow \mathbb{R}^n$ such that $x \in X \Leftrightarrow f(x) \in Y$ and $x \in \partial X \Rightarrow |x - f(x)| \leq r$.*

The condition of strong r -similarity implies all the described conditions. Moreover, it limits the distance between arbitrary point $x \in A$ and its homeomorphic image $f(x)$ instead of limiting distance between ∂X and $\partial \mathcal{D}(X)$ as Hausdorff distance does. In [118] authors prove several theorems which we summarize in the following theorem:

Theorem 2.2.9. *Let $R \in \mathbb{R}^+$. Then S is strongly r -similar to the union of pixels corresponding to subset sampling of S in any two dimensional grid with pixel size $r < R$.*

Theorem 2.2.9 is extended to images exposed to blurring present in real imaging conditions in [118]. Still, such a framework does not exist for higher dimension. Moreover, a counterexample showing that the topological equivalence between three or higher dimensional shape and its digitization cannot be achieved is provided [118].

From Theorem 2.2.9 it is clear that the deviation of a point belonging to S and its homeomorphic image belonging to subset sampling becomes smaller as the spatial resolution increases. This entails that the similarity between S and its subset sampling increases as the spatial resolution increases. The enhancement of visual similarity is presented in Figure 2.6 where the circle from Figure 2.4(d) is given with pixels size two times (Figure 2.6(c)) smaller, four times smaller (2.6(c)) and eight times smaller (2.6(d)).

It is clear that the digitization of a R -regular shape obtained by subset sampling approaches the true shape when pixel size is $r < R$ and decreases, i.e. the spatial resolution increases. Is this sufficient that a descriptor of a R -regular shape estimated from such digitization converges towards its true value when spatial resolution increases? The answer is: No, in general.

Multigrid convergence

The problem of the convergence of an estimation of a descriptor from its digitization towards the true value with increasing spatial resolution is named *multigrid convergence*. The multigrid convergence reduces to the problem of deriving an upper bound of the estimation at a given resolution. It has a dual significance. Having such an upper bound we can know how reliable is the estimated value in real applications and we can study the convergence of the estimated descriptor towards its true value via the upper bound.

To give a formal definition of the multigrid convergence, we assume a digitization in which the uniform spacing between grid points is equal to r , i.e. the grid resolution is $\nu = \frac{1}{r}$.

Definition 2.2.10. *Let S be a shape and $Des(S)$ a descriptor of S . Let $\widetilde{Des}_\nu(S)$ be a method for estimation of $Des(S)$ from a digitization of S in the digital grid with resolution ν . Method $\widetilde{Des}(S)$ is multigrid convergent iff:*

$$Des(S) = \lim_{\nu \rightarrow \infty} \widetilde{Des}_\nu(S). \quad (2.8)$$

In order to analyse upper bounds of the error of $\widetilde{Des}(S)$ we consider following definition:

Definition 2.2.11. *The function $f(\nu) \geq 0$ is the asymptotic complexity class $\mathcal{O}(g(\nu))$ ($f(\nu) = \mathcal{O}(g(\nu))$) iff there exists a constant $c \geq 0$ and a constant $\nu_0 \geq 0$ such that $|f(\nu)| \leq c \cdot g(\nu)$, for all $\nu \geq \nu_0$. In this case we say that $g(\nu)$ is the worst-case upper bound of $f(\nu)$.*

If f is an error measure of an estimation ($f = \widetilde{Des}_r(S) - Des(S)$) then $g(s)$ specifies a worst-case error bound of that estimation.

We point out that in almost all the literature on multigrid convergence one of two variants of the Gauss digitization is assumed and the results we describe here assume the same. The problem of multigrid convergence is a traditional problem in mathematics. It appears in works of Gauss, Dirichlet and Jordan, but upper bound errors have been improved through time, i.e. lower upper bound errors for the same descriptor have been provided. For instance, Gauss and Dirichlet had already known that the number of grid points inside a planar convex shape converges towards its area with the speed $\mathcal{O}(\frac{1}{\nu})$. This result is improved by [46]

and the worst-case upper bound $\mathcal{O}((\frac{1}{\nu})^{\frac{7}{11}} \cdot (\log \frac{1}{\nu})^{\frac{47}{22}})$ is given for convex shapes that have continuous third order derivatives and positive curvature at every point of the boundary. In [56] it is noticed that the condition on the shape border can be relaxed and that it can contain a finite number of vertices and is given even better upper bound $\mathcal{O}((\frac{1}{\nu})^{\frac{15}{11}+\epsilon})$, where $\epsilon > 0$. For an analysis and worst-case error bounds of estimation of different shape descriptors from binary images we refer to [17, 58].

Although the problem of multigrid convergence has a long tradition and is intensively explored, there are many shape analysis methods proposed and used without any analysis of their multigrid convergence such as linearity [120], squariness [88] and rectilinearity [89]. An interesting experimental evaluation of existing theoretical worst-case upper bounds of methods for shape description is given in [17]. This study shows that the results of an experimental evaluation frequently do not coincidence with the existing theoretical. This indicates that the provided theoretical worst-case error bounds are not optimal. For instance, the worst-case upper bound $\mathcal{O}(\frac{1}{\nu})$ of estimating shape perimeter given in [112] shows to be $\mathcal{O}((\frac{1}{\nu})^{\frac{4}{3}})$ in the experimental evaluation. Moreover, in [58] is made a conclusion that for the most of the provided upper bounds is not yet known if they are optimal or not and that this is an open problem.

2.3 Pixel Coverage Representation

The described traditional framework is mostly used for representing shapes and studying errors of shape analysis methods at present. Still, it shows insufficiency in many real situations and arises a need for different approaches.

The property of multigrid convergence of a method ensures that there is always a resolution increment that reduces the error to a desired value. Although intuitively appealing, the existence of such an increment does not necessarily provide the arbitrary accuracy and precision of a shape analysis method in practice. First of all, an arbitrary increment of the resolution is a theoretical procedure and cannot be conducted in practice since imaging devices are always of the limited resolution. This problem is frequently present when imaged objects are far away from the imaging device (satellite images) or when imaged objects are very small (viruses or nano-particles). Secondly, as possibilities for increasing the spatial resolution become greater, it becomes a desire to study smaller and smaller objects. In such situations the performance of shape analysis methods at limited resolutions is of great importance.

Stated problems imposed a question if there is some other, additional, information that can be provided for usage in shape analysis, apart from the one provided by binary images. This has led the scientific research into alternative directions for

improving accuracy and precision of image analysis methods. Using coverage of a pixel by a shape under consideration has been the main direction of this research.

A strong motivation for using pixel coverage by a shape in the shape analysis tasks can be found in [54]. The authors showed that the error free reconstruction of a polygonal shape is possible if the covered area by a shape is known for every pixel and the spatial resolution is sufficiently high. It is shown that, at spatial resolution ν and gray level resolution b , the maximal error of reconstruction of shapes is:

$$\frac{1}{\sqrt{3}\nu(2^b - 2)^2}. \quad (2.9)$$

The important point to note here is that the provided upper bound error decreases faster with b than with ν .

In remote sensing the size of pixels range from a couple of meters to a couple of kilometers due to the great distance between imaged objects and imaging device. This causes that every pixel is in a large number of cases covered by several objects and assigning a pixel to just one object causes large errors in further processing. To reduce errors the idea of *fractional pixels* is introduced. A fractional pixel is a pixel which gray scale value expresses how large pixel fraction is covered by an object. Fractional pixels can be estimated using linear mixture models which generally result in a poor performance or using neural networks which are able to capture complex structures in the data as presented in [52].

An additional field of practical application of image analysis in which partially covered spels attract significant attention is processing of tomographic images. Due to inhomogeneities of regions of spels and sensitivity and finesse of imaged objects, determining whether a spel belongs to an object is a difficult issue. The problem, and the need for sub-voxel precision, is well illustrated in [78], where it is shown that consistently misplacing the tissue borders in a brain volume having voxels of size 1 mm^3 by only a single voxel in image, resulted in volume errors of approximately 30% for white matter, 40% for grey matter and 60% for cerebrospinal fluid in a brain. This has led to the various methods for estimating portion of each of the tissues that is contained in a voxel. An approach based on expectation-maximization in such estimation is presented in [61].

Although providing improvements in specific applications, the described work is missing a well defined mathematical model for abstracting the essential data. The absence of such model significantly obscures the development of general shape analysis methods which are not related to a specific application or imaging conditions.

The coverage model

A binary image can be understood as a characteristic function of a shape that assigns value 1 to points which belong to the shape and 0 in the opposite. In a digital setting, the described characteristic function is applied to the whole Voronoi regions corresponding to sampling points. The problem arises at the border pixels which do not completely belong to a shape, nor its background. They belong to the shape to a certain extent, while partially belonging to the shape complement, i.e. background. A mathematical field which deals with sets to which elements partly belong is *fuzzy set theory* and, having in mind aforementioned, it is natural that a mathematical model for abstracting pixel coverage information is developed within its framework.

A fuzzy subset F of a reference set D is a set of ordered pairs $F = \{(x, \mu_F(x))\}$, where $\mu_F : D \rightarrow [0, 1]$ is the membership function of F [132]. In other words, a fuzzy set is a set whose membership function maps an arbitrary reference set to the interval of real numbers $[0, 1]$, where elements with the membership function equal to 1 are completely in the set, while those with the membership function equal to 0 are completely in its complement.

In the frame of fuzzy sets a coverage representation of a subset of \mathbb{R}^n is proposed:

Definition 2.3.1. [109] *Given a partition $\Sigma = \{\sigma_i\}_{i \in I}$ of a reference set D , a coverage representation of a set $X \subset D$ on Σ is a fuzzy subset $\{(\sigma_i, \alpha(\sigma_i)) \mid \sigma_i \in \Sigma\}$, such that $\alpha(\sigma_i) = \frac{|\sigma_i \cap X|}{|\sigma_i|}$, where $|X|$ denotes the cardinal number of X .*

When the theoretical model is used in image processing, it is considered that the reference set D is the Euclidean space \mathbb{R}^n . Σ corresponds to the collection of all the Voronoi regions, usually defined by the set of integer points \mathbb{Z}^n . A pixel, voxel or spel (in more than three dimension) is indicated by its integer point $\mathbf{i}(i_1, i_2, \dots, i_n) \in \mathbb{Z}^n$ and denoted as $\sigma_{i_1, i_2, \dots, i_n}$.

The proposed theoretical framework has enabled development and improvement of many shape analysis methods. For example, the area of a two dimensional shape S can be estimated from its coverage representation using the definition of area of discrete fuzzy set from [85] as

$$A(S) = \sum_{\mathbf{i}(i_1, i_2) \in S} \alpha(\sigma_{i_1, i_2}). \quad (2.10)$$

The same definition can be applied for estimating volume $V(S)$ of a three dimensional shape.

In [110, 111] is shown that, for a two or three dimensional shape S , usage of coverage model instead of binary images significantly improves the precision keeping accuracy on the same, high level in estimation of area, perimeter and the

descriptor named *compactness* computed as:

$$\frac{P^2(S)}{4\pi \cdot A(S)}, \quad (2.11)$$

or

$$\frac{P(S)}{\sqrt[3]{36\pi \cdot V(S)}}. \quad (2.12)$$

A method for improving shape moment estimation from digital images is presented in [106]. The usage of coverage representation for computing shape signatures from digital images is examined in [12, 49] and multiple improvement of accuracy and precision shown when this model is used. A method that further improves shape boundary length estimation from pixel coverage representation is examined in [107]. Tests on real images show that the maximal error of estimation is reduced 5 to 60 times by method that utilizes coverage values comparing to 5 best known and best performing local methods based on binary images.

Motivated by the described results, we explore the usage of coverage model for estimation of Feret's diameter from the digital image representations of two dimensional objects in the thesis. The work related to this problem is presented in [27, 28]. In accordance with Definition 2.3.1, we use the following digitization model for this purpose:

Definition 2.3.2. [107] *In the integer grid, the pixel coverage digitization of a shape $S \subset \mathbb{R}^2$ is:*

$$\mathcal{D}(S) = \left\{ \left((i, j), \alpha_{i,j} \right) \mid (i, j) \in \mathbb{Z}^2 \right\}, \quad \alpha_{i,j} = \frac{A(p_{i,j} \cap S)}{A(p_{i,j})}. \quad (2.13)$$



Figure 2.7: The binary and pixel coverage digitization of a disk.

Coverage values $\alpha_{i,j}$ in the digitization model can be computed for an analytically defined two dimensional shape by computing the intersecting points of its

border with the digital grid. Knowing the intersecting points, the analytic expression is integrated to compute the area that shape covers in every pixel. This is how we computed $\alpha_{i,j}$ in experiments on synthetic images. A binary representation and the coverage values computed in this manner for a disk are given in Figure 2.7.

For the more realistic evaluation of Feret’s diameter estimation of a shape from its digital image representation, a segmentation algorithm that provides approximate values of $\alpha_{i,j}$ (pixel coverage segmentation algorithm) is needed. There are several pixel coverage segmentation algorithms presented in the literature that enable application of listed shape analysis methods based on the coverage in varying conditions and applications. One such algorithm is proposed in [107]. The algorithm is based on double thresholding which is suitable for usage when an object and its background are well separable and imaging device has a linear response. A method based on local unmixing for estimating coverage values from any binary image shape representation is proposed in [64,108]. The importance of this method is that it transfers good properties of a well chosen binary segmentation method on pixel coverage digitization. In [69], a graph theoretic framework for coverage segmentation is given. The framework enables estimation of coverage values in any dimension, and images sampled on non-Cartesian or spatially variant grids.

In the following sections, we give description of the method based on double thresholding and the method based on local unmixing since we use them to obtain coverage values from real images in our experimental evaluation.

Coverage segmentation based on double thresholding

There are many imaging devices that provide approximate coverage values. For example, the devices whose output is the integral of photons over finite sized image sensors as present in a digital camera. When there is no variations of gray levels caused by object properties which are not relevant for consideration, e.g. by object texture, it is possible to map image intensity values into coverage values. The method based on double thresholding provides such mapping.

Let us denote by f the intensity of the imaged foreground (object) and with b the imaged background. The image intensity $I_{i,j}$ can be modeled as a convex combination of f and b :

$$I_{i,j} = \alpha_{i,j} \cdot f + (1 - \alpha_{i,j}) \cdot b \Rightarrow \alpha_{i,j} = \frac{I_{i,j} - b}{f - b}. \quad (2.14)$$

Not knowing the values f and b , the algorithm loops over all the possible thresholds b' and all the pixels whose value is lower than b' are considered as background. The complement of the set of pixels categorized as the background by b' is eroded by the $3 \times 3 \times 3 \times \dots \times 3$ structuring element and every pixel in the

obtained set is considered to be foreground. The threshold value f' for foreground is chosen as the minimal gray value among gray values of pixels obtained by the erosion. The border pixels between foreground and background are considered to be those which are removed by the erosion. The structuring element for the erosion is suitably chosen to be $3 \times 3 \times 3 \times \dots \times 3$ since the object border should not be more than one pixel wide. In order to remove the individual dark noise points that distort appropriate selection of f' morphological closing, i.e. a dilation followed by the erosion by the same structuring element, before selecting f' is performed. At every step, the difference $l = f' - b'$ is computed. The threshold values f' and b' giving the largest difference are chosen and coverage values according to Equation 2.14 are calculated according to them. An example of a digital image of black disks and the gray scale image that represents their coverage values computed by the algorithm is presented in Figure 2.8.

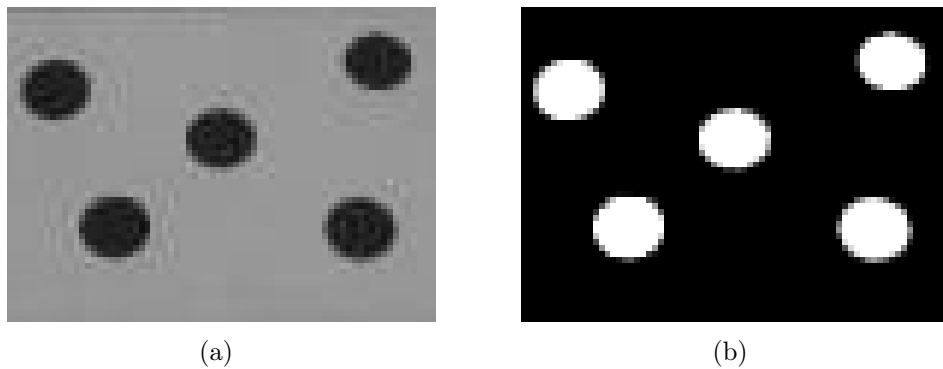


Figure 2.8: A digital image of black disks (a) and the gray scale image that represents their coverage values computed by the algorithm based on double thresholding (b).

Coverage segmentation based on local unmixing

The method based on local unmixing uses a binary image representation to compute coverage values. Assuming that the correct class is assigned to the pixels which are completely covered by one object, the method utilizes this assignment to estimate the coverage values of pixels being intersected by the border of some object.

Having the binary image representation of a shape, the next step is to designate all the pixels intersected by the shape border. In order to do this, all pixels which are neighbors with a pixel of a class different from it are collected in the set B . It is assumed that the set of pixels not belonging to just one object are subset of B .

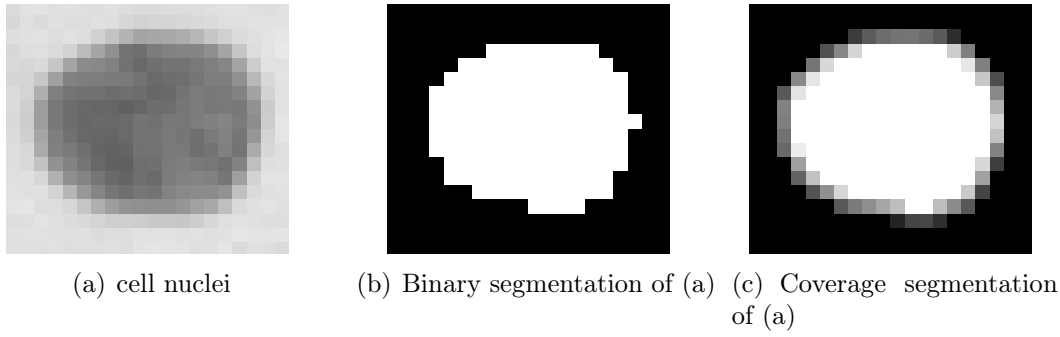


Figure 2.9: An image of a cell nuclei, its binary image representation and pixel coverage representation computed by the algorithm based on local unmixing.

It is assumed that the value of a mixed pixel $I(p)$ is a convex combination of the image values corresponding to pure classes c_k covering the pixel under consideration: $I(p) = \sum_{k=1}^m \alpha_k \cdot c_k$, $\sum_{k=1}^m \alpha_k = 1$. Besides, it is assumed that the coefficients in the combination correspond to the proportion of the pixel coverage by a class denoted with α_k . In a noise free conditions and if the number of equations is not bigger than the number of classes m , coverage values are computed by solving system of linear equations.

However, in real imaging conditions, it is not certain that there exists solution of the problem due to the presence of noise. This is the reason why the problem is converted into the problem of minimizing the function:

$$F(\alpha_1, \alpha_2, \dots, \alpha_m, \lambda) = \|I(p) - \sum_{k=1}^m \alpha_k c_k\|_2^2 + \lambda \cdot (\sum_{k=1}^m \alpha_k - 1). \quad (2.15)$$

In general, the set of non-pure, or mixed, pixels should be an one-pixel thick set. Nevertheless, due to a presence of noise, some of elements of B are assigned partial coverage value, although they should be pure. To reduce this consequence of noise, the thinning of the set of mixed pixels is performed by assigning the pure class to pixels in B which are at a smallest distance to one pure class. This is done until a one pixel thick set B is reached. In Figure 2.9 is given an image of a cell nuclei, its binary image representation and the pixel coverage digitization computed by the algorithm.

2.4 Mathematical Morphology

Mathematical morphology is one more field in image processing developed to treat the shapes of studied objects. The original problem of mathematical morphology

arised in the mining industry and we shortly describe it in following.

It was required that rocks be characterized based on their shapes using digital images. The rocks were porous which made it hard to discern between the relevant image spels representing the shapes of rocks and those which represent the cavities in rocks and are irrelevant for the consideration. Operations on digital images were required to remove spels representing cavities, at the same time preserving spels representing the shapes of rocks. Mathematical morphology provides such operations.

The main idea for a solution was introduced by French scientists Georges Matheron and Jean Serra in mid 1960 [71, 101, 102]. The idea is based on the Minkowski sum and difference of two sets.

Definition 2.4.1. [73] *Let X and Y be two sets of position vectors. Then, the Minkowski sum of X and Y is given by:*

$$X + Y = \{\mathbf{x} + \mathbf{y} \mid \mathbf{x} \in X \text{ and } \mathbf{y} \in Y\}, \quad (2.16)$$

and the Minkowski difference of X and Y is given by

$$X - Y = \{\mathbf{x} - \mathbf{y} \mid \mathbf{x} \in X \text{ and } \mathbf{y} \in Y\}. \quad (2.17)$$

Generally speaking, if X is the set of position vectors of points which represent an object, a set Y can be suitably chosen and positioned so that the Minkowski sum adds points to remove potential redundant holes in X , i.e., representing aforementioned cavities in rocks. Similarly, it is possible that there are irrelevant points in X and the Minkowski difference can be used to remove them.

In mathematical morphology, the set Y is called *structuring element*. In sequel, we denote a structuring element with O and give the definitions of the basic morphological operations:

Definition 2.4.2. [71] *The dilation of a set X by a structuring element O is given by:*

$$X \oplus O = \bigcup_{\mathbf{p} \in O} X_{\mathbf{p}}, \quad (2.18)$$

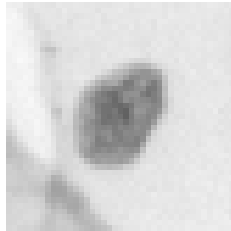
the erosion of a set X by a structuring element O is given by:

$$X \ominus O = \bigcap_{\mathbf{p} \in O} X_{\mathbf{p}}, \quad (2.19)$$

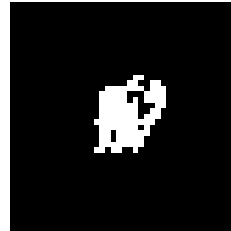
where $X_{\mathbf{p}}$ is the translation of a set X along vector \mathbf{p} : $X_{\mathbf{p}} = \{\mathbf{x} + \mathbf{p} \mid \mathbf{x} \in X\}$.

Since satisfying $X \oplus O = (X^c \ominus \check{O})^c$, where \check{O} is the reflection of O , the operations of dilation and erosion are dual. In image processing, they are usually preceded by the process of segmentation. Due to this, the set X consists of position

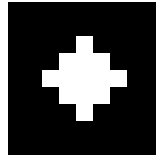
vectors of image spels representing an object. The structuring element O is then a set of position vectors of spels conveniently chosen in the same digital grid as X . Morphological operations are performed not just to remove the irrelevant or emphasize relevant data that exist in the real world, but also to remove or emphasize the data incurred during the image acquisition, not present in the real world. For instance, they are frequently used to remove image noise or other degradation.



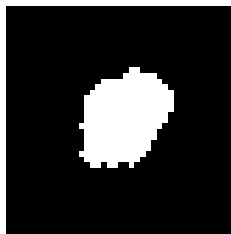
(a) A microscopic image of a cell nuclei imaged at resolution $2.0px/\mu m$.



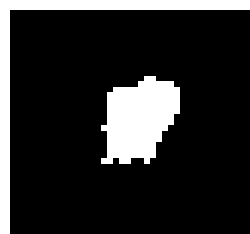
(b) Thresholding of (a) resulted in a poor segmentation adding holes and regions of non-convexities at border.



(c) A structuring element.



(d) Resulting image after dilating (b) with structuring element (c) much better approximates the shape of (a).



(e) Erosion of (d) by the same structuring element, i.e. opening of (b), keeps the size of (b).

Figure 2.10: An illustration of using dilation to remove holes disturbing the original shape of a cell after segmentation. The dilation makes the object larger, so opening can be performed to keep the size, but remove holes. Due to duality of dilation and erosion, if we would switch positions of black and white pixels in (b) and perform erosion, the result would be the same except that black pixels would represent the cells shape.

For an illustration of performing dilation and erosion on a digital image, we give

Figure 2.10. A digital image representation of a cell nuclei obtained at resolution $2.0 \frac{\mu\text{x}}{\mu\text{m}}$ given in Figure 2.10(a) is thresholded at 65 % of maximal image intensity value. The resulting image shown in Figure 2.10(b) poorly approximates the shape of cell nuclei since it contains holes and non convex regions in the border. The dilation of thresholded image by the structuring element given in Figure 2.10(c) provides much better approximation of the shape, as presented in Figure 2.10(d). Due to the duality of dilation and erosion, the result would be the same if we have replaced the white pixels with black and vice versa and performed the erosion with the same, centrally symmetrical, structuring element.

We point out that, besides removing holes, a dilation makes an object larger while an erosion makes an object smaller. The white region that represents the cell nuclei in binary image in Figure 2.10(d) is larger than the one in Figure 2.10(b). To restore the white region to the original size, once the holes are removed by the dilation, the erosion by the same structuring element can be performed. The result of such erosion is presented in Figure 2.10(e). Combinations of the two basic morphological operations, with the same structuring element, lead to two other important morphological operators *opening* and *closing*:

Definition 2.4.3. *The opening of a set X by a structuring element O is given by:*

$$X \circ O = (X \oplus O) \ominus O, \quad (2.20)$$

the closing of a set X by a structuring element O is given by:

$$X \bullet O = (X \ominus O) \oplus O. \quad (2.21)$$

During 1960s and during most of 1970s mathematical morphology was based on the classical set-theory. Commonly, pixels with value 1 were considered as the elements of a set and pixels with value 0 as the elements of the set complement as done in [101] for example. This limited mathematical morphology only on binary images, although the most of digital image representations assume usage of gray levels. Such limitation is overcome by proposing morphological operations for gray level images in [102] and further considering them in [119].

The basic morphological operations for gray scale images are given by the following definition.

Definition 2.4.4. *The grayscale morphological dilation and erosion of a function $f : D \rightarrow \mathbb{R}$ by a flat structuring element O are respectively defined as:*

$$f \oplus O(\mathbf{x}) = \max_{\mathbf{z} \in O} (f(\mathbf{x} - \mathbf{z})), \quad \mathbf{x} \in D \quad (2.22)$$

$$f \ominus O(\mathbf{x}) = \min_{\mathbf{z} \in O} (f(\mathbf{x} - \mathbf{z})), \quad \mathbf{x} \in D. \quad (2.23)$$

The defined operations assign the maximal or minimal value in the neighborhood defined by a structuring element to every pixel when applied on two dimensional digital images. A simple illustration of usage of gray scale morphology for removing noise in a two dimensional digital image is given in Figure 2.11. Figure 2.11(a) represents the two cells of *Escherichia coli* which pixels mix with the background noise. After performing the erosion by the structuring element presented in Figure 2.11(b), the pixels which represent the noise are removed. For improved visualization, the images are normalized according to the formula $norm(g) = \frac{g - \min(g)}{\max(g) - \min(g)}$, where g is the image function. The resulting image is given in Figure 2.11(c). We notice that Definition 2.4.4 reduces to 2.4.2 if image codomain contains just two values, as for binary images.

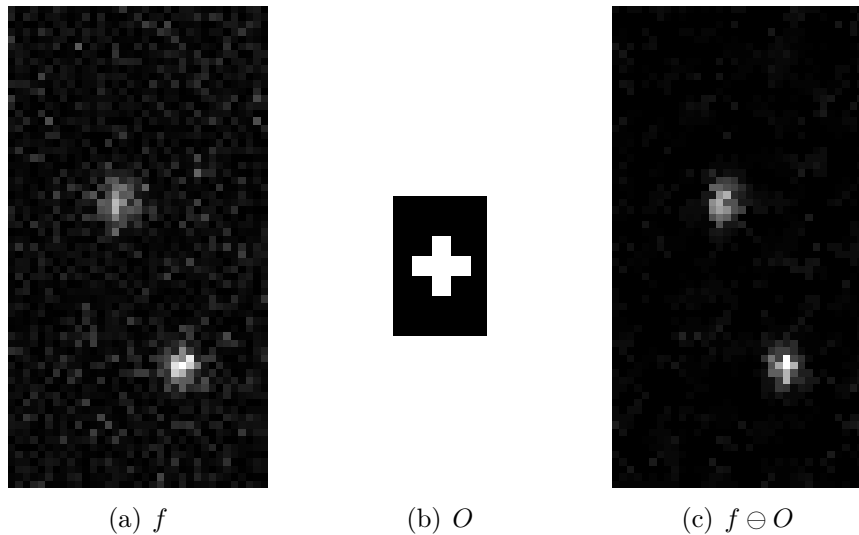


Figure 2.11: (a) An image of *Escherichia coli* cells in which background noise mixes with cell pixels. (b) A structuring element. (c) Dark regions in image are spread and noise pixels removed by performing erosion. Both images are normalized according to the formula $norm(g) = \frac{g - \min(g)}{\max(g) - \min(g)}$, where g is an image function.

Assigning to a pixel the maximal or minimal value in a neighborhood is the procedure that corresponds to spreading of the existing dark or bright gray values in an image, but does not enable changes of these values before the assignment. The following definitions enable to increase or reduce deliberately gray values in a neighborhood before the assignment and thereby provide more freedom in setting an intensity to a desired value.

Definition 2.4.5. [102] A structuring function \mathcal{K} on a support $O \subset \mathbb{R}^n$ is a function $\mathcal{K} : O \rightarrow \mathbb{R}$.

Definition 2.4.6. *The gray scale dilation and erosion of a function $f : D \rightarrow \mathbb{R}$ by a structuring function \mathcal{K} are given by:*

$$\delta_{\mathcal{K}}(f)(\mathbf{x}) = \sup_{\mathbf{z} \in O} (f(\mathbf{x} - \mathbf{z}) + \mathcal{K}(\mathbf{z})), \quad \mathbf{x} \in D,$$

$$\varepsilon_{\mathcal{K}}(f)(\mathbf{x}) = \inf_{\mathbf{z} \in O} (f(\mathbf{x} - \mathbf{z}) - \mathcal{K}(\mathbf{z})), \quad \mathbf{x} \in D.$$

Since described operations were introduced, the simple idea of mathematical morphology found application in many fields of image processing. A number of exquisite books on usage of mathematical morphology in image analysis exist such as [114] and [75]. Together with their applications in different areas, various theoretical frameworks were developed for mathematical morphology simplifying studying of its properties and its usage. We here list just some of the most crucial. A theoretical framework based on complete lattices is given in [41]. Besides that, mathematical morphology is defined on structures such as multivalued images [3], graphs [43, 127] and manifolds [40].

Adaptive mathematical morphology

When dilations and erosions of digital images have begun to be used, one structuring element or function has been used for every point in an image. A structuring element or a function which is the same for every image spel is named *rigid* [19].

Digital image data representing an object property frequently can be variable, although the object property does not change. For instance, identical objects in reality can appear different in size in different parts of an image due to image perspective, or intensity values representing them can differ due to uneven illumination. Real imaging conditions frequently assume uneven illumination, presence of noise and similar difficulties. This makes it hard and frequently impossible to extract relevant image data without having more freedom in treating spels when morphological operations are performed. It has become of interest to define structuring elements and functions that adapt to local properties in an image. Such structuring elements and functions are named *adaptive* and they change their shape or values depending on the position, shape and values of image data to be removed or emphasized. *Adaptive mathematical morphology* is a field of mathematical morphology in which rigid structuring elements and functions can be replaced by adaptive.

To illustrate the basic idea of adaptive mathematical morphology, we give Figure 2.12 taken from [24]. The figure illustrates forming a type of adaptive structuring elements named *general adaptive neighborhoods* [23]. A general adaptive neighborhood is defined for every image point such that it is connected and contains points with similar properties. More precisely, h is a *criterion mapping* that

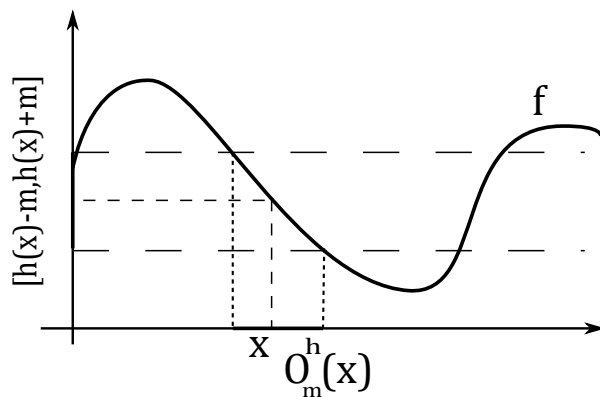


Figure 2.12: Forming a general adaptive neighborhood $O_m^h(x)$. h is a criterion mapping related to a local image property embraced by the image function f and m is homogeneity tolerance that defines how much a property expressed by h can vary within a general adaptive neighborhood.

expresses a local property of the image embraced by an image function. Such local property can be luminance, for instance. m is *homogeneity tolerance* that defines how much a property expressed by h can vary within a general adaptive neighborhood. The local adaptive neighborhood $O_m^h(x)$ is chosen around point x such that it is connected and can be adjusted by choosing the parameter m .

Two categories of adaptive structuring elements are defined in [83]. In the first category fall the structuring elements which adapt only to the position in the image domain. They are named *extrinsic* or *local-adaptive* structuring elements. Probably the earliest example of using an extrinsic structuring element and adaptive mathematical morphology in general is for analyzing the vehicles whose size in images vary across spatial positions due to the distance from an imaging device [5]. To follow the size of vehicles, structuring element vary linearly with their vertical position. In the similar manner structuring elements are designed in [18, 125].

The second category of adaptive structuring elements includes *intrinsic* or *input adaptive* structuring elements that are dependent on the image content beside being dependent on the location in an image. Approaches for defining input adaptive structuring elements are diverse and we list only a few. An approach from the second category is to define a general adaptive neighborhood [23] in the manner as already described. The most known are *morphological amoebas* [62] defined via *amoeba distance* between pixels p and q for which exists path of adjacent pixels $\mathcal{P}(p, q) = \{p_1, p_2, \dots, p_n\}$ such that $p = p_1$ and $q = p_n$:

$$d_A(p, q) = \min_{\mathcal{P}(p, q)} \sum_{i=1}^{i=n} (d(p_i, p_{i+1}) + \lambda |f(p_i) - f(p_{i+1})|), \quad (2.24)$$

where d is a distance and λ is a constant. The morphological amoeba is a structuring element that decreases in its size at pixels close to edges. This is because d_A is high due to high differences in intensity values in image regions corresponding to edges:

$$Am_r(p) = \{q \mid d_A(p, q) < r\}, \quad r > 0. \quad (2.25)$$

Another approach for defining a structuring element that decreases its size at pixels close to the regions at which the differences of pixel intensities are high is to compute *saliency map* of an image and relate radius of the structuring element to it. The saliency map is an image in which image intensity grows with the smaller distance of the pixel to an edge and the magnitude of that edge. The radius of *saliency adaptive* structuring elements is computed directly on saliency maps in [20] and shown that such structuring elements are more uniform in shape, have fewer holes, and are less sensitive to noise than the morphological amoebas.

Adaptive structuring functions are not so well explored and there exist only a few methods for computing them. The existing approaches are mainly extensions of the classical and well explored filtering methods for removing noise or extracting edges and corners in images. *Bilateral filtering* consists of smoothing pixel intensities while preserving edges in images by means of nonlinear combinations of nearby image intensities. This approach is related to the adaptive structuring functions and *spatially variant bilateral* structuring functions defined in [1]. *Non local image filtering* consists of computing a weighted average of different parts of images, mainly to remove noise. This approach is extended to *non local* structuring functions in [97, 124]. In [2] different distances are examined to define adaptive structuring functions based on random walks in which the step from one point to another depends on the distance between them.

Motivated by the general idea of adaptive mathematical morphology, we explore usage of adaptive structuring functions in Chapter 4 to relate morphological distances to relevant data in digital images. Although the exploration is grounded in adaptive mathematical morphology, we use a different approach than any of the existing. Instead of observing a single image to define a structuring function, we observe two images f_1 and f_2 which should be compared. More precisely, we relate structuring function to $|f_1 - f_2|$, which is the essential data for comparison.

2.5 Distances in Image Processing

Let D be a non-empty set. A *distance* is a function $d : D \times D \rightarrow [0, \infty)$. A distance is called a *metric* on D if for arbitrary elements x, y, z from X the following properties hold:

1. *Separability*:

$$d(x, y) = 0 \Leftrightarrow x = y$$

2. *Symmetry*:

$$d(x, y) = d(y, x)$$

3. *Triangle inequality*:

$$d(x, y) + d(y, z) \geq d(x, z).$$

The pair (D, d) is usually called a *metric space*. It is not necessary that d satisfies all the conditions 1. – 3. to be used in image processing. If d satisfies symmetry and triangle inequality, it is named *pseudometric*. If d satisfies separability and symmetry, it is named *semimetric*.

Distances between images are one of the oldest and the most useful image analysis tools. They have been used in image processing since its raise in 1960s. Image segmentation, image retrieval, object identification, recognition and classification are just some of the subfields in which distances play a significant role. A distance that is suitable for all the situations when comparing image data does not exist. Which distance is the best for a specific application depends on many circumstances. Comparison of variety of properties of objects, diverse objects represented by digital images, diverse conditions of imaging causing noise and degradation are just some of the factors that caused usage of many different distances in image processing. For an exhaustive overview of existing distances we refer to [25]. There exists a constant need for original approaches to define new and modify the existing distances due to their continual spread of usage. In sequel, we give a review of widely used distances in image processing that will be used later in the thesis.

Let $\mathbf{x}(x_1, x_2, \dots, x_n), \mathbf{y}(y_1, y_2, \dots, y_n) \in \mathbb{R}^n$ and $n \in \mathbb{N}$. Probably the most widely used distance in image processing is the *Euclidean metric*:

$$d_E(\mathbf{x}, \mathbf{y}) = \left(\sum_{i=1}^n (x_i - y_i)^2 \right)^{\frac{1}{2}}. \quad (2.26)$$

The Euclidean metric belongs to L_p *metrics* or *Minkowski distances* defined as:

$$L_p(\mathbf{x}, \mathbf{y}) = \left(\sum_{i=1}^n |x_i - y_i|^p \right)^{\frac{1}{p}}, \quad p > 0. \quad (2.27)$$

After for $p = 2$, L_p metrics are mostly used for $p = 1$ and for $p \rightarrow \infty$. L_1 is named the *city block distance*. When $p \rightarrow +\infty$, L_p converges toward the *Chebyshev* or *chessboard distance*:

$$L_\infty = \max_{i=1,2,\dots,n} \{|x_i - y_i|\}. \quad (2.28)$$

So far stated distances belong to the class of distances defined between points for which is frequently used name *point to point distances*. A point to point distance on a set D can be used to define a *point to set distance* between a point $\mathbf{a} \in D$ and a non-empty subset X of D :

$$d(\mathbf{a}, X) = \inf_{\mathbf{x} \in X} (d(\mathbf{a}, \mathbf{x})). \quad (2.29)$$

Let Y be another non-empty subset of D . To define a *set to set distance* for comparing properties of X and Y , a point to set distance is frequently used. The set to set distance considered the earliest by most of the authors in image processing appears in the PhD thesis of Pompeiu from 1905 [82] in a form similar as given by the formal definition of Hausdorff in his famous book from 1914 [38]:

$$d_H(X, Y) = \max\{\sup_{\mathbf{x} \in X} (d(\mathbf{x}, Y)), \sup_{\mathbf{y} \in Y} (d(\mathbf{y}, X))\}. \quad (2.30)$$

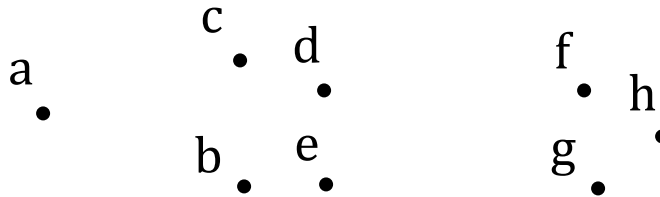


Figure 2.13: Hausdorff distance between $\{\mathbf{a}, \mathbf{b}, \mathbf{c}, \mathbf{d}, \mathbf{e}\}$ and $\{\mathbf{f}, \mathbf{g}, \mathbf{h}\}$ depends only on the distance of the point \mathbf{a} to $\{\mathbf{f}, \mathbf{g}, \mathbf{h}\}$. Other points are not relevant and due to this $d_H(\{\mathbf{a}\}, \{\mathbf{f}\}) = d_H(\{\mathbf{a}\}, \{\mathbf{f}, \mathbf{g}, \mathbf{h}\}) = d_H(\{\mathbf{a}, \mathbf{b}, \mathbf{c}, \mathbf{d}, \mathbf{e}\}, \{\mathbf{f}, \mathbf{g}, \mathbf{h}\})$.

Usually, d_H is called the *Hausdorff distance* or the *Hausdorff metric* because satisfies metric properties when d is a metric and X and Y are compact sets. Some authors use the name *Hausdorff-Pompeiu metric* or the *Pompeiu-Hausdorff metric* [4,9]. Although having the impressive range of usage in different disciplines [4], the Hausdorff distance has a strong drawback for many usages in image processing. In particular, $d_H(X, Y)$ depends exclusively on the point from $X \cup Y$ that is furthest from X and Y . To illustrate this, let us observe $X = \{\mathbf{a}, \mathbf{b}, \mathbf{c}, \mathbf{d}, \mathbf{e}\}$ and $Y = \{\mathbf{f}, \mathbf{g}, \mathbf{h}\}$ presented in Figure 2.13. For these sets is valid:

$$\begin{aligned} d_H(\{\mathbf{a}\}, \{\mathbf{f}\}) &= d_H(\{\mathbf{a}\}, \{\mathbf{f}, \mathbf{g}, \mathbf{h}\}) = \\ d_H(\{\mathbf{a}, \mathbf{b}, \mathbf{c}\}, \{\mathbf{f}, \mathbf{g}, \mathbf{h}\}) &= d_H(\{\mathbf{a}, \mathbf{b}, \mathbf{c}, \mathbf{d}, \mathbf{e}\}, \{\mathbf{f}, \mathbf{g}, \mathbf{h}\}). \end{aligned} \quad (2.31)$$

The problem escalates when the point on which the Hausdorff distance between two sets depends represents an outlier. This is frequently case in image processing

since a digital image can be corrupted by noise or other degradation caused by imaging conditions.

In order that a set to set distance be sensitive to relevant changes of two sets, point to set distances are usually summed or averaged over points and sets. A distance computed in this manner, which is not a metric since it does not satisfy the triangle inequality, named the *sum of minimal distances* is proposed in [79] and its theoretical properties are examined in [30]:

$$d_{SMD}(X, Y) = \frac{1}{2} \left(\sum_{\mathbf{x} \in X} d(\mathbf{x}, Y) + \sum_{\mathbf{y} \in Y} d(\mathbf{y}, X) \right). \quad (2.32)$$

It is easy to conclude that $d_{SMD}(X, Y)$ is sensitive to internal changes of sets X and Y and will be different for sets of points from Figure 2.13 for which d_H stays the same.

One widely used distance in image processing which is not based on a point to set distance is the *symmetric difference* [55] defined for finite sets F_1 and F_2 by:

$$d_{SD}(F_1, F_2) = |F_1 \Delta F_2|, \quad (2.33)$$

where $F_1 \Delta F_2 = (F_1 \cup F_2) \setminus (F_1 \cap F_2)$ and $|F|$ denotes the number of elements of F . The main disadvantage of the symmetric difference is that it takes into account only the number of points inside sets and is independent on their geometrical properties.

When set to set distances are used for comparing digital image data, a digital image is frequently observed as a fuzzy set and the notion of α -cut used:

Definition 2.5.1. [132] *An α -cut of a fuzzy set \mathcal{F} is the (crisp) set ${}^\alpha F = \{\mathbf{x} \in X \mid \mu_{\mathcal{F}}(\mathbf{x}) \geq \alpha\}$, $\alpha \in (0, 1]$.*

One of *fuzzification principles* used to extend a function \hat{f} defined for (crisp) sets to a function f defined for fuzzy sets is:

$$f(\mathcal{F}) = \int_0^1 \hat{f}({}^\alpha \mathcal{F}) d\alpha. \quad (2.34)$$

Every quantification value of a gray scale image is observed as an value of α . Digital images are observed as fuzzy sets and Equation 2.34 is used to compute set to set distances between them in [22, 65, 96] for instance.

Frequently, image intensity values are observed as points and a point to point distance applied as done in [34, 63, 116]. For instance, the Minkowski distances are used for comparing two gray value images $f, g : D \rightarrow \mathbb{R}$ in this manner by computing:

$$L_p(f, g) = \left(\sum_{(x_1, x_2, \dots, x_n) \in D} |f(x_1, x_2, \dots, x_n) - g(x_1, x_2, \dots, x_n)|^p \right)^{\frac{1}{p}}, \quad p > 0. \quad (2.35)$$

Motivation for proposing morphological distances

In general, a distance used for comparing image data does not provide a possibility to be adjusted to a specific change in the shape of objects of interest. To clearly illustrate this and motivate the need for morphological distances, we compute L_1 , d_{SD} , d_{SMD} and d_H between finite sets of pixels representing Gauss \mathcal{G}_2 digitization of two-dimensional objects. Figure 2.14 gives a square and its modifications for which we compute the distances. In particular, Figure 2.14(a) shows the square. In Figure 2.14(b) it is divided on two components by removing one pixel wide segment. In Figure 2.14(c), one pixel wide segment is removed from the border. Two line segments are added perpendicular to the border changing the convexity in Figure 2.14(d). One pixel wide segment is added to the border in Figure 2.14(e). L_1 is mathematically equivalent with d_{SD} when both are defined. Regardless, we observe L_1 and d_{SD} because they are both extensively used in image processing and they always appear in the literature separately. As in [63], we compute L_1 between images $f, g : D \rightarrow \mathbb{R}$ as $L_1(f, g) = \sum_{x_1, x_2 \in D} |f(x_1, x_2) - g(x_1, x_2)|$, where $f(x_1, x_2), g(x_1, x_2)$ take value 1 at points which represent object and 0 otherwise. The rest of the distances are computed on the coordinates of points representing objects. We emphasize that the concept could easily be extended to more gray levels, for example, using Definition 2.5.1 and Equation 2.34. For easy verification, we use L_∞ point to point distance to compute d_H and d_{SMD} . Obtained results are given in Table 2.1.

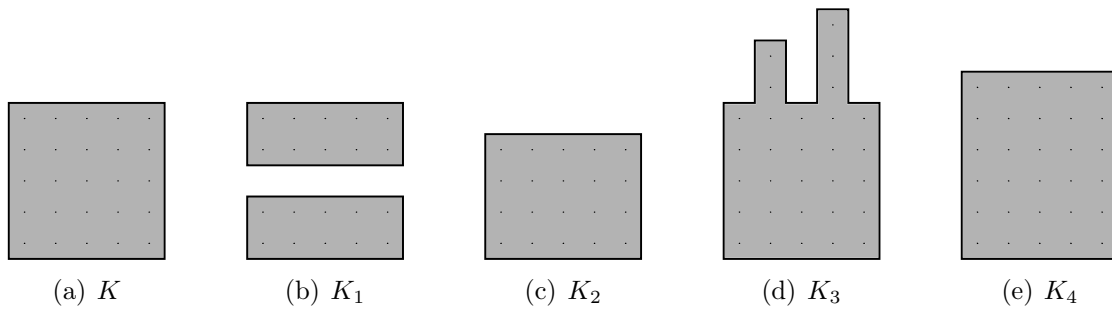


Figure 2.14: A square K and its changes in connectivity (K_1), size (K_2 and K_4) and convexity (K_3).

By just observing the values in the table, it is not possible to make conclusions on a particular property in which K and K_i , $i \in \{1, \dots, 4\}$ differ. Moreover, $L_1 = d_{SD}$ does not change the value. Because it depends on the point from $K \cup K_i$ that is furthest from K and K_i , only the value of d_H that stands out from the rest in the row indicates a protrusion or a strong change of the size. As shape is an

Table 2.1: Different distances computed for Figure 2.14

	K, K_1	K, K_2	K, K_3	K, K_4
$L_1 = d_{SD}$	5	5	5	5
d_{SMD}	2.5	2.5	4.5	2.5
d_H	1	1	3	1

important property of an object, dealing with its geometry is a crucial task when objects are compared by comparing their digital image representation.

Existing morphological Distances

The term *morphological distances* appears for the first time in [92] to denote the distances based on morphological dilation and erosion. Although the capability of morphological distances to deal with the geometry of shapes is demonstrated in several papers [90, 92, 103, 126], an overview of existing morphological distances and their properties is missing in the literature.

To express the Hausdorff distance in a way that is widely used to highlight the usage of morphological operations in computing distances between sets points, let us denote with \mathcal{B}_R^c a compact ball in a metric space (D, d) . The Hausdorff distance is frequently referred as the *Hausdorff dilation distance* [103] when computed between compact subsets X and Y of a bounded set:

$$d_H(X, Y) = \inf_{R \in \mathbb{R}} \{R \mid X \oplus \mathcal{B}_R^c \supseteq Y \text{ and } X \subseteq Y \oplus \mathcal{B}_R^c\}. \quad (2.36)$$

If X, Y are, also, regular, i.e. $cl(int(X)) = X$ and $cl(int(Y)) = Y$, where $cl(X)$ denotes closure and $int(X)$ interior of a set X , the Hausdorff distance can be expressed as the *Hausdorff erosion distance* [103]:

$$d_H(X, Y) = \inf_{R \in \mathbb{R}} \{R \mid X \ominus \mathcal{B}_R^c \subseteq Y \text{ and } X \supseteq Y \ominus \mathcal{B}_R^c\}. \quad (2.37)$$

Since they are based on an isotropic structuring element, i.e. a ball, Hausdorff dilation and Hausdorff erosion distances do not provide a great possibility to be adjusted to a specific shape property. Following the idea of Hausdorff dilation distance, its modified definition that allows a structuring element of an arbitrary shape to be used is proposed in [93]. Modified definition is given by the following equation and the introduced distance is named *dilation distance* for sets:

$$d_D(X, Y) = \min_{n \in \mathbb{N}} \{n \mid X \subseteq (Y \oplus nO)\}, \quad (2.38)$$

where $Y \oplus nO$ denotes subsequently performed morphological dilation of a set Y : $Y \oplus nO = (((Y \oplus O) \oplus O) \dots \oplus O)$ by a flat structuring element O . We emphasize that

d_D and d_H are not the same. For instance, if $X \subset Y$ then $d_D(X, Y) \neq d_D(Y, X)$, while d_H is symmetric.

The important point to note is that d_D can be adjusted to certain types of shape changes by choosing an appropriate structuring element. Such changes of the square S_1 with side q presented in Figure 2.15(a) are given in Figure 2.15(b) and Figure 2.15(c), where horizontal and vertical segments of the same size are added to S_1 to obtain S_2 and S_3 , respectively. If we choose the structuring element presented in Figure 2.15(d), $d_D(S_1, S_2) = 1$ and $d_D(S_1, S_3) = 3$. By choosing a structuring element oriented horizontally, we adjusted dilation distance to be more sensitive to the shape changes oriented vertically.

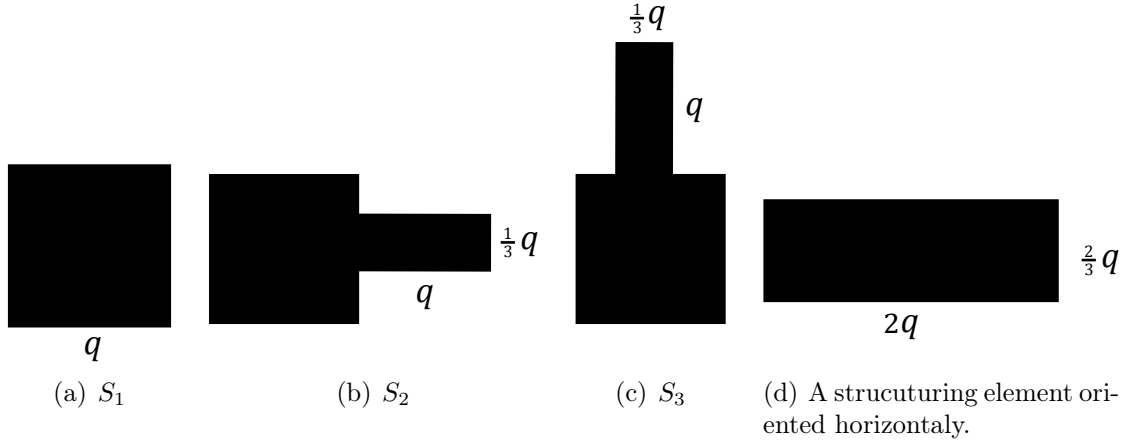


Figure 2.15: By choosing the structuring element oriented horizontally from (d), we adjusted d_D to be more sensitive to shape changes oriented vertically. For the given structuring element $d_D(S_1, S_2) = 1$, while $d_D(S_1, S_3) = 3$.

Although having greater capability to be adjusted to shape changes than d_H , d_D still strongly depends on the furthest point from the border, which is frequently an outlier. To compute distances between gray scale images the concept given by Equation 2.38 is straightforwardly extended using gray scale dilation and erosion [92]:

Definition 2.5.2. For a function pair $f_1, f_2 : D \rightarrow \mathbb{R}$, the dilation and the erosion distance based on subsequently performed dilation and erosion are respectively given by:

$$d_{dilate}(f_1, f_2) = \min\{n \mid A((f_1 \wedge f_2) \oplus nO) > A(f_1 \vee f_2)\} \quad (2.39)$$

$$d_{erode}(f_1, f_2) = \min\{n \mid A((f_1 \vee f_2) \ominus nO) < A(f_1 \wedge f_2)\} \quad (2.40)$$

where $(f_1 \wedge f_2)(x) = \inf(f_1(x), f_2(x))$, $(f_1 \vee f_2)(x) = \sup(f_1(x), f_2(x))$ and $A(f) = \int_{x \in D} f(x) dx$.

Being based on sums, d_{dilate} and d_{erode} are not sensitive to outliers as d_H and d_D . At the same time their discriminative power between shape changes is decreased. For instance, d_{dilate} would be the same when the binary image representation of the shape from Figure 2.15(a) is compared with binary image representations of shapes from Figure 2.15(b) and Figure 2.15(c).

Chapter 3

Feret's Diameter

Overview This chapter is based on papers "Precise estimation of the projection of a shape from a pixel coverage representation" [27] and "Estimation of Feret's Diameter from pixel coverage representation of a shape" [28]. Section 3.1 briefly describes the importance of Feret's diameter. In Section 3.2 we give a description of the estimation of Feret's diameter from digital images in a traditional manner. In Section 3.2.1 we give an overview of problems related to estimation in this manner and in Section 3.2.2 error analysis and multigrid convergence. In Section 3.3 we present a new method for estimation of Feret's diameter from digital images that utilizes pixel coverage representation of a shape proposed in [27]. We give error analysis with multigrid convergence of this method in Section 3.3.1 and Section 3.3.2 and improvement based on this analysis in Section 3.3.3. In Section 3.4 we compare performance of methods in synthetic and real examples.

3.1 Importance of Feret's diameter

The usage of Feret's diameter in real applications is extremely high since it can be relatively easily measured in practice and provides a measure of such a basic property of an object as the size. In sequel, we give an overview of some of work in order to show that Feret's diameter has a strong discriminating power between objects worth further exploration and to illustrate significance of Feret's diameter in applications in which is of great importance that a used measure is as exact as possible.

The classic diameter, which can be computed from Feret's using Equation 2.4, is a basic and simple shape property standardly used as shape descriptor. Nevertheless, it continues to be an active subject of research in shape analysis. For comparing objects based on their shapes, the ratio of the squared distance between two shape centroids (one computed from the whole shape and other computed from

shape border) to the squared shape diameter is studied in [57]. In [128] is proven that the circles have the minimal diameter among all the shapes having the same area. Based on this, two measures, that reach their minima for disks, for shape elongation are defined via shape diameter. The classical diameter is widely used in real applications in which poor estimation can have critical consequences. For example, obtaining exact vessel diameters during coronary interventions is essential for sizing interventional devices such as angioplasty balloons and stents. Due to this, extensive studies are conducted to evaluate and compare errors of widely used image analysis systems for estimation of vessels diameter [51, 70, 115, 123]. The classic diameter of a tumor is the fundamental prognostic factor of the outcome of a medical treatment. A factor that suggest poor prognosis for the treatment from [37] is tumor diameter above 10 *cm*. In [131] is concluded that tumor diameter is related to lymph node metastases.

Feret's diameter provides a more comprehensive shape information than classic diameter as it gives a measure of object size along one or more selected directions. It is standardly used for shape description when objects of interest are very small which makes discerning between objects based on their size a delicate problem. Consequently, precision and accuracy of measuring Feret's diameter are of great importance. As a measure of size of of very small objects, Feret's diameter is used even before emergence of digital image processing. For instance, it is used to describe size of microscopic particles as seen in profile under the microscope in [130]. After the appearance of digital image processing, Feret's diameter stayed irreplaceable descriptor for analysis of size of particles from their digital image representation. An automated system based on Feret's diameter calculated from binary images for classification of spores is presented in [129]. In [48] Feret's diameter computed from binary images is used for estimation of length and width of dust particles. In [35] Feret's diameter for multiple directions is computed from binary images to compare cells of yeasts. More particularly, maximal and minimal Feret's diameter as well as elongation computed in accordance with Equation 2.5 are used for this purpose.

3.2 Estimation from Binary Images

Binary image representation of a shape usually corresponds to the Gauss digitization of that shape. When estimated in real applications, Feret's diameter $\mathcal{F}_\varphi(S)$ of a compact set $S \subset \mathbb{R}^2$ is estimated from binary images in accordance with Definition 2.1.2 as $\mathcal{F}_\varphi(\mathcal{G}_i(S))$, $i \in \{1, 2\}$ [48, 129]. We refer to these approaches, respectively, as *Binary Approach 1* (BAP1), based on \mathcal{G}_1 , and *Binary Approach 2* (BAP2), based on \mathcal{G}_2 . Also, in theoretical considerations of the upper bound error for shape analysis methods the Gauss digitization is used to represent digital

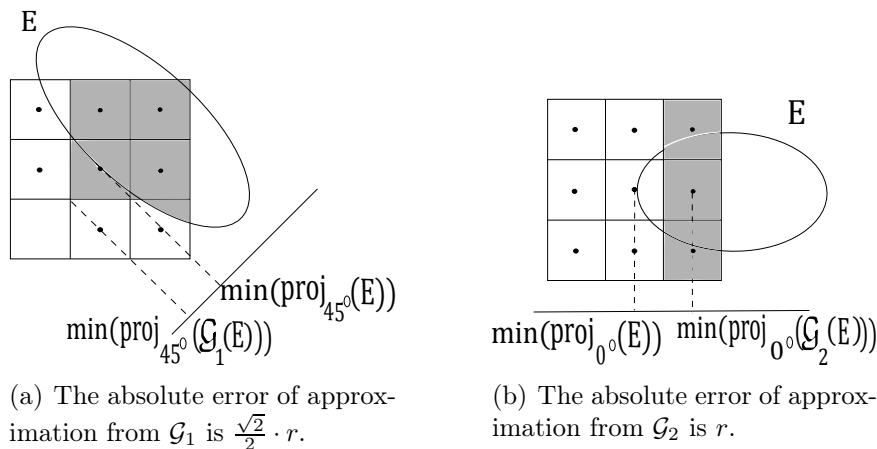


Figure 3.1: An ellipse E in the digital grid with pixel size r and the error of estimating $\min(\text{proj}_\varphi(\mathcal{G}_i(E)))$, $i \in \{1, 2\}$.

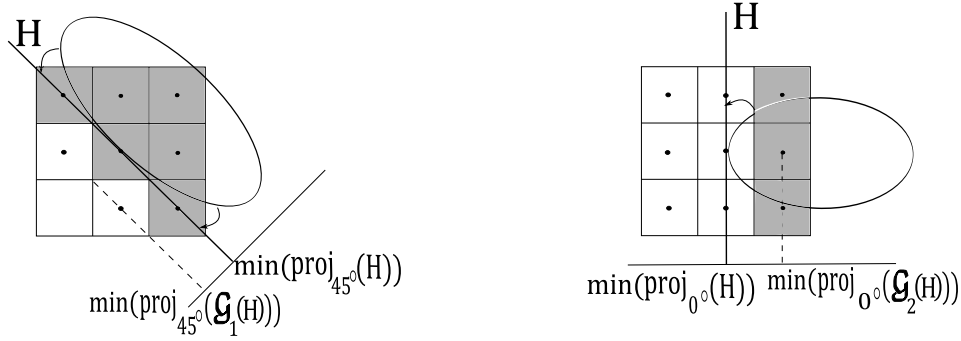
approximation of a two dimensional shape [17, 46, 56, 58, 112]. Both variants of Gauss digitization are present in the literature. \mathcal{G}_1 is, e.g., used in [31, 33] and \mathcal{G}_2 is used, e.g., in [14, 15].

3.2.1 Examples and Motivation for Improvement

To illustrate the need for the improvement of accuracy and precision of estimation of Feret's diameter from Gauss digitization, we refer to Figure 3.1. In the figure is given $\min(\text{proj}_\varphi(\mathcal{G}_i(E)))$, $i \in \{1, 2\}$, for a position of an ellipse E in the digital grid with pixel size r . Whenever \mathcal{G}_1 is used, extremal point is approximated by a vertex of a pixel in the grid as illustrated in Figure 3.1(a). For given example the absolute error of approximation amounts $\frac{\sqrt{2}}{2} \cdot r$. Similarly, whenever $\mathcal{G}_2(E)$ is used, extremal point of an ellipse E is approximated by the center of a pixel. For such approximation the absolute error of approximation amounts r in a given example.

Regardless of the used variant of digitization, the estimation of Feret's diameter will be accurate only if there exists a position of E in the digital grid for which both extremal points in a given direction coincidence with its approximations. In most of the cases such position does not exist. A change of the position of E in the digital grid can change the error of approximation of extremal points and therefore the error of estimation of Feret's diameter. Due to this, the estimation is not precise. All the consideration applies on an arbitrary shape.

In many real applications the mentioned error has a large negative impact on performance. For instance, in [129] is shown that the automated method based on



(a) If $\min(\text{proj}_\varphi(H))$ is estimated from $\mathcal{G}_1(H)$, maximal error of estimation is reached for $\varphi = 45^\circ$ and is $\frac{\sqrt{2}}{2} \cdot r$.

(b) If $\min(\text{proj}_\varphi(H))$ is estimated from $\mathcal{G}_2(H)$, maximal error of estimation is reached for $\varphi = 0^\circ$ and is r .

Figure 3.2: Position of a half plane H in the digital grid for which $\max_\varphi |\Delta \min(\text{proj}_\varphi(H))|$ is reached for BAP1 and BAP2.

Feret's diameter estimation from binary images is faster than the manual classification of spores. Yet, authors notice that the method shows increasing misclassification when a larger amount of particles other than spores are present due to imprecise evaluation of particle measurements. The method based on computing Feret's diameter from binary images from [48] shows high accuracy, speed and reproducibility. The drawback is that for finer particles, increasing of resolution and specialized computing resources are needed.

3.2.2 Error analysis and multigrid convergence

For further consideration we denote the error of estimation of $\min(\text{proj}_\varphi(S))$, for a shape S , as:

$$\Delta \min(\text{proj}_\varphi(S))^{\text{method}} = \min(\widetilde{\text{proj}}_\varphi(S)) - \min(\text{proj}_\varphi(S)), \quad (3.1)$$

where $\text{method} \in \{\text{BAP1}, \text{BAP2}\}$ and by $\min(\widetilde{\text{proj}}_\varphi(S))$ is denoted the estimation of $\min(\text{proj}_\varphi(S))$ by that method.

Consider an arbitrary R -regular shape S , inscribed in a digital grid with grid resolution ν (pixel size r). We observe the estimation of $\min(\text{proj}_\varphi(S))$ by BAP1 and BAP2. W.l.o.g., we assume that $\varphi \in [0^\circ, 45^\circ]$. For simplicity we assume that the curvature of ∂S close to the extremal point is $\kappa = 0$, such that the boundary resembles the straight edge of a half plane H (perpendicular to the direction φ). It is then fairly straightforward to derive the error bounds. This is the best case situation; for shapes where the extremal point is on a curved boundary the errors are equal or larger than the ones we observe here.

As presented in Figure 3.2(a), the minimal value of $\Delta \min(\text{proj}_\varphi(H))^{BAP1}$ is reached for $\varphi = 45^\circ$, when the diagonal of pixel centres are on the boundary of the object:

$$\min_{\varphi} \{ \Delta \min(\text{proj}_\varphi(H))^{BAP1} \} = -\frac{\sqrt{2}}{2} \cdot r. \quad (3.2)$$

The least upper bound of $\Delta \min(\text{proj}_\varphi(H))^{BAP1}$ is approached for $\varphi = 0^\circ$, when pixel centres are on the boundary of the complement. (This is similar to the case shown in Figure 3.2(b).)

$$\sup_{\varphi} \{ \Delta \min(\text{proj}_\varphi(H))^{BAP1} \} = \frac{1}{2} \cdot r. \quad (3.3)$$

Result 1. The error of BAP1 for a straight boundary is always in the interval $[-\frac{\sqrt{2}}{2} \cdot r, \frac{1}{2} \cdot r)$.

As presented in Figure 3.2(b), the supremum of $\Delta \min(\text{proj}_\varphi(H))^{BAP2}$ is approached for $\varphi = 0^\circ$ and amounts:

$$\sup_{\varphi} \{ \Delta \min(\text{proj}_\varphi(H))^{BAP2} \} = r. \quad (3.4)$$

Result 2. The error of estimation by BAP2 for a straight boundary is never negative since $\mathcal{G}_2(H) \subset H$. This implies that the error of BAP2 is always in the interval $[0, r)$.

We briefly mention that it is easy to verify that the upper bounds of \mathcal{G}_1 and \mathcal{G}_2 can be reached if Jordan outer digitization, \mathcal{J}_1 , or Jordan inner digitization, \mathcal{J}_2 , were examined. To illustrate this situation, we give Figure 3.3 where the error $\frac{\sqrt{2}}{2} \cdot r$ is doubled by \mathcal{J}_1 and the error r is reached by \mathcal{J}_2 . Due to this, and the fact that it is used in most theoretical investigations and real applications, we consider only the Gauss digitization in our studies.

Multigrid convergence

For an R -regular shape S in the digital grid, increment of the resolution corresponds to increment of R , with the same rate. Consequently, $\nu \rightarrow \infty$ produces that the curvature $\kappa = \frac{1}{R}$ of ∂S tends to zero, i.e., ∂S tends (locally) to a straight line, at an arbitrary point of ∂S . Since, for both BAP1 and BAP2, the maximal error is proportional to the size of a pixel, the error of these methods approaches zero as $\nu \rightarrow \infty$ with the same speed. Consequently, the estimation of $\mathcal{F}_\varphi(S)$ from $\mathcal{G}_i(S)$, $i \in \{1, 2\}$ is multigrid convergent for all R -regular shapes, with a rate of convergence of $\mathcal{O}(\frac{1}{\nu})$. Still, the large maximal absolute error of BAP1 and BAP2 at lower resolutions is a serious limitation.

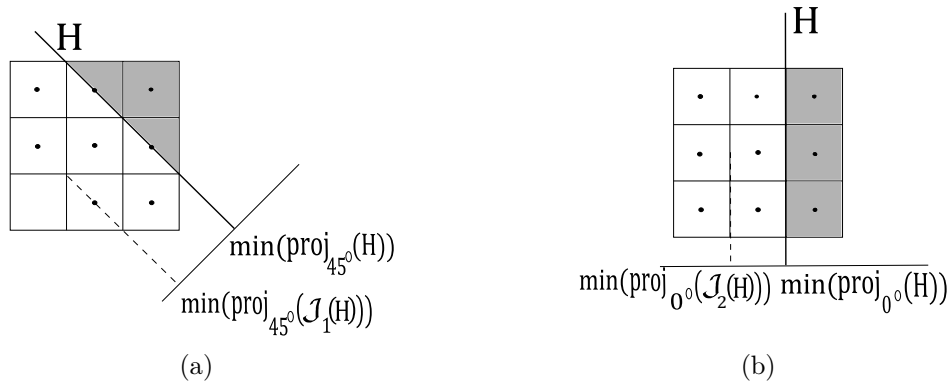


Figure 3.3: The error $\frac{\sqrt{2}}{2} \cdot r$ of $\mathcal{G}_1(H)$ is doubled by \mathcal{J}_2 in a) and the error r of $\mathcal{G}_2(H)$ is reached by \mathcal{J}_2

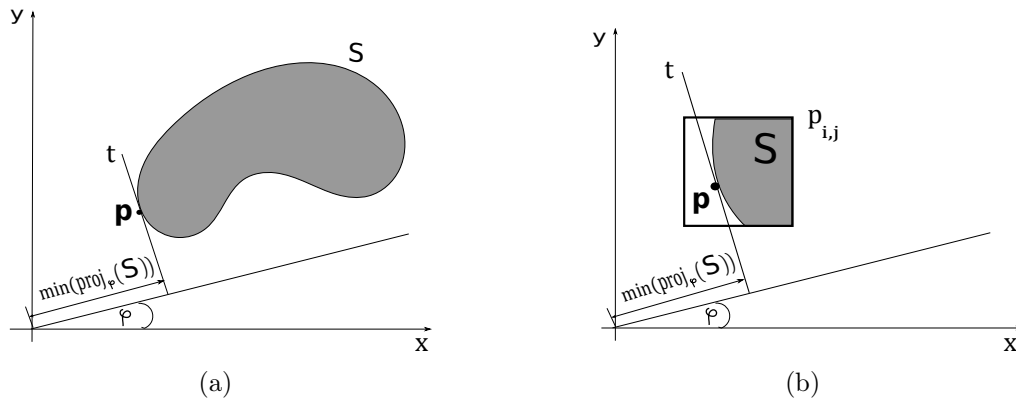


Figure 3.4: (a) Tangent line t at extremal point P that determines $\min(\text{proj}_\varphi(S))$ is perpendicular to the direction φ . (b) t locally approximates ∂S in pixel $p_{i,j}$.

3.3 Estimation from Pixel Coverage Representation

For a given shape S , an extremal point \mathbf{p} in a direction φ lies on the border ∂S . Let us assume that ∂S is smooth such that its tangent line is well defined everywhere. The tangent line t of S at \mathbf{p} is perpendicular to the direction φ and its distance to the origin uniquely determines $\min(\text{proj}_\varphi(S))$ or $\max(\text{proj}_\varphi(S))$. The illustration for $\min(\text{proj}_\varphi(S))$ is given in Figure 3.4(a). Also, t locally approximates ∂S in a pixel $p_{i,j}$ as illustrated in Figure 3.4(b). We consider the estimation of $\min(\text{proj}_\varphi(S))$ in sequel. The estimation of $\max(\text{proj}_\varphi(S))$ is analogous.

Knowing the direction of t and the coverage $\alpha_{i,j}$ of a pixel $p_{i,j}$ by the set S ,

we estimate the distribution of $\alpha_{i,j}$ as follows: within $p_{i,j}$ we approximate the boundary of S with a straight line l which is orthogonal to the direction φ and encloses, together with the pixels edges, a polygon with area equal to the coverage of the pixel. As presented in Figure 3.5, three types of polygons may occur: triangle, trapeze or pentagon. For every case, minimal extremal projection value:

$$\min(\text{proj}_\varphi(S)) = \min_{(x,y) \in S} (x \cos \varphi + y \sin \varphi), \quad (3.5)$$

is computed as the signed distance d , from the centre of the pixel $p_{i,j}$ to the straight line l , added as an offset to the projection of the pixel centre. The computation of d , corresponding to the computation of a minimal extremal projection value from Section III in [27], is as follows:

- $l \cap p_{i,j}$ is a triangle. This is equivalent with $0 < \alpha_{i,j} < \frac{\tan \varphi}{2}$.

If we set the origin in the lower left vertex of $p_{i,j}$ as illustrated in Figure 3.5(a), the length of the projection of the upper left vertex of $p_{i,j}$ onto the direction φ is given by $\cos \varphi + \sin \varphi$. Height h of the $\triangle \mathbf{abc}$ can be calculated as $\sqrt{\sin 2\varphi \cdot \alpha_{i,j}}$. Consequently, $d = \frac{\cos \varphi + \sin \varphi}{2} - \sqrt{\sin 2\varphi \cdot \alpha_{i,j}}$.

- $l \cap p_{i,j}$ is a trapeze. This is equivalent with $\frac{\tan \varphi}{2} \leq \alpha_{i,j} \leq \frac{1 - \tan \varphi}{2}$.

Let us observe parallelogram \mathbf{abcd} illustrated in Figure 3.5(a) which builds l and a line l_1 parallel with l that passes through the pixel center. The area of \mathbf{abcd} is given by $A(\mathbf{abcd}) = \mathbf{ad} \cdot d = \frac{1}{\cos \varphi} \cdot d$. The area of the trapeze that l_1 builds with pixel edges is equal $\frac{1}{2}$. This implies $d = \frac{1}{\cos \varphi}(\frac{1}{2} - \alpha_{i,j})$. We emphasize that $(\frac{1}{2} - \alpha_{i,j}) < 0$ whenever $\alpha_{i,j} > \frac{1}{2}$ providing negative value of d .

- $l \cap p_{i,j}$ is a pentagon. This is equivalent with $\alpha_{i,j} > 1 - \frac{\tan \varphi}{2}$. This case is analogous to the case of triangle since $1 - \alpha_{i,j}$ is a triangle.

For the computation of Feret's diameter only extremal points are relevant. The algorithm from [27] treats each pixel of $\mathcal{D}(S)$ as if it contains an extremal point, and estimates the projection of that point. In case that the pixel does not contain an extremal point, the assumption about the tangent direction may be completely wrong. However, this will only lead to an overestimate of the projection value. Since we look for the minimal projection, such overestimates are not disturbing the algorithm; for the pixel with the minimal projection value, the assumption about the tangent direction is appropriate.

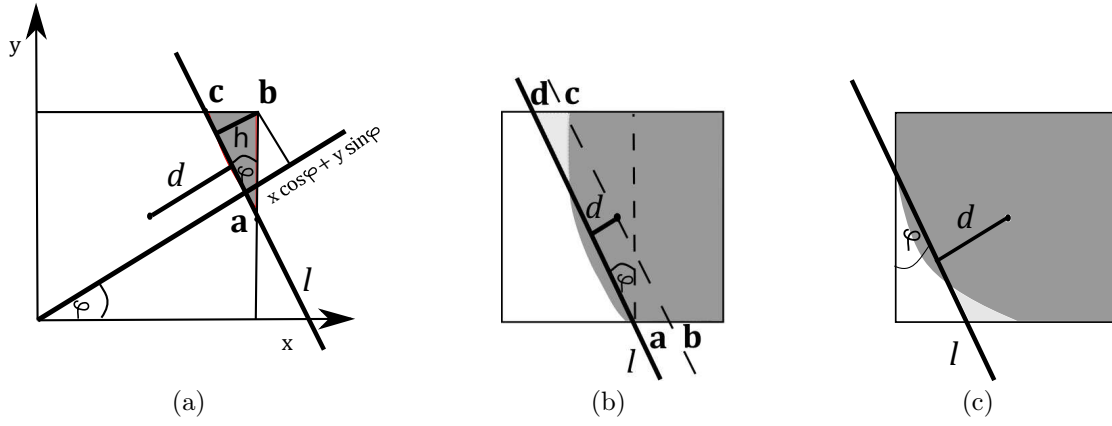


Figure 3.5: The polygon, formed by the line l and the pixel edges, having an area equal to the pixel coverage by the shape (dark gray shaded area), can be: (a) triangle; (b) trapeze; (c) pentagon. The line l is perpendicular to the direction φ . The area of pixel coverage outside the polygon is equal to the area inside the polygon not covered by the shape (light gray shaded area). The signed distance d , from the pixel center to the line l , is negative if the pixel center is covered by the shape and positive otherwise.

Algorithm 1. [27] *Minimal value of $\text{proj}_\varphi(S)$ for a given shape S and the direction φ .*

Input: Pixels $p_{i,j}$, $i \in \{1, \dots, m\}$, $j \in \{1, \dots, n\}$, with pixel coverage values $\alpha_{i,j}$ of given shape S , and direction φ for projecting.

Output: Estimation $\min(\widetilde{\text{proj}}_\varphi(S))$ of $\min(\text{proj}_\varphi(S))$.

for $i \in \{1, \dots, m\}$, $j \in \{1, \dots, n\}$, $\alpha_{i,j} > 0$

if $0 < \alpha_{i,j} < \frac{\tan \varphi}{2}$ (triangle)
 $d = \frac{\cos \varphi + \sin \varphi}{2} - \sqrt{\sin 2\varphi \cdot \alpha_{i,j}}$

elseif $\frac{\tan \varphi}{2} \leq \alpha_{i,j} \leq \frac{1 - \tan \varphi}{2}$ (trapeze)
 $d = \frac{1}{\cos \varphi} (\frac{1}{2} - \alpha_{i,j})$

else /* i.e., $\alpha_{i,j} > 1 - \frac{\tan \varphi}{2}$ */ (pentagon)
 $d = \sqrt{\sin 2\varphi (1 - \alpha_{i,j})} - \frac{\cos \varphi + \sin \varphi}{2}$

end if

$pr_{i,j}(S) = i \cos \varphi + j \sin \varphi + d$

end for

$\min(\widetilde{\text{proj}}_\varphi(S)) = \min \{ pr_{i,j}(S) \mid i \in \{1, \dots, m\}, j \in \{1, \dots, n\}, \alpha_{i,j} > 0 \}$.

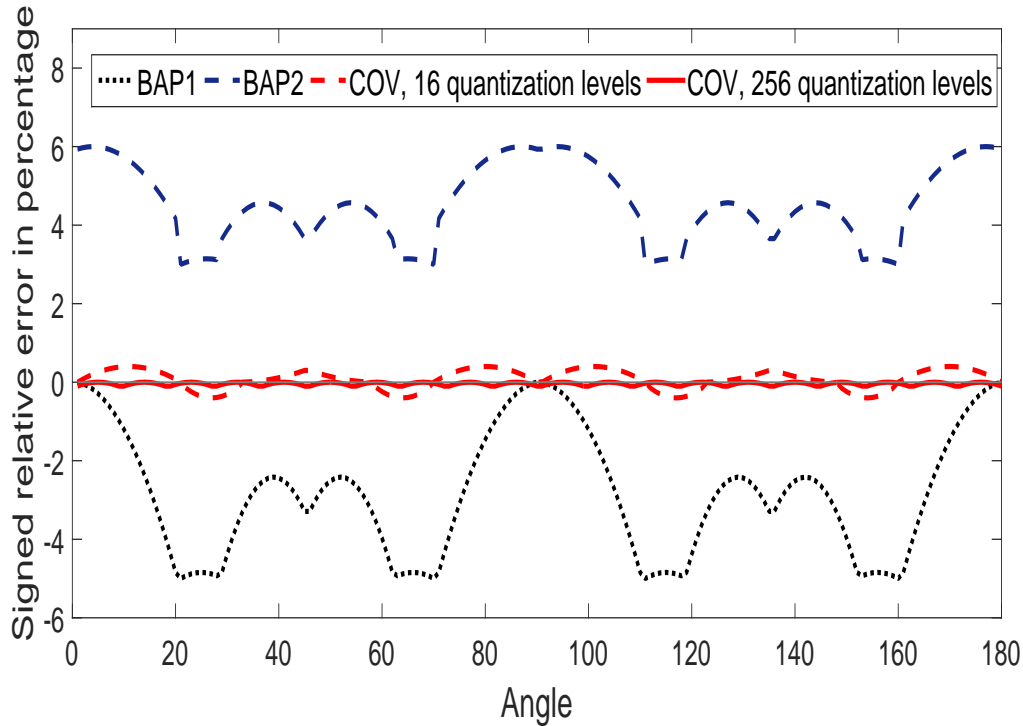


Figure 3.6: Example of signed relative error of Feret's diameter of a circle with radius 8 depending on the angle of projection.

In the sequel, we refer to estimation of $\min(\text{proj}_\varphi(S))$ from $\mathcal{D}(S)$, for a shape S , by Algorithm 1, as *Coverage Approach* (COV).

To present the performance of estimation of Feret's diameter $\tilde{\mathcal{F}}$ by the algorithm, we synthetically generate coverage digitizations of a circle with radius 8 pixels. To estimate pixel coverage values, we divide a pixel into 1×1 , 2×2 , 4×4 , 8×8 and 16×16 subpixels and count the number of subpixels centers contained in the shape. In this way 1, 4, 16, 64 or 256 grey levels become available for representation of pixel coverage by the shape.

Empirical signed relative error $\epsilon = \frac{\tilde{\mathcal{F}}_\varphi(S) - \mathcal{F}_\varphi(S)}{\mathcal{F}_\varphi(S)}$ of estimation of the Feret's diameter by the different algorithms is given in Figure 3.6. The absolute relative error reaches 6% for classical approaches (BAP1 and BAP2) and about 0.1% for 256 quantization levels for the new method (COV).

To present the performance of Feret's diameter by Algorithm 1 when computing other descriptors, we calculate elongation as $\tilde{\mathcal{E}} = \max_{\varphi \in [0, \pi]} \frac{\tilde{\mathcal{F}}_\varphi(S)}{\tilde{\mathcal{F}}_{\varphi + \frac{\pi}{2}}(S)}$. To present

improved accuracy and precision by the algorithm comparing to estimation from binary images, we perform test on a group of 900 ellipses with different positions in the digital grid and different sizes. For every ellipse, the positions of foci are randomly chosen inside one pixel and every 5 randomly positioned foci are rotated with step of 5 degrees in range $[0^\circ, 90^\circ]$. We increase major axis, but keep distance, d , between two foci. Because minor axis can be expressed as: $b = \sqrt{a^2 - (d/2)^2}$, an assumption of fixed value d implies that minor and major axes increase and decrease together. Estimation of elongation consequently, may exhibit behaviour less dependent on resolution changes. The obtained results are presented in Figure 3.7. For elongation, the signed relative error is approximately reduced from 16.36 to 0.05% when changing from BAP1 to COV.

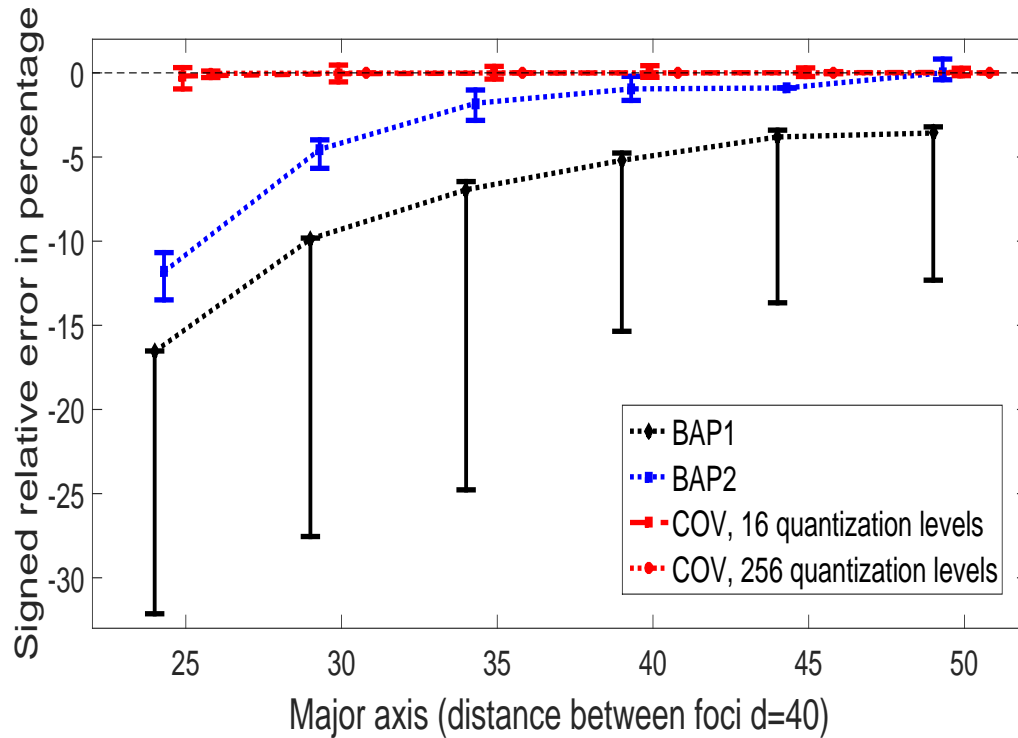


Figure 3.7: Signed relative error of estimation of elongation of an ellipse using different methods.

Although the assumption on smooth border is made, the algorithm can be used for shapes with non smooth border, e.g. polygons. As extremal point of polygonal shape is always a vertex, the error will strongly depend on the interior angle of the vertex, as it is presented in Figure 3.8.

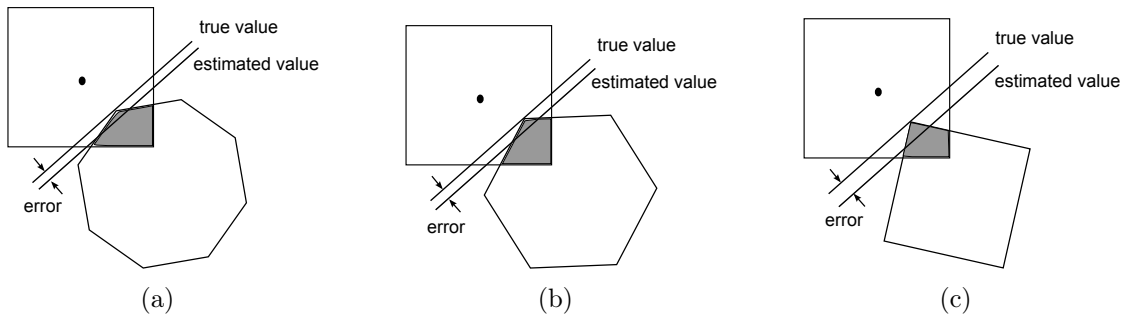


Figure 3.8: Error of approximation for polygonal shapes depends on interior angle of vertex.

To demonstrate the applicability of the algorithm on polygonal shapes we observe estimation of the diameter of a square for different side length. The results are given in Figure 3.9. We note that the violation of the smoothness requirement does degrade the performance of the method. However, it still significantly outperforms the best of the two methods based on binary images.

3.3.1 Lower and upper error bounds of Algorithm 1

Following notions from 3.1, we denote the error of estimation of $\min(\text{proj}_\varphi(S))$ by COV as $\Delta \min(\text{proj}_\varphi(S))^{COV}$. To be able to study $\Delta \min(\text{proj}_\varphi(S))^{COV}$ and theoretical properties of COV regardless of the error of estimation of coverage values, we assume exact pixel coverage values. As demonstrated in experiments presented in Figure 3.6, Figure 3.7 and Figure 3.9, the method works well for approximate coverage values.

From experiment presented in Figure 3.6 we conclude that COV is more precise than BAP1 or BAP2. In this experiment, the absolute relative error of estimation of the diameter of a disk is reduced 50 times by COV, compared to binary approaches. However, the output of Algorithm 1 does not give the correct value on average, i.e. it is not accurate because it has a certain bias.

Following theorems and analysis enable further improvement of COV by further reducing its maximal absolute error.

Proposition 3.3.1. *For an arbitrary shape S and a direction φ , it holds that:*

$$\Delta \min(\text{proj}_\varphi(S))^{COV} \geq 0. \quad (3.6)$$

Proof. It is easy to conclude that for any pixel with a coverage value $\alpha_{i,j} > 0$, the estimate $pr_{i,j}$ computed by Algorithm 1 is the upper bound of possible projection values for any distribution of the same area within the pixel $p_{i,j}$. The assumed

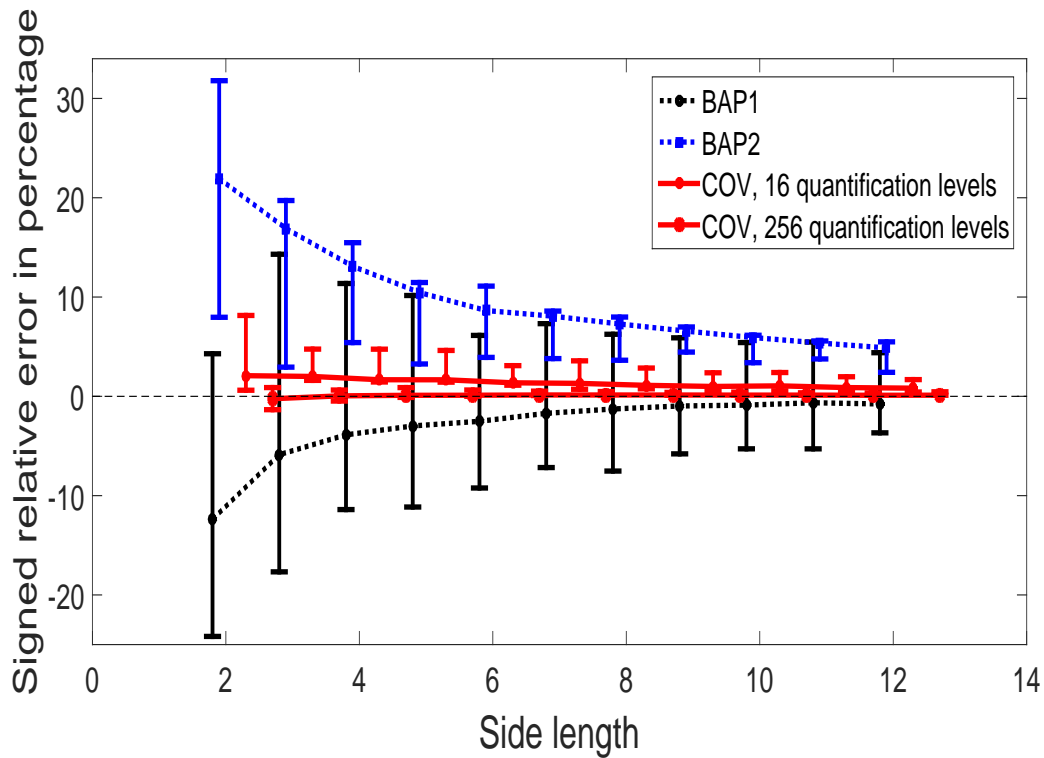


Figure 3.9: Signed relative error of estimation for diameter of a square using different methods.

distribution of area ensures the largest possible projection value given the covered area. ■

It is straightforward to conclude that the lower bound $\Delta \min(\text{proj}_\varphi(S))^{COV} = 0$ is reached by any shape with a straight boundary perpendicular to the direction φ which extends through a pixel. For this case, the polygonal approximation of Algorithm 1 is exact.

To formally discuss convergence of $\partial S \cap p_{i,j}$ toward $l \cap p_{i,j}$, we restrict the analysis to R -regular shapes in a digital grid where R is greater than the pixel diameter r . The condition $r < R$ ensures that the $\partial S \cap p_{i,j}$ can be polygonalized in a reasonable way in the sense of Figure 3.5. An example of violation of this condition is shown in Figure 3.10(a). For an extremal point, it holds by definition that the shape boundary is situated between the inner osculating disk \mathcal{K} and the tangent line in the point (see Figure 3.10(b)).

Proposition 3.3.2. *For an arbitrary angle φ , the upper bound of $\Delta \min(\text{proj}_\varphi(S))^{COV}$, over all coverage digitizations of R -regular shapes S , in a grid where R is greater than the pixel diameter, is reached for a coverage digitization of a disk with radius*

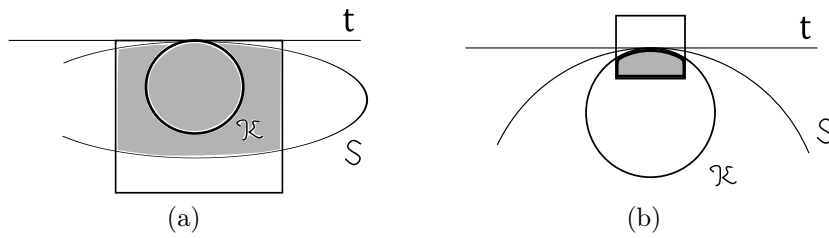


Figure 3.10: (a) If the radius of the osculating disk is smaller than the diameter of a pixel p , then two “independent parts“ of ∂S may intersect p . (b) At an extremal point, the boundary of an R -regular shape S is situated between the inner osculating disk \mathcal{K} and the tangent line t .

R .

Proof. At an extremal point of a shape S , we can, according to Definition 2.2.3, always fit an osculating disk \mathcal{K} of radius R inside S . Since $\mathcal{K} \cap p_{i,j} \subseteq S \cap p_{i,j}$ and the projection value $pr_{i,j}$ of any pixel $p_{i,j}$ in Algorithm 1 is monotonically non-increasing w.r.t $\alpha_{i,j}$, it follows that $pr_{i,j}(\mathcal{K}) \geq pr_{i,j}(S)$. ■

Besides providing us a shape for which analytic equation is known that limits from above $\Delta \min(\text{proj}_\varphi(S))^{COV}$, proposition 3.3.2 enables an analysis of multigrad convergence of COV:

Increment of the grid resolution ν is equivalent to increment of the radius R . As $\nu \rightarrow \infty$, the upper bound of the error, according to Proposition 3.3.2, approaches the projection error for a disk with infinite radius, i.e., the error for a (locally) straight boundary. Since Algorithm 1 provides a correct, error free result for such a boundary, it is clear from Proposition 3.3.1 and Proposition 3.3.2 that $\Delta \min(\text{proj}_\varphi(S))^{COV}$ converges toward 0, as $\nu \rightarrow \infty$.

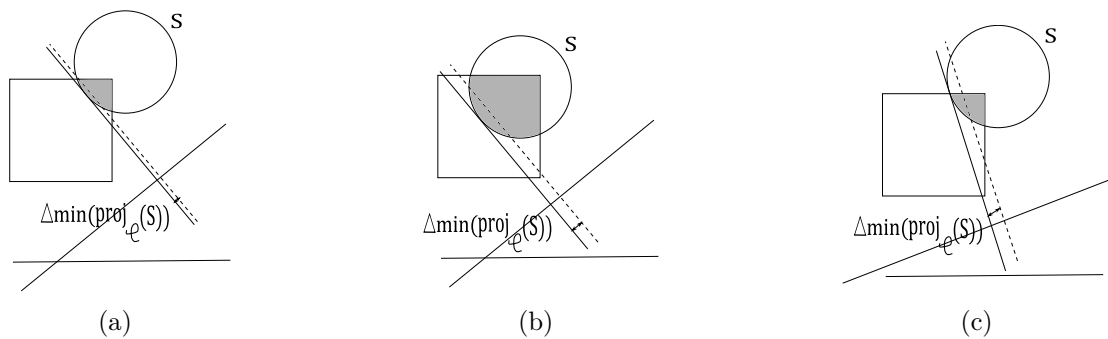


Figure 3.11: The projection estimation error changes depending on the direction φ and the position of a shape in the digital grid.

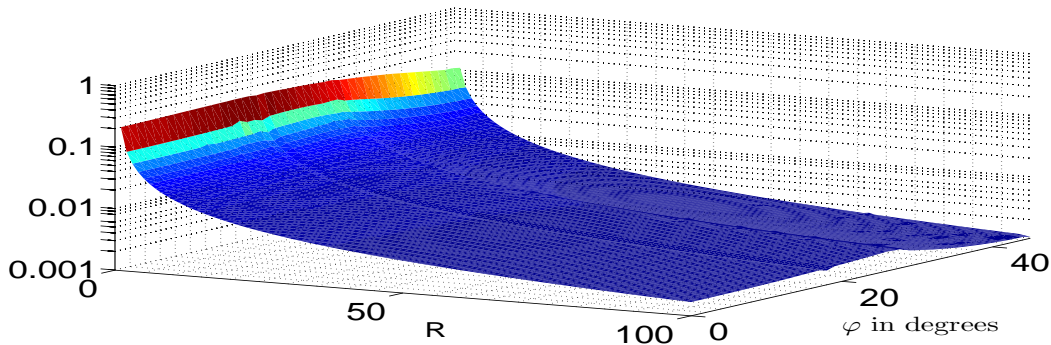


Figure 3.12: Maximal error of the estimation of $\min(\text{proj}_\varphi(S))^{COV}$ for a shape S with the maximal boundary curvature $\kappa_{\max} = \frac{1}{R}$, evaluated for $\varphi \in \{0^\circ, 1^\circ, 2^\circ, \dots, 45^\circ\}$ and $R \in \{1, 2, \dots, 100\}$.

3.3.2 Empirical analysis of the error

To minimize the error of Algorithm 1 we seek an explicit expression for the maximal error reached for R -regular objects of a given maximal boundary curvature κ_{\max} and a given direction of projection φ . We note that a change of position of the shape S in the digital grid, or a change of the direction of projecting φ , may lead to a change of $\Delta \min(\text{proj}_\varphi(S))^{COV}$. Some examples are illustrated in Figure 3.11.

Not knowing the exact position of S in the grid, we observe all positions and find an upper bound of the error as a function of the direction φ . From Proposition 3.3.2 we know that the maximal value of $\Delta \min(\text{proj}_\varphi(S))^{COV}$, over all translations and rotations of S in the digital grid, is, for any angle φ , reached for the point with the maximal curvature along ∂S . To estimate the maximal error of COV for a shape with the maximal curvature κ_{\max} , it is therefore enough to observe a disk with radius $R = \frac{1}{\kappa_{\max}}$, and seek for the maximal error over all positions in the digital grid, for each given angle φ .

Neighbouring pixels interact in an intricate way and, despite the simplicity of the studied shape, it turns out to be non-trivial to derive an analytic expression for $\Delta \min(\text{proj}_\varphi(S))^{COV}$.

Instead, we perform in [28] a thorough empirical study of the error for disks of different radii and locations in the digital grid. Due to symmetry of the digital grid, it is enough to observe $\varphi \in [0^\circ, 45^\circ]$. We observe $\varphi \in \{0^\circ, 1^\circ, \dots, 45^\circ\}$ and for every value φ and given R , we evaluate all translations of the centre of the disk inside one pixel in steps of 0.001 pixel, in the directions of x and y axes. The maximal error over this range of data is plotted in Figure 3.12, for every $R \in \{1, 2, 3, \dots, 100\}$.

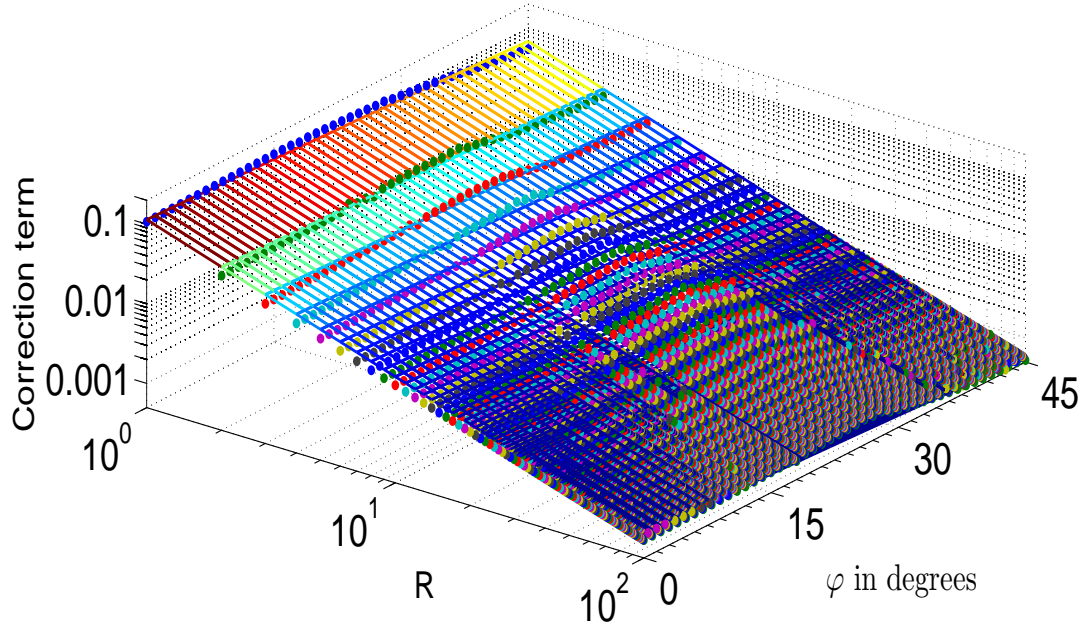


Figure 3.13: Empirical values of correction term for $R \in \{1, 2, \dots, 100\}$ and $\varphi \in \{0^\circ, 1^\circ, \dots, 45^\circ\}$ and the surface $Corr^{fit}$ obtained by fitting procedure. For improved visualization are the radius R and the function value presented with a logarithmic scale.

3.3.3 Improved method for estimation of Feret's diameter

If ∂S is a straight line, COV provides an exact value of the projection. To reduce the error for curved boundaries, we use, for any given φ , the empirical estimate of $\max(\Delta \min(\text{proj}_\varphi(S))^{COV})$, where the maximum is over all positions of S in the digital grid.

The fact that the error of COV is in the range $[0, \max\{\Delta \min(\text{proj}_\varphi(S))^{COV}\}]$ enables us to improve the estimate and to minimize the maximal error by introducing a correction term, to centre the range of errors around zero:

$$\begin{aligned} \min(\widetilde{\text{proj}}_\varphi^{corr}(S)) &= \min(\widetilde{\text{proj}}_\varphi(S)) - Corr(R, \varphi), \\ Corr(R, \varphi) &= \frac{1}{2} \max\{\Delta \min(\text{proj}_\varphi(S))^{COV}\}. \end{aligned} \quad (3.7)$$

By introducing this correction term, we reduce the maximal absolute error of the estimation to at most half of the original one.

To express the correction term $Corr$ used in Equation (3.7), we perform a fitting procedure on the point cloud of data described in the previous section,

where the values of the maximal error are divided by two. The point cloud of empirically obtained values, $Corr^{emp}(R, \varphi)$, shows strong similarity to a power function and asymptotic behaviour as $R \rightarrow \infty$. Therefore, we tried fitting to numerous expressions such as: $a \cdot R^b \cdot \varphi^c$, $\frac{a+b \cdot \varphi^c}{R^d}$, $a \cdot R^b + c \cdot \frac{\varphi}{R}$. When Levenberg-Marquardt algorithm is applied to the non linear least square problem:

$$\min_{a,b,c} \left(\sum_{R,\varphi} (Corr^{emp}(R, \varphi) - (a \cdot R^b + c \cdot (\frac{\varphi}{R}))^2) \right), \quad (3.8)$$

we obtain the following expression for the correction term:

$$Corr^{fit}(R, \varphi') = 0.11142 \cdot R^{-1.02808} - 1.01 \cdot 10^{-3} \cdot \frac{\varphi'}{R}. \quad (3.9)$$

Due to symmetry, it is enough to observe angles $\varphi' \in [0^\circ, 45^\circ]$, $\varphi' = \left| (\varphi + 45) \bmod 90 - 45 \right|$ where mod denotes the modulo operation. In Figure 3.13 we show empirical values of the correction term and the surface obtained by fitting for $R \in \{1, 2, \dots, 100\}$, $\varphi \in \{0^\circ, 1^\circ, \dots, 45^\circ\}$.

The error introduced by fitting is acceptable; average residual is $5.368 \cdot 10^{-4}$, while average value $\Delta \min(\text{proj}_\varphi(S))^{COV}$ over all R and φ is $8.793 \cdot 10^{-3}$. The fit explains the variation of the data to a high degree; the coefficient of determination, R^2 , is $1 - 3.427 \cdot 10^{-5}$.

Based on the above results and observations, we propose an improved method for estimation of Feret's diameter of an R -regular shape S , with the maximal curvature of the boundary κ_{max} , in the direction φ :

1. Compute extremal projections using Algorithm 1.
2. Calculate the correction term $Corr(R, \varphi)$ for $R = \frac{1}{\kappa_{max}}$ and the considered direction φ according to Equation (3.9).
3. Apply Equation (3.7) to obtain an estimate of Feret's diameter with minimal maximal error:

$$\begin{aligned} \tilde{\mathcal{F}}_\varphi^{corr}(S) = \max(\widetilde{\text{proj}}_\varphi(S)) + Corr(R, \varphi) - \\ (\min(\widetilde{\text{proj}}_\varphi(S)) - Corr(R, \varphi)). \end{aligned} \quad (3.10)$$

The estimated upper bound of the maximal absolute error of estimation of Feret's diameter by this method is

$$2 \cdot Corr^{fit}(R, \varphi) = 2 \cdot (0.11142 \cdot R^{-1.02808} - 1.01 \cdot 10^{-3} \cdot \frac{\varphi}{R}). \quad (3.11)$$

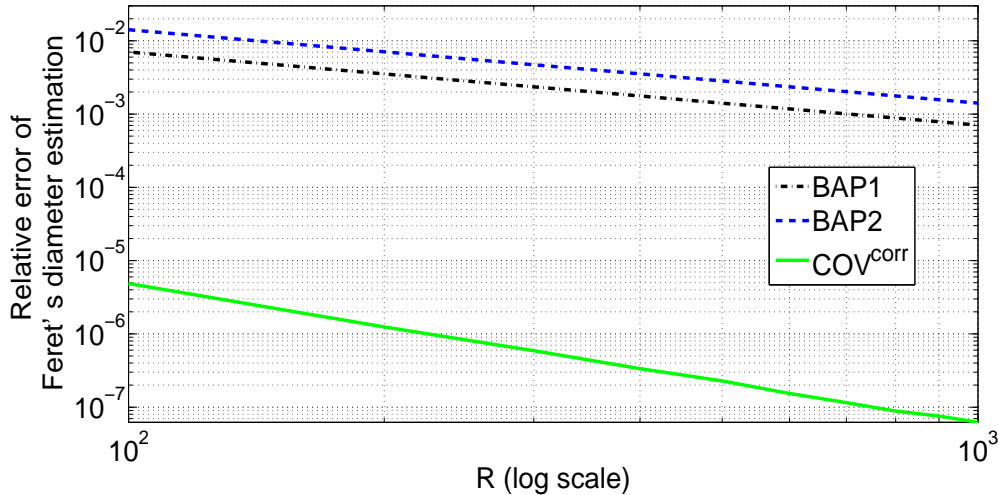


Figure 3.14: Relative error of estimation of Feret’s diameter for disks of increasing radius. The error of the proposed method is reduced by a factor 100 when object size is increased by a factor 10.

Multigrid convergence

From Equation (3.11) we see that the error (measured in pixels) converges toward 0, roughly at a speed $\frac{1}{R}$. If we increase the image resolution by a factor ν , the radius of curvature increases with the same factor and the error measured in pixels decreases as $\approx \frac{1}{\nu}$ while, at the same time, the size of a pixel also decreases as $\frac{1}{\nu}$. From this, as previously noted, we conclude that the proposed method is multigrid convergent for any R -regular set (with $R > r$) with an empirically observed rate of convergence of $\mathcal{O}(\frac{1}{\nu^2})$.

An empirical study, shown in Figure 3.14, where the relative error, $\frac{|\hat{x}-x|}{x}$, of estimation of Feret’s diameter using observed methods is presented for disks of increasing radii supports the observation on speed of convergence. We observe that if the object size is increased by a factor 10, BAP1 and BAP2 show a reduction of relative error by the same factor, whereas for the proposed method the same change leads to a reduction of the relative error by the square of the change in size, i.e., a factor 100.

3.4 Evaluation

In following, we refer to the method of Section 3.3.3 as COV^{corr} . We evaluate COV^{corr} by comparing it with BAP1, BAP2 and COV. For synthetically generated

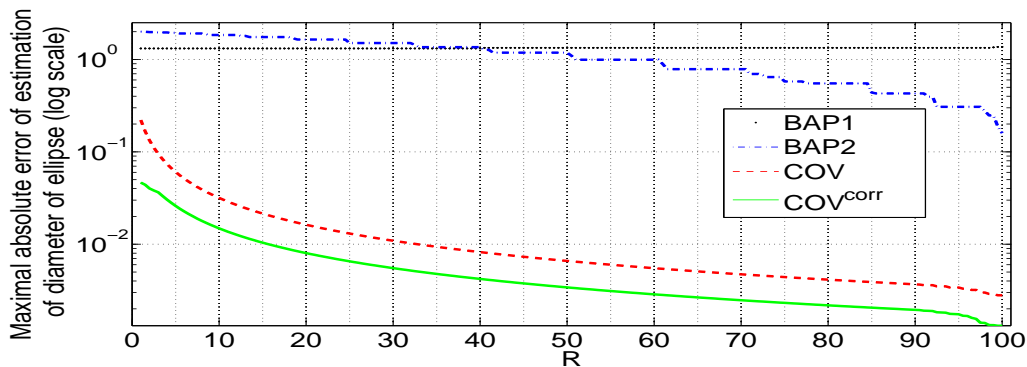


Figure 3.15: Maximal absolute error of estimation of diameter for ellipses of different eccentricity. For each value $R \in \{1, 1.5, 2, 2.5, \dots, 99.5, 100\}$, 200 displacements in the digital grid are observed.

ellipses, we examine the maximal absolute error in estimation of the maximal and average Feret's diameter. In real imaging conditions, we examine the error in estimation of Feret's diameter of ellipses in two perpendicular directions. Also, we examine the rotational invariance of estimation of Feret's diameter for a disk. At the end, we evaluate the performance of COV^{corr} in a real application on a data set of 368 microscopic images of cell nuclei.

In our experiments, we show that COV^{corr} exceeds the performance of other methods. COV^{corr} shows especially good performance at low resolutions where it outperforms other methods, often by a large margin.

3.4.1 Synthetic data

Classic diameter of ellipses

We evaluate performance of COV^{corr} in estimation of the classic diameter on 400000 synthetically generated ellipses. The minimal radius of the curvature R of an ellipse with major and minor axis a and b is given by $\frac{b^2}{a}$. For fixed major axis $a = 100$, we select $R \in \{1, 1.5, 2, \dots, 100\}$ by setting the minor axis $b = \sqrt{R \cdot a}$. For every value R , we rotate the ellipse with an angle of rotation in the range $[0^\circ, 45^\circ]$ with the step 5° . For every rotation, we perform 200 random translations of the centre of the ellipse inside one pixel. Knowing the minimal radius of curvature and the angle φ , we calculate Corr as explained in Section 3.3.3. The obtained maximal absolute error is presented in Figure 3.15.

For BAP1, observed maximal absolute error is in the range $[1.3156, 1.3682]$. For BAP2 the error range is $[0.1595, 2.0000]$. The error of COV^{corr} is $[0.0013, 0.0465]$. On average, the reduction of the error is 210 times compared to BAP1 and 174

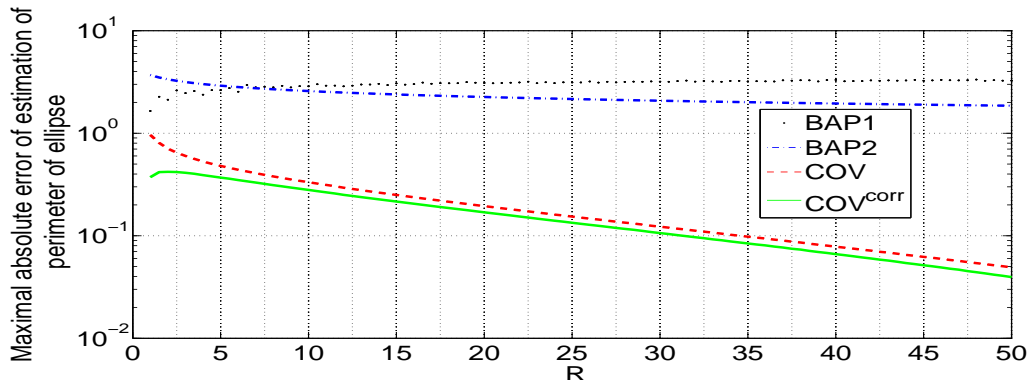


Figure 3.16: Maximal absolute error of estimation of perimeter of ellipse for $R \in \{1, 1.5, 2, \dots, 50\}$ from Cauchy’s theorem.

times compared to BAP2. This is a dramatic improvement in performance. For COV the error is in the range $[0.0028, 0.2211]$ which is, on average, 2.3 times worse performance than COV^{corr} .

Ellipse perimeter via average Feret’s diameter

We evaluate performance of COV^{corr} in estimation of the average Feret’s diameter. We perform tests in the same manner as in the previous section, but exclude rotations from consideration and observe $R \in \{1, 1.5, 2, \dots, 50\}$. For every value R , we perform 1000 random translations of the ellipse centre inside one pixel. For every position in the digital grid, we estimate average Feret’s diameter $\bar{\mathcal{F}}$ over all angles with a step of 1° and use Theorem 2.1.3 to estimate perimeter of the ellipse as $\bar{\mathcal{F}} \cdot \pi$. Knowing the minimal radius of curvature and projecting direction, we calculated Corr as explained in Section 3.3.3. The maximal absolute error over 1000 translations for perimeter estimation is given in Figure 3.16.

Maximal absolute error of the perimeter estimates is in the range $[1.6471, 3.3381]$ for BAP1. It is within $[1.8541, 3.6956]$ for BAP2. The error for COV^{corr} is in the range $[0.0395, 0.4200]$. On average, the reduction of the error is 18.4 times compared to BAP1 and 13.7 times compared to BAP2. For COV, the range of the error is $[0.0491, 0.9632]$. For ellipses with high maximal curvature along the boundary ($R = 1$) the error of COV is 2.3 times larger than the error of COV^{corr} .

3.4.2 Real data

Digital photos of printed disks

To evaluate the method in more realistic conditions we take photos of 5 black disks printed on a white paper. We set the digital camera at resolution 640×480 px in

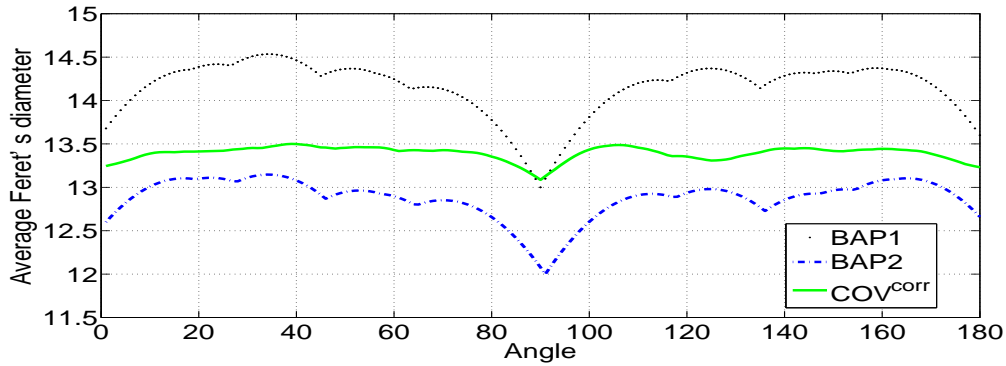


Figure 3.17: Measurements of Feret's diameter for different directions φ averaged over five imaged disks. Correct result is a horizontal line with no variation. The proposed method provides significant improvement over binary approaches. The observed standard deviation of Feret's diameter is 0.3193 for BAP1, 0.2289 for BAP2, and 0.0789 for COV^{corr} .

the grey-scale mode.

To obtain coverage segmentation of the disks, we use the method for pixel coverage segmentation based on double thresholding proposed in [107] and described in Section 2.3.

In the first experiment, we take an image of disks at a distance of $2m$, with the camera view perpendicular to the plane of the paper. In the obtained image, we examine rotational invariance of the (classic) diameter estimation by considering estimation of Feret's diameter for different directions. We estimate the value R , used for calculation of correction term $Corr$, as the average radius over all angles and disks obtained by COV (without correction). Obtained average Feret's diameter over all disks as a function of angle is given in Figure 3.17. The difference between the maximal and minimal value of the average Feret's diameter is $1.534 px$ for BAP1 while for BAP2 it is $1.085 px$. For COV^{corr} it is $0.415 px$. This is an improvement of 3.7 and 2.6 times compared to BAP1 and BAP2, respectively.

In our following experiment, the optical axis of the camera builds a vertical angle with the plane of the imaged paper. Due to this the imaged disks appear as ellipses. We estimate the tilt angle by $\arccos \frac{b}{a}$, where a and b are the major and minor axis of the ellipse, respectively. Illustration of the setup is given in Figure 3.18. To obtain the correction term $Corr$, we use $\varphi = 0$ and $R = \frac{b^2}{a}$, where a and b are estimated by the method without correction. Results of this experiment, for a setup where the true tilt angle is 60° , are shown in Table 3.1. The signed error is given in degrees. Average absolute error is 4.22° for BAP1, 4.60° for BAP2 and 0.591° for COV. Average absolute error for COV^{corr} is 0.569° . This corresponds to a reduction of the error by a factor 7.4 and 8.1 compared with

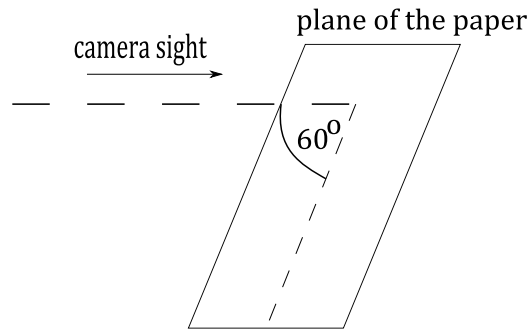


Figure 3.18: We estimate the angle that the optical axis builds with the plane of the imaged paper.

resp. binary approaches.

Table 3.1: Signed error of estimation of the tilt angle, in degrees.

disk	BAP1	BAP2	without correction	corrected
1	-3.557	-5.097	-0.836	-0.808
2	5.380	4.158	-1.097	-1.067
3	-3.557	-5.097	-0.987	-0.960
4	-3.557	-5.097	-0.020	0.005
5	-2.204	-3.557	-0.018	0.006

The obtained results show that also in real imaging conditions COV^{corr} clearly outperforms binary methods for Feret’s diameter estimation and that it consistently improves on COV.

Microscopic Images

We estimate Feret’s diameter on a data set of 368 microscopic images of cell nuclei. Every cell is imaged with primary, secondary magnification and Numerical aperture, respectively set to $(20, 0.63, 0.40)$, $(20, 0.63, 0.75)$, $(20, 1, 0.40)$, $(20, 1, 0.50)$, $(20, 1, 0.75)$, $(40, 0.63, 0.95)$, $(40, 1, 0.95)$. Approximate grid resolutions (in $\frac{px}{\mu m}$) are respectively: 2.0, 2.0, 3.125, 3.125, 3.125, 4.0, 6.25.

Cell nuclei are segmented using a marker-based watershed segmentation to accurately delineate the nuclear boundaries [77]. To obtain coverage segmentations of the cells we use the method of [108] based on a local linear unmixing of the components described in Section 2.3.

Maximal curvature along the boundary of a cell is unknown, so we approximate it by the curvature of a disk of equivalent area as the cell. Since BAP2 shows better performance than BAP1 in estimation of average Feret’s diameter, as presented in

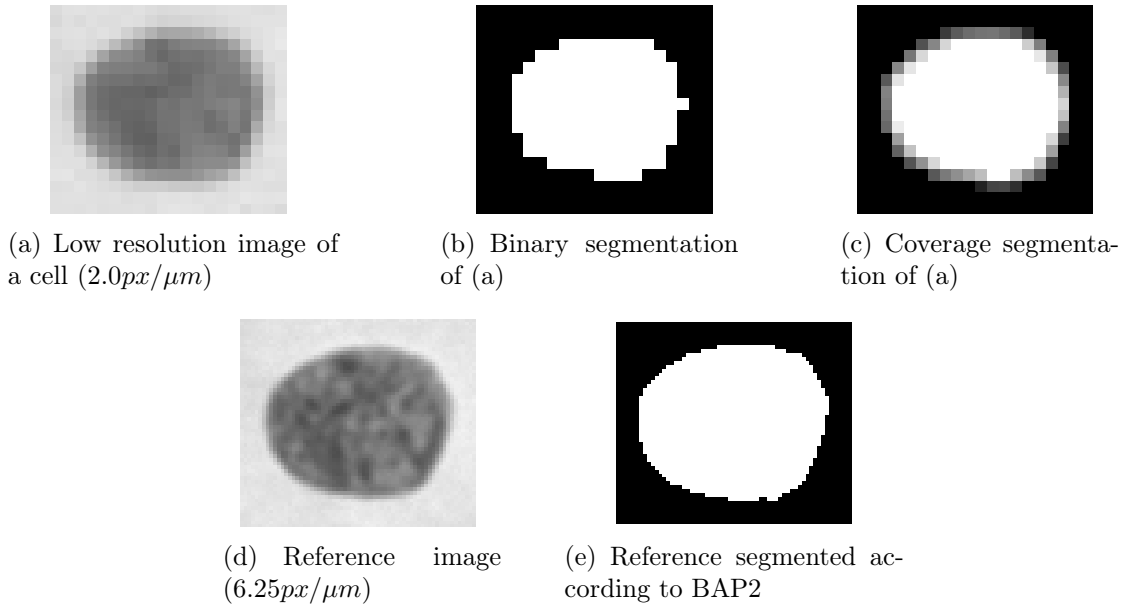


Figure 3.19: Example of an image of a cell used in our experiment (a). We compared estimation of Feret's diameter from binary segmentation (b) and coverage segmentation (c). As a reference value we used the image given in (d) and its binary segmentation (e).

Figure 3.16, we compare COV^{corr} with BAP2. We use the result obtained by BAP2 at the highest available resolution as a reference value \mathcal{F}^{ref} , and then we compare the estimates achieved from the images of lower resolution with this reference. Figure 3.19 presents binary and pixel coverage segmentations of one cell at a lower resolution and the corresponding reference image and its segmentation. Applying BAP2 and COV^{corr} , for every cell C , we estimate the mean squared difference as $\frac{1}{720} \sum_{\varphi} (\mathcal{F}_{\varphi}(C) - \mathcal{F}_{\varphi}^{ref}(C))^2$, $\varphi \in \{0.25^{\circ}, \dots, 180^{\circ}\}$. We average this error over the 368 cells, for each fixed resolution.

Comparison is given in Figure 3.20, for the first six resolution settings, the seventh resolution is used as reference. Obtained values in μm^2 are: (0.6215, 0.5992, 0.1478, 0.1433, 0.1498, 0.0764) for BAP2 and (0.0531, 0.0463, 0.0490, 0.0536, 0.0481, 0.0413) for COV^{corr} . The proposed method gives better result on the poorest images (lowest resolution) than BAP2 applied to the best images (highest resolution). The average reduction of the error over all settings is 5.96 times.

Obtained results clearly show that COV^{corr} can be used for improved estimation of Feret's diameter on real images.

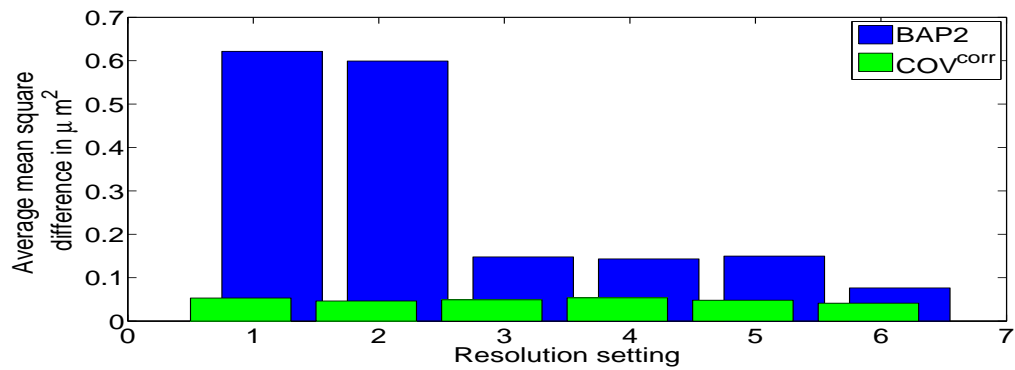


Figure 3.20: Average mean square difference between Feret's diameter estimated with resp. method on each of the first six resolution settings and using BAP2 on the highest (reference) resolution. COV^{corr} shows excellent agreement with the reference (presumed best estimate).

Chapter 4

Advanced morphological distances

This chapter is based on paper "Advanced morphological distances based on dilation and erosion" [26]. The importance of morphological distances is briefly described in Section 4.1. The mathematical model and some notation we use for our study are given briefly in Section 4.2. In Section 4.3 we explore problems related to computing existing morphological distances between gray scale images. In Section 4.4 we propose new morphological distances for comparing objects based on their digital image representation. Experimental evaluation is given in Section 4.5.

4.1 Importance of morphological distances

The usage of a distance related to a specific shape property to compare objects from their digital image representations has a great potential in many challenging and topical research task. For instance, technological developments in the past two decades have greatly advanced the field of bioimaging and made tracking particles such as molecules, organelles or viruses using their digital images of key importance for the investigation of processes in cells like virus infections, intracellular transports or gene transcriptions [98, 99]. As in [45], measuring of displacements of a particle along the specific directions can be of great importance in particle tracking, and a distance which is more sensitive to particle moves just along these directions than to all the other directions is specially suitable for this purpose. In geographical information science, shapes are in a large number of cases studied to make conclusions on specific phenomena based on their digital image representation. Lately, a highly topical researching is on melting and movements of Antarctic ice shelf from satellite images [44, 59]. Making a distance more sensitive to internal shape changes, such as change of connectivity, is highly desirable in order to distinguish between relevant and irrelevant changes when satellite images

of an ice shelf at different time frames are compared. A relevant change can be separating an iceberg from a shelf, when the shape becomes disconnected, and an irrelevant change could be melting of the coast due to higher temperatures.

We mentioned just some applications in which there exists a strong need for using morphological distances. Although the potential of their usage is great, existing morphological distances have strong drawbacks which significantly limit their broader usage. The work presented in the thesis is a great step toward overcoming the drawbacks and making morphological distances more suitable for a wider usage. In following, we give an overview of applications in which existing morphological distances have been already successfully used.

The Hausdorff distance, d_H , is frequently observed as a minimal radius of a ball that a set A should be dilated with to become a superset of a set B and vice versa as given by Equation 2.36 and Equation 2.37. In [103] authors shown that, by performing morphological dilations, erosions and basic set operations (union and intersection) on X and Y , can be constructed a sequence of sets $\{S_i\}$, $i = 1, \dots, n$ such that $\sum_{i=1, \dots, n} d_H(S_i, S_{i+1}) = d_H(X, Y)$ and $d_H(S_i, S_{i+1}) \leq \frac{d_H(X, Y)}{n}$. To

form such sequence interpolating two shapes, in order to simulate geometrical changes of physical phenomena, Equation 2.36 and Equation 2.37 are used for comparing image data in [90, 126]. The morphological distance d_D based on the number of subsequent dilations of A to cover B that allows usage of an arbitrary structuring element given by Equation 2.38 is used in [93] to compare shapes of digital elevation models. As an extension of d_D to gray scale images, dilation distance, d_{dilate} , and erosion distance, d_{erode} , given by Definition 2.5.2 are used for ranking images representing variable specific phenomena across spatial positions in [92] and for morphing, i.e. transforming one digital image into another via a sequence of intermediate images in [91].

4.2 Model description

A function $f : D \rightarrow \mathbb{R}$ can be easily represented as a set of points by its umbra $\mathcal{U}(f) = \{(x, y) \in D \times \mathbb{R} \mid y \leq f(x)\}$ and dilation and erosion applied. A function frequently models a signal which carries information about a phenomenon. Definition 2.5.2 is given for functions. If we switch \wedge and \vee and use $\ominus nO$ instead $\oplus nO$, Equation 2.39 becomes Equation 2.40. Therefore, all conclusions we derive for d_{dilate} can also be dually derived for d_{erode} . To clearly illustrate the shortcomings of d_{dilate} , we observe functions: $[a, b] \rightarrow \mathbb{R}$. The extension of all considerations to discrete two dimensional functions is straightforward.

4.3 Examples and motivation for improvement

Although a good performance of morphological distances is shown in different applications, they all have drawbacks that seriously limit their broader usage. Namely, how much A should be dilated to become a superset of B depends exclusively on the furthest point of B from A, and vice versa. The furthest points are frequently outliers and d_H and d_D strongly depend on them. This frequently makes them useless in real applications. Because they are on sums that depend on all points of compared objects, d_{dilate} and d_{erode} are less sensitive to outliers, but authors notice some of their drawbacks. The strongest drawback of d_{dilate} is that it cannot be applied on image pairs of a certain type as it does not provide a finite value. A vague explanation of situations when this problem arises is given in [92]. In following, we give a proposition which provides the clear condition that determines for which image pairs $d_{dilate}(f_1, f_2) = \min\{n \mid A((f_1 \wedge f_2) \oplus nO) > A(f_1 \vee f_2)\}$ can and cannot be computed.

4.3.1 Necessary and sufficient conditions for computing d_{dilate}

Proposition 4.3.1. *For a function pair $f_1, f_2 : [a, b] \rightarrow \mathbb{R}$, the necessary and sufficient condition for $d_{dilate}(f_1, f_2) \in [0, \infty)$ is:*

$$\max_{x \in [a, b]} ((f_1 \wedge f_2)(x)) > \frac{A(f_1 \vee f_2)}{b - a}. \quad (4.1)$$

Proof. We perform the proof using negations of the conditions:

$$\max_{x \in [a, b]} ((f_1 \wedge f_2)(x)) \leq \frac{A(f_1 \vee f_2)}{b - a} \Leftrightarrow d_{dilate}(f_1, f_2) \notin [0, \infty). \quad (4.2)$$

We have:

$$\begin{aligned} \max_{x \in [a, b]} ((f_1 \wedge f_2)(x)) &\leq \frac{A(f_1 \vee f_2)}{b - a} \Leftrightarrow \\ (b - a) \max_{x \in [a, b]} ((f_1 \wedge f_2)(x)) &\leq A(f_1 \vee f_2). \end{aligned} \quad (4.3)$$

As $(f_1 \wedge f_2) \oplus nO$ is limited from above by $\max_{x \in [a, b]} ((f_1 \wedge f_2)(x))$, we have:

$$\max_{n \in \mathbb{N}} (A((f_1 \wedge f_2) \oplus nO)) = (b - a) \max_{x \in [a, b]} ((f_1 \wedge f_2)(x)), \quad (4.4)$$

and we can substitute $\max_{n \in \mathbb{N}} (A((f_1 \wedge f_2) \oplus nO))$ with $(b - a) \max_{x \in [a, b]} ((f_1 \wedge f_2)(x))$.

$$\max_{n \in \mathbb{N}} (A((f_1 \wedge f_2) \oplus nO)) \leq A(f_1 \vee f_2) \Leftrightarrow \quad (4.5)$$

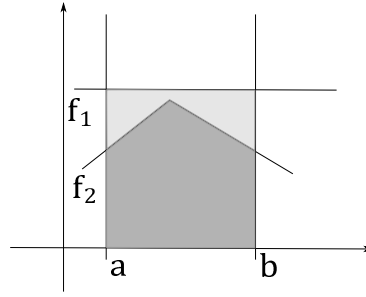


Figure 4.1: An example of $d_{dilate}(f_1, f_2) \notin [0, \infty)$ because $\max_{x \in [a, b]} ((f_1 \wedge f_2)(x)) < \min_{x \in [a, b]} ((f_1 \vee f_2)(x))$.

$$(\forall n \in \mathbb{N})(A((f_1 \wedge f_2) \oplus nO)) \leq A(f_1 \vee f_2) \Leftrightarrow \quad (4.6)$$

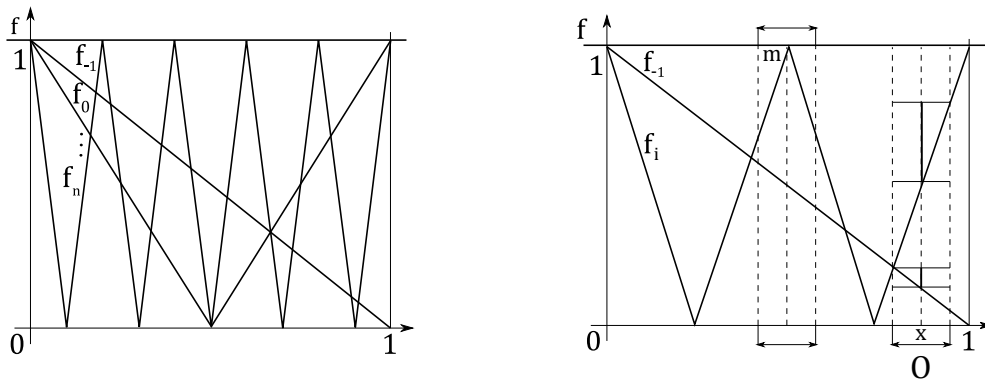
$$d_{dilate}(f_1, f_2) \notin [0, \infty) \blacksquare \quad (4.7)$$

We notice that the consideration applies for both, positive and negative, function values. From Proposition 4.3.1 it follows that $d_{dilate}(f_1, f_2)$ does not provide meaningful result for a large number of function pairs $\{f_1, f_2\}$ within a finite range. For instance, $\max_{x \in [a, b]} ((f_1 \wedge f_2)(x)) < \min_{x \in [a, b]} ((f_1 \vee f_2)(x))$ implies $d_{dilate}(f_1, f_2)$ does not have a finite value, regardless of the form of f_1 and f_2 and changes in their gray values. This is illustrated in Figure 4.1.

4.3.2 Insensitivity of d_{dilate} to changes in gray values

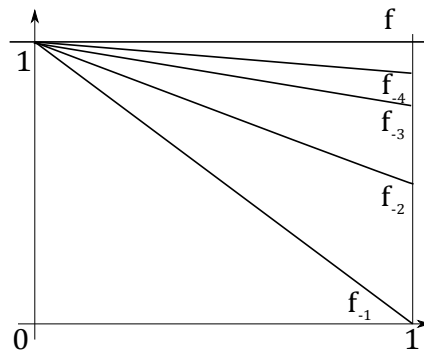
Another drawback of d_{dilate} is a situation in which d_{dilate} is not sensitive to significant changes in differences of image values that can carry valuable information about imaged objects. Let us assume that Proposition 4.3.1 is satisfied and that we are computing $d_{dilate}(f, f_i)$ where $f(x) = 1$ is a constant function and f_i is a piece-wise linear function namely a *triangle wave* ranging between 0 and 1 with the period $p = 2^{-i}$: $f_i(x) = \frac{2}{p} \left(|(x \bmod p) - \frac{p}{2}| \right)$, where mod denotes the modulo operation. We observe functions on the interval $[0, 1]$ as given in Figure 4.2(a) for $i \in \{-1, 0, 1, 2, \dots, n\}$. It is easy to conclude that $d_{dilate}(f, f_i) = \min\{n \mid \forall x \in [a, b], f_i \oplus nO(x) = 1\}$. Figure 4.2(b) illustrates a neighborhood of a maximum m of f_i for which $f_i \oplus O$ becomes equal to 1 in a single dilation step by a structuring element O . Observing just the spreading of such neighborhoods, we conclude:

$$d_{dilate}(f, f_i) = \min\{n \mid n \geq \frac{1}{2^{i+1} \cdot l}, n \in \mathbb{N}\}, \quad (4.8)$$



(a) A sequence of triangular waves ranging between 0 and 1, $f_i(x) = \frac{2}{p} \left(|(x \bmod p) - \frac{p}{2}| \right)$, where $p = 2^{-i}$.

(b) A neighborhood of a maximum m that becomes equal to 1 and the increment of a value $f_i(x)$ in a single step of dilation by O .



(c) The sequence of triangular waves for $i \in \{-4, -3, -2, -1\}$.

Figure 4.2: A set of functions for which d_{dilate} does not provide meaningful result. The distribution of maxima solely determines the value of d_{dilate} while other properties are neglected in 4.2(a). Higher slope of f_i can cause smaller distance regardless of f in 4.2(b). $d_{dilate}(f, f_i)$ is the same for all f_i , $i \in \{-4, -3, -2, -1\}$ presented in 4.2(c)

where $0 < l \leq 1$ is the width of O . The distance decreases exponentially with i . We emphasize that other properties except the distribution of maxima of f_i , such as minima or shape of f_i leading to strong changes in differences in gray values in images, can be changed without any impact on $d_{dilate}(f, f_i)$. For example, $d_{dilate}(f, f_{-1}) = d_{dilate}(f, f_{-2}) = \dots = d_{dilate}(f, f_{-n})$, $n > 0$, although f_i becomes closer to f as i decreases. More precisely, the minimum of f_i becomes closer to 1 and the slope becomes closer to 0 with decreasing i , as illustrated in Figure 4.2(c).

Let us, now, observe $f_i \oplus O(x)$ for an arbitrary $x \in [0, 1]$ presented in Figure

4.2(b). In a single step of the dilation the increment of f_i is $\Delta f_i \oplus O(x) = s_i \cdot \frac{1}{2}$, where $s_i = 2^{i+1}$ is the absolute value of the slope of f_i . The increment $\Delta f_i \oplus O(x)$ is directly proportional to the absolute value of the slope. Due to this, $d_{dilate}(f, f_i)$ would strongly decrease with i if f is not constant and reaches values lower than 1, regardless of the shape of f . In many situations, this can be a disadvantage. For example, if f has light changes in values representing image regions without edges and high slope of f_i represents strong changes of the border.

When Proposition 4.3.1 is not satisfied, then it is not possible to apply Definition 2.5.2 and [92] suggest two modification to be used for that matter. The first one is to compute the distance as:

$$d_{dilate}(f_1, f_2) = \min\{n \mid (f_1 \wedge f_2) \oplus nO = (f_1 \wedge f_2) \oplus (n+1)O\} = \min\{n \mid (f_1 \wedge f_2) \oplus nO = \max_{x \in [a,b]} (f_1 \wedge f_2)(x) = const\}. \quad (4.9)$$

Because a constant should be reached by dilations, d_{dilate} depends exclusively on the distribution of maxima of $f_1 \wedge f_2$ when this suggestion is used. All the other properties are neglected, as it is already discussed.

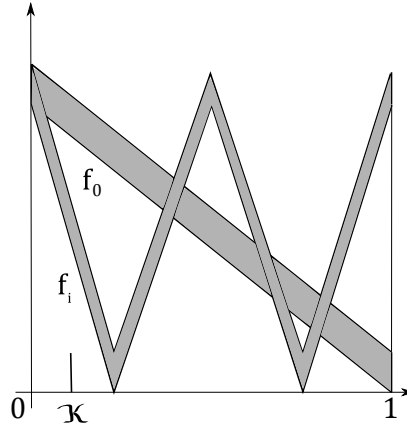


Figure 4.3: $\delta_{\mathcal{K}}(f_i)$ for a one-point wide structuring function \mathcal{K} causes the same change of the area (shaded region), regardless on i .

The second suggestion for modifying Definition 2.5.2 in [92] was to use structuring functions for computing d_{dilate} . However, details on how this can be done and on impact of this modification are missing. To illustrate a problem with choosing a structuring function, we refer to the sequence of described piece-wise linear function f_i and $\delta_{\mathcal{K}}(f_i)$ for a one-point wide structuring function \mathcal{K} presented in Figure 4.3. Regardless on i , the change of $A(f_i)$, presented as shaded area in the figure, is equal to $h \cdot \frac{1}{2^i} \cdot 2^i = h$ in a single step of the dilation, where h is the height

of \mathcal{K} . Usage of the structuring function \mathcal{K} causes the same change of $A(f_i)$ and consequently d_{dilate} is the same for all i , regardless of the function f . Minima of an image function can represent holes or disconnected regions inside a shape and f can represent a region without holes. In such a situation, the behavior of d_{dilate} is inappropriate. A dilation by a structuring function is performed in a similar manner as the dilation by the flat structuring element, but image values are increased by the values of the used structuring function before choosing maximum. Due to this, the higher slope of an image function implies the higher increment in a single step of the dilation for the same structuring function, as already considered for the dilation by a flat structuring element. Due to this, $d_{dilate}(f, f_i)$ would necessarily decrease with i when widening the support of the used structuring function, although this is not appropriate behavior when the number of holes increases, for instance.

4.4 New morphological dilation and erosion distances

In this section, we propose new morphological distances based on the same morphological concepts as d_{dilate} and d_{erode} which overcome problems discussed in the previous section. We base our definitions on Definition 2.4.6, but use the term of *adaptive structuring function* that changes its values depending on $x \in [a, b]$. For this purpose, we relate a structuring function to $|f_1(x) - f_2(x)|$, $x \in [a, b]$.

The dilation of a concave function f with a convex structuring function \mathcal{K} might produce additional local extrema to $\delta_{\mathcal{K}}(f)$ as illustrated in Figure 4.4(a). The same is valid for erosion of a convex f with a concave \mathcal{K} . A non-symmetric structuring function \mathcal{K} produces displacement of extrema for function f as illustrated in Figure 4.4(b). Due to the above-mentioned, to preserve basic morphological properties of f , we use only symmetric structuring functions in defining morphological distances, which are concave when performing a dilation and convex when performing an erosion.

We propose novel morphological distances based on gray scale morphological dilation and erosion with structuring functions as:

Definition 4.4.1. For a function pair $f_1, f_2 : [a, b] \rightarrow \mathbb{R}$ and $x \in [a, b]$, let \mathcal{K}_x be a structuring function which is concave, symmetric, non-negative and satisfies the property $\max_{z \in O}(\mathcal{K}_x(z)) = \max_{z \in O, x-z \in [a, b]} |f_1(x-z) - f_2(x-z)|$ on a support O . For \mathcal{K}_x , the new dilation distance is defined as:

$$d'_{dilate}(f_1, f_2) = \int_a^b \delta_{\mathcal{K}_x}(f_1 \wedge f_2)(x) - (f_1 \wedge f_2) \oplus O(x) dx. \quad (4.10)$$

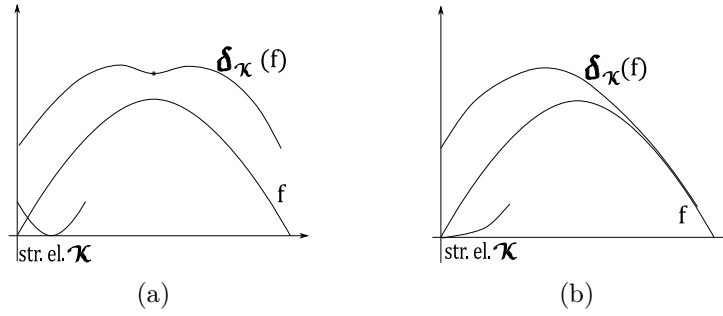


Figure 4.4: Dilation of a concave function by a convex structuring element provides a minimum in (a), and dilation by a non symmetric structuring element causes displacement of maximum in (b).

Definition 4.4.2. For a function pair $f_1, f_2 : [a, b] \rightarrow \mathbb{R}$ and $x \in [a, b]$, let \mathcal{K}_x be a structuring function which is convex, symmetric, non-negative and satisfies the property $\max_{z \in O}(\mathcal{K}_x(z)) = \max_{z \in O, x-z \in [a, b]} |f_1(x-z) - f_2(x-z)|$ on a support O . For \mathcal{K}_x , the new erosion distance is defined as:

$$d'_{erode}(f_1, f_2) = \int_a^b (f_1 \vee f_2) \ominus O(x) - \varepsilon_{\mathcal{K}_x}(f_1 \vee f_2)(x) dx. \quad (4.11)$$

To illustrate the usage of the proposed definitions and computation of the defined distances for discrete functions, we give following example of computing $\delta_{\mathcal{K}_x}((f_1 \wedge f_2))(x) - (f_1 \wedge f_2) \oplus O(x)$. Two discrete functions, f_1 and f_2 , are respectively given in Figure 4.5(a) and 4.5(b). Their absolute difference $|f_1 - f_2|$ is given in Figure 4.5(c). For this example we use the support for structuring function O given in Figure 4.5(d). In the neighborhood defined by O of every point of the domain the maximal value of $|f_1 - f_2|$ is computed. In Figure 4.5(e) is given such computation for the domain point $x = 3$. After that, a structuring function that have the maximal value equal to the computed is defined for every point of the domain. We stress out that the imposed properties for the structuring functions are that they all have the maximal value computed in the described manner, they are all symmetric and defined on O . The structuring functions can differ in all the other properties across the domain points. In Figure 4.5(f) is given a constant structuring function $\mathcal{K}_3(z) = \max_{z \in O} |f_1(3-z) - f_2(3-z)|$, $z \in O$ that we use in this example. At a point of the domain, the difference of $\delta_{\mathcal{K}_x}((f_1 \wedge f_2))$ and $(f_1 \wedge f_2) \oplus O(x)$ is computed. We illustrate the computation in Figure 4.5(h) for $x = 3$. To compute $d'_{dilate}(f_1, f_2)$, the computation is performed and the difference summed over all the domain points.

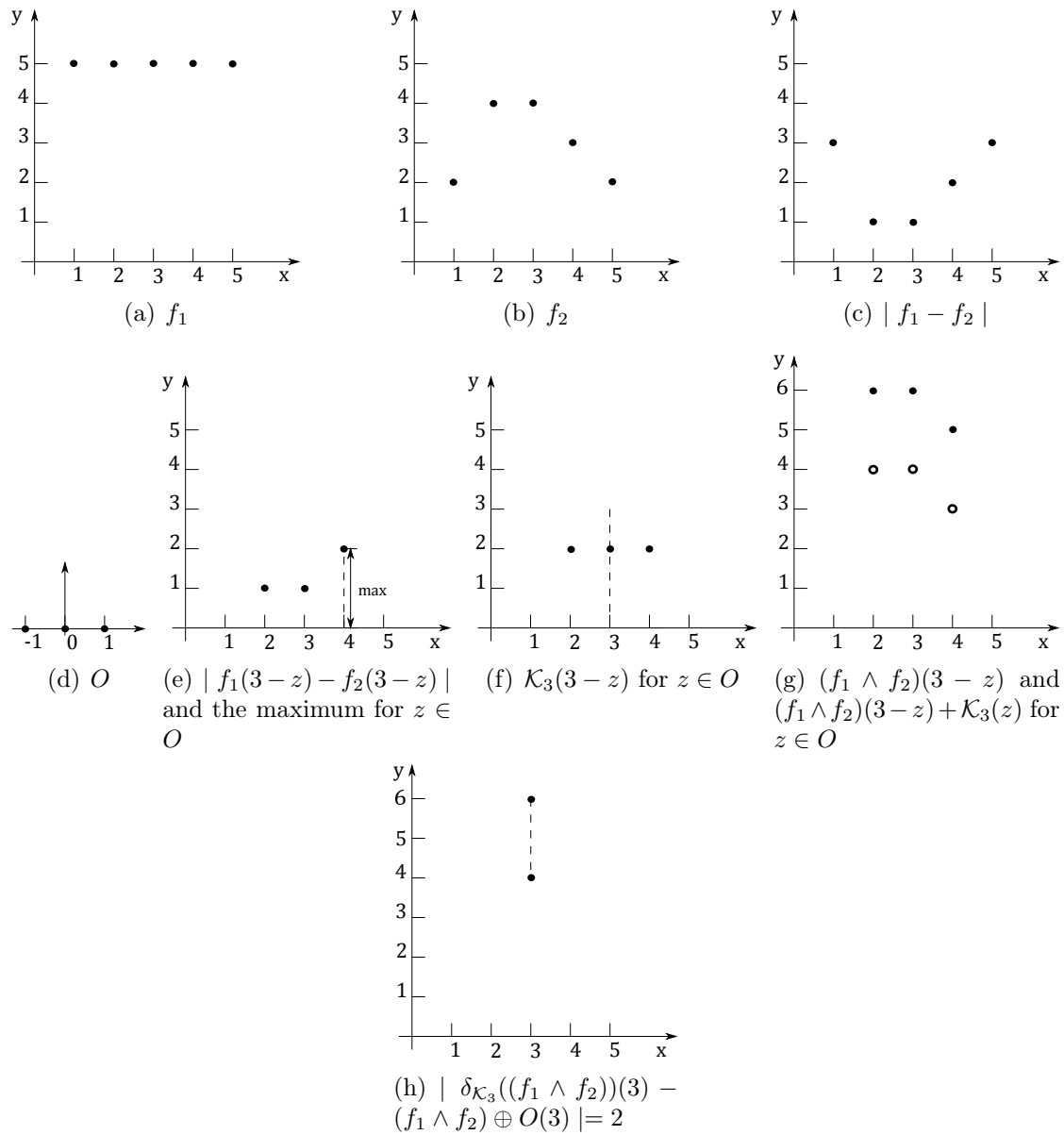


Figure 4.5

We emphasize that d_{dilate} cannot be computed for given example because $(f_1 \wedge f_2)(x) < (f_1 \vee f_2)(x), \forall x \in \{1, 2, 3, 4, 5\}$. Contrary to that, d'_{dilate} can be computed for any pair of images. All the necessary operations for computing d'_{dilate} can be performed and, instead of sequentially performed dilations which value is limited from above, d'_{dilate} is defined via a single step of the dilation by the structuring

function \mathcal{K}_x that provides $\delta_{\mathcal{K}_x}((f_1 \wedge f_2)(x)) \geq (f_1 \wedge f_2) \oplus O(x)$, $x \in D$ and the problem from Proposition 4.3.1 is resolved.

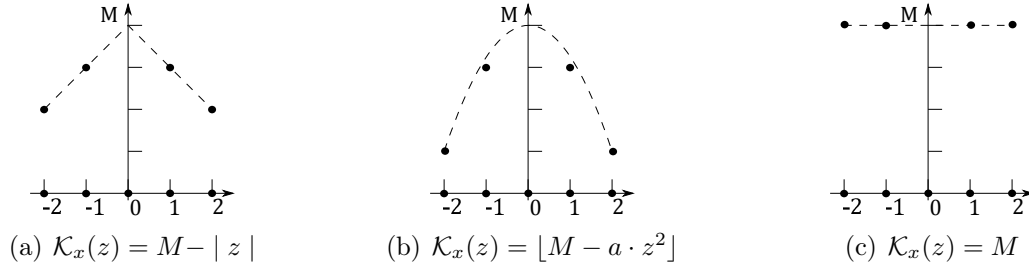


Figure 4.6: Examples of computing a structuring function \mathcal{K}_x . To shorten notation, we use the letter M for $\max_{z \in O} |f_1(x - z) - f_2(x - z)|$. $\lfloor x \rfloor$ denotes the nearest smaller integer of x .

A structuring function can be chosen suitable to deal with image values in the neighborhood of x which can differ in different parts of an image. Such a selection is research for itself and we illustrate just some of possible, very simple structuring functions in Figure 4.6. Together with the illustrations of the structuring functions are given their analytic expressions $\mathcal{K}_x(z) = M - |z|$, $\mathcal{K}_x(z) = \lfloor M - a \cdot z^2 \rfloor$, $\mathcal{K}_x(z) = M$, where $M = \max_{z \in O} |f_1(x - z) - f_2(x - z)|$.

For our purpose, we choose to use the type of the structuring function presented in Figure 4.6(c), i.e. a constant structuring function equal to the $\max_{z \in O} |f_1(x - z) - f_2(x - z)|$ over the whole support. In this manner, the proposed distances enable intuitive clear and simple consideration of properties of sets of pixels at which images differ. This is done in the similar manner as when extracting relevant image properties from a single image using morphological operations. We obtain results given in the first row of Table 4.1 if we choose a support O_1 presented in Figure 4.7(a) and a structuring function which is constant on it to compute $d'_{erode}(K, K_i)$ for shapes in Figure 2.14. We easily make conclusions on certain types of object changes by observing the obtained values.

The highest value is reached for the case with a change of connectivity. Smallest value is reached for the cases where pixels at which images differ are surrounded by the background, which is case for protrusions. Values between appear for changes in the border. To more strongly highlight the protrusions in the vertical direction the support O_2 presented in Figure 4.7(b) can be considered. The results for d'_{dilate} for constant structuring function on O_2 are given in the second row of Table 4.1 where d'_{dilate} escalate only when this change occurs.

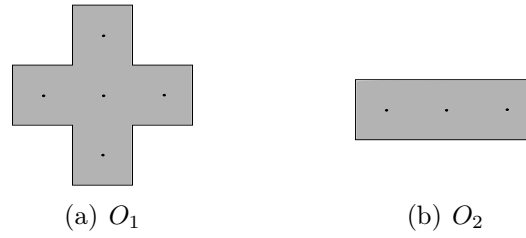


Figure 4.7: A structuring element that stays the same for rotations for $\frac{\pi}{2}$ and a horizontal structuring element

Table 4.1: New distances for Figure 2.14

	K, K_1	K, K_2	K, K_3	K, K_4
\mathcal{O}_1	9	3	2	3
\mathcal{O}_2	7	7	13	7

As the absolute differences between f_1 and f_2 increase, the value (height) of \mathcal{K}_x increases, and the value of $d'_{dilate}(f_1, f_2)$ with it. Higher slope at a point causes higher values of the dilation by \mathcal{K}_x for the same reason as described for Figure 4.2(b) for flat structuring element, but at the same time higher value of $\delta_{\mathcal{K}_x}(f_1 \wedge f_2)(x)$. It is not possible to freely change the differences between compared functions without any impact on d'_{dilate} and $d'_{dilate}(f, f_i)$ monotonously grows with i for the triangular wave considered in Section 4.3. The behavior of d'_{dilate} for the triangular wave when $i \in \{-4, -3, \dots, 3, 4\}$ is presented in Figure 4.8 for the constant structuring function on the support $O = [-0.1, 0.1]$.

If we choose the one-point wide support for the structuring function to compute d'_{dilate} , it reduces to L_1 distance. Consequently $d(f, f_i) = const$ for such support for sequence of functions from Figure 4.2. If the support is the widest possible and completely covers $[a, b]$, d'_{dilate} behaves as d_∞ , if the constant structuring function is chosen. The appropriate behavior of d'_{dilate} in experimental settings, with regards to both changes of objects in the spatial domain and image intensities, is shown in Section 4.5.1 and Section 4.5.2.

4.4.1 Metric properties for d'_{dilate} and d'_{erode}

The proposed distances are semimetrics. In following we consider metric properties of d'_{dilate} . The consideration for d'_{erode} is analogous.

1. Non negativity: $d'_{dilate}(f_1, f_2) \geq 0$ for every f_1 and f_2 .

This property holds because $\mathcal{K}_x \geq 0$ for every $x \in [a, b]$. Consequently, $\delta_{\mathcal{K}_x}((f_1 \wedge f_2)(x)) \geq (f_1 \wedge f_2) \oplus O(x)$ for every $x \in [a, b]$.

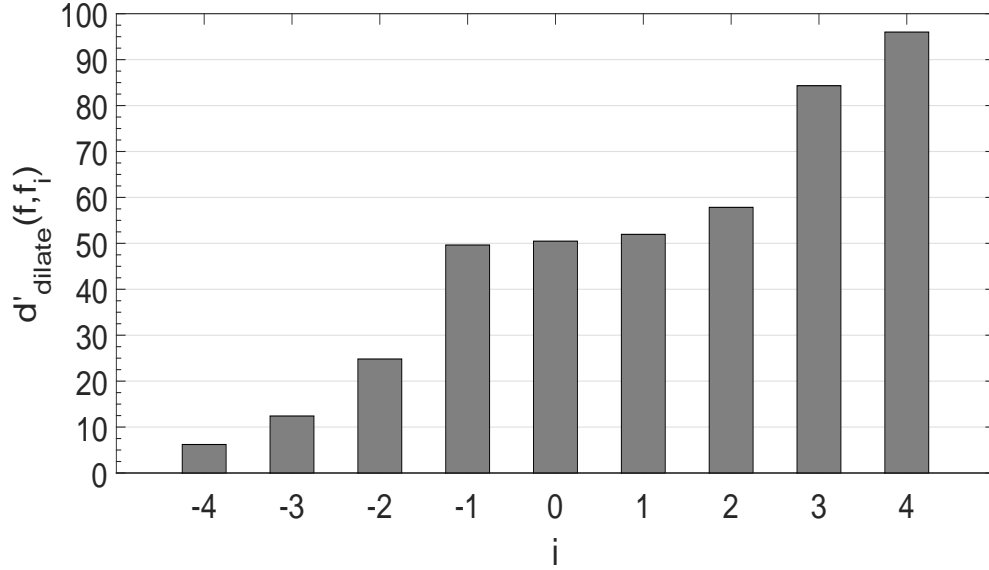


Figure 4.8: $d'_{dilate}(f, f_i)$ for the triangular wave. We use the constant function on the support $O = [-0.1, 0.1]$.

2. Separability: $f_1 = f_2 \Leftrightarrow d'_{dilate}(f_1, f_2) = 0$ for every f_1 and f_2 .

This is true because:

(\Rightarrow) If $f_1 = f_2$, then $\max_{z \in O}(\mathcal{K}_x(z)) = 0$ for every $x \in [a, b]$. This implies $\delta_{\mathcal{K}_x}(f_1 \wedge f_2)(x) = (f_1 \wedge f_2) \oplus O(x)$ for every $x \in [a, b]$.

(\Leftarrow) We prove by contra-position: If $f_1 \neq f_2$ then $d'_{dilate}(f_1, f_2) \neq 0$. Assume that $f_1 \neq f_2$. Then, $\max_{z \in O}(\mathcal{K}_x(z)) > 0$ for some $x \in [a, b]$. Consequently, $\delta_{\mathcal{K}_x}(f_1 \wedge f_2)(x) > (f_1 \wedge f_2) \oplus O(x)$ for some $x \in [a, b]$.

3. Symmetry: $d'_{dilate}(f_1, f_2) = d'_{dilate}(f_2, f_1)$ for every f_1 and f_2 .

This property trivial holds because: $f_1 \wedge f_2 = f_2 \wedge f_1$.

4. Triangle inequality does not hold: there exist f_1, f_2, f_3 such that $d'_{dilate}(f_1, f_2) + d'_{dilate}(f_2, f_3) < d'_{dilate}(f_1, f_3)$.

Let us consider the function triplet presented in Figure 4.9, where O is large enough to cover the whole domain and

$$\mathcal{K}_x(z) = \begin{cases} \max_{z \in O}(|f_1(x+z) - f_2(x+z)|) & \text{if } z = 0 \\ 0 & \text{otherwise .} \end{cases}$$

Here, distance values are $d'_{dilate}(f_1, f_2) = 6$, $d'_{dilate}(f_1, f_3) = 9$ and $d'_{dilate}(f_2, f_3) = 2$, therefore $d'_{dilate}(f_1, f_2) + d'_{dilate}(f_2, f_3) = 8$, while $d'_{dilate}(f_1, f_3) = 9$.

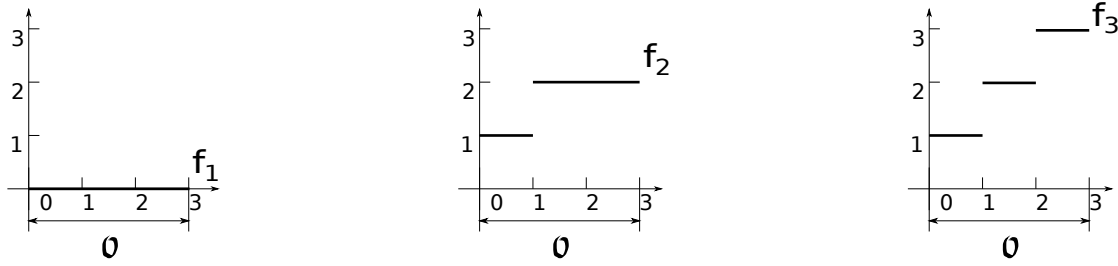


Figure 4.9: Function triplet, f_1, f_2, f_3 , for which the triangle inequality $d'_{dilate}(f_1, f_2) + d'_{dilate}(f_2, f_3) \geq d'_{dilate}(f_1, f_3)$ is not satisfied. Distance values are $d'_{dilate}(f_1, f_2) = 6$, $d'_{dilate}(f_1, f_3) = 9$ and $d'_{dilate}(f_2, f_3) = 2$.

4.5 Experimental evaluation

4.5.1 Behavior depending on changes in gray levels

To show the advantage of using d'_{dilate} over d_{dilate} in a realistic experimental setting to resolve a problem similar to the one illustrated on the toy example in Section 4.3.2, we compute d_{dilate} and d'_{dilate} between a simulated, but yet realistic, set of images. The differences in image intensities including important information are successively increased. Namely, we successively add noise to an image. The noise causes larger fluctuations of image intensity values introducing smaller local maxima and higher slopes of the image function. Due to this, $A(f_1 \wedge f_2)$ reaches $A(f_1 \vee f_2)$ in a single dilation step and d_{dilate} is equal to 1 regardless of the differences in gray vales which carry important information. In contrast, valuable conclusions can be made based on values of d'_{dilate} .

More particularly, we considered a two-dimensional Gaussian $G(\mu_x, \mu_y; \sigma)$, as often considered in studies of single particle tracking experiment [76]. Formally,

$$f_1(\mu_x, \mu_y) = b + A \cdot G(\mu_x, \mu_y; \sigma) + \zeta, \quad (4.12)$$

where b is the background, A is the amplitude and σ is the standard deviation of the Gaussian, and ζ is noise.

The image f_1 is corrupted by Poisson noise as done in [113] and with this procedure the image f_2 is constructed in the following manner. We set the realistic values for the parameters [113]: fixed background $b = 1$, fixed standard deviation

of the Gaussian $\sigma = 1.5$ and variable amplitude $A \in \{100, 200, \dots, 1000\}$, where a larger amplitude means brighter and more distinctive particles. For every value A we successively add Poisson noise using DIPimage function *noise* [42]. Poisson noise is signal dependent. The intensities of the input image divided by the conversion variable p are used as mean values for the Poisson distribution. On our image set, this means that, as values of image function are increased by increasing A , increases the mean value of the noise and images are corrupted to a larger extent than images with smaller amplitude.

We note that the parameter p is inversely proportional to the amount of added noise, i.e., smaller values of p correspond to larger amount of noise. An example of f_1 for $A = 500$ and f_2 for the same A and $p = 0.5$ is given in Figure 4.10. For every selection of the aforementioned parameters, we generate 1000 images (denoted here as f_1) with randomly placed the position (μ_x, μ_y) of particle. These 1000 images are corrupted by the above aforementioned procedure. Finally, we computed the average value of $d_{dilate}(f_1, f_2)$ and $d'_{dilate}(f_1, f_2)$ over all the image pairs $\{f_1, f_2\}$ defined as above. For this experiment, we use image patches of size 11×11 and the constant structuring function $\mathcal{K}_{\mathbf{x}}(\mathbf{z}) = \max_{\mathbf{z} \in O} |f_1(\mathbf{x} - \mathbf{z}) - f_2(\mathbf{x} - \mathbf{z})|$ on the support $O = \{-1, 0, 1\} \times \{-1, 0, 1\}$.

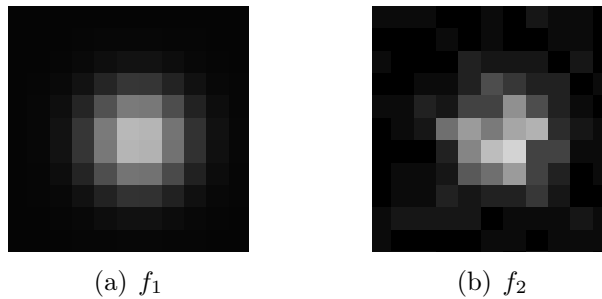


Figure 4.10: Examples of two-dimensional Gaussians with the amplitude $A = 500$. f_2 is corrupted by Poisson noise with the conversion factor $p = 0.5$.

The results are depicted in Figure 4.11. The obtained results show that the old dilation distance d_{dilate} does not distinguish between images if they are corrupted with different amount of noise or have different amplitudes. Moreover, it does not change its value at all. In contrast, the new dilation distance d'_{dilate} increases with increasing amplitude A and with increasing amount of noise matching the effect of Poisson noise on signal presented by the images.

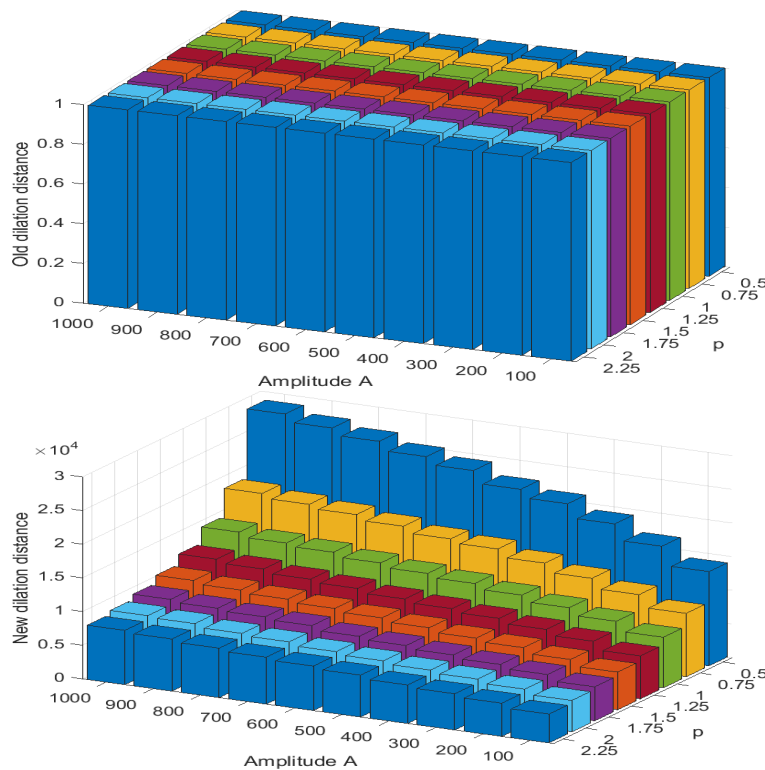


Figure 4.11: The averaged distance between noise free f_1 and degraded object f_2 for different noise and amplitude levels. Up: Old morphological dilation distance d_{dilate} . Bottom: New morphological dilation distance d'_{dilate} . Parameter p is the conversion factor computed as the intensity of the image divided by the mean value for the Poisson distribution.

4.5.2 Particle tracking

In this section, we show that the new dilation distance d'_{dilate} follows well spatial changes of an object. In particular, we present the applicability of the new dilation distance d'_{dilate} to a challenging problem of single particle tracking [13]. At the same time we show insensitivity of d_{dilate} to changes of image data which correspond to object changes in the spatial domain.

A typical image analysis pipeline for single particle tracking analysis includes: (1) detection of single particles in every frame, (2) connection of the previously detected particles into trajectories and (3) analysis of the obtained trajectories. A drawback of such analysis is that an incorrect detection of single particles or assigning a particle to a wrong trajectory leads to a biased interpretation of the data.

For a real experimental data, it is not possible to know the exact position of a particle. Therefore, we use a highly realistic synthetic data generated by SMeagol software [66], which generates single molecule microscopy time-lapse videos by incorporating complex reaction diffusion kinetics that occur in cells as well as simulates realistic microscopy imaging. We generate a movie of 99 frames with two molecules in an E. coli cell geometry, and some example frames are depicted in Figure 4.12.

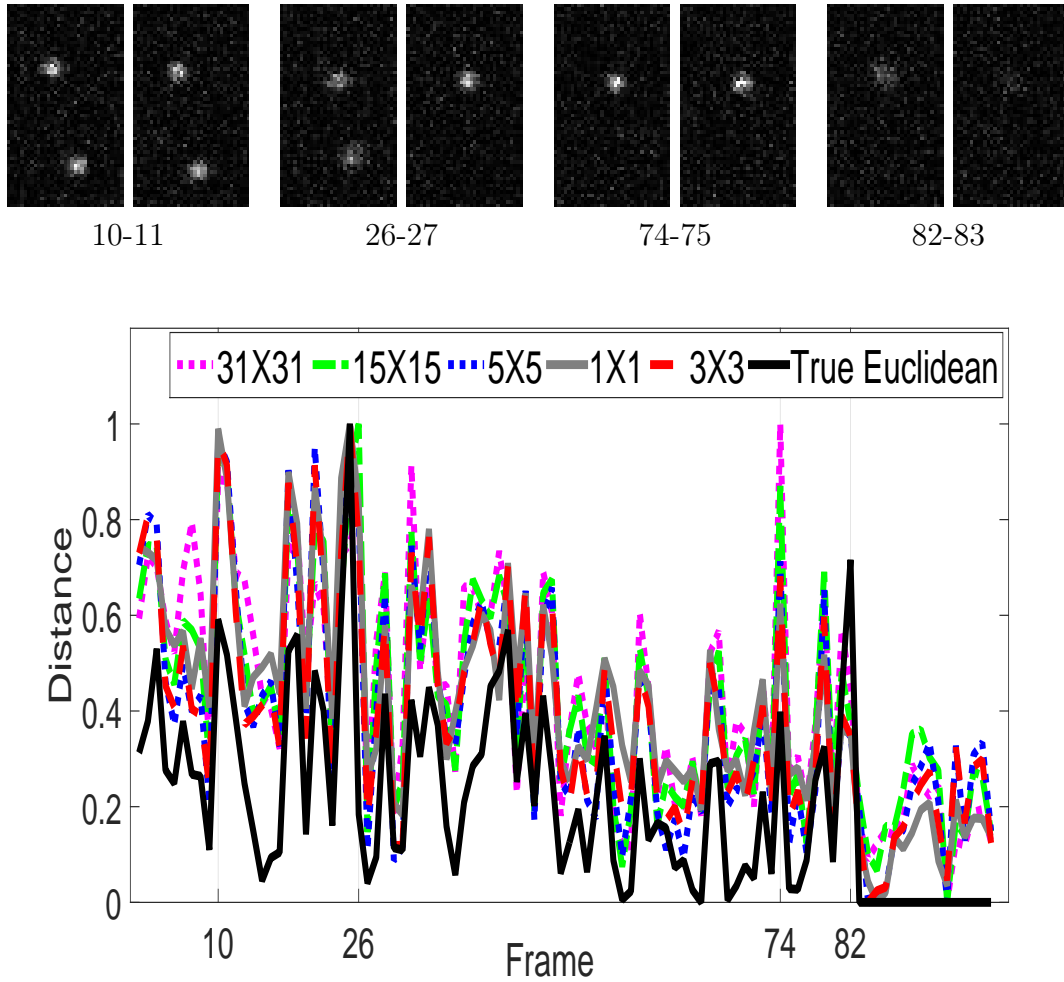


Figure 4.12: Top: Example of different consecutive frames. Bottom: The d'_{dilate} between consecutive frames, for different structuring elements, versus the Euclidean distance between the position of molecules for all frames.

For this experiment, we compute the d'_{dilate} for every two consecutive frames in the movie. For the set of pairs of consecutive frames, we compute the distance

for different size of the support and the constant structuring function. The results are shown in Figure 4.12, together with the true Euclidean distance between the molecules, where all distances are normalized for the purpose of comparison. From the obtained results, it is clear that d'_{dilate} to a large extent follows the movement of a single and multiple molecules for the majority of frames. To determine the most appropriate support for the structuring function, we compute the coefficient of determination, R^2 , for distance values obtained by a structuring element and the true euclidean distance values. The computed R^2 measure amounts respectively 0.8311, 0.8356, 0.8151, 0.8070 and 0.7938 for $1 \times 1 px$, $3 \times 3 px$, $5 \times 5 px$, $15 \times 15 px$ and $31 \times 31 px$ support for structuring function. We conclude that the most appropriate support is $3 \times 3 px$ and that d'_{dilate} explains the variation of euclidean distance to a high degree as R^2 reaches 0.8356.

For an illustration, we name a few frames at which d'_{dilate} follows the movements of one or two particles to a large extent: (i) a large movement for both molecules as can be seen between frames 10 and 11; (ii) when one molecule disappears as can be seen for frames 26 and 27, i.e., a molecule at the bottom of the image vanishes; (iii) a larger movement of one molecule between frames 74 and 75; and (iv) when both molecules vanishes (frames 82 and 83) for the rest of the movie only the background noise is present in the image and the d'_{dilate} is on the average smaller than in the rest of the movie.

On the other hand, d_{dilate} does not follow the motion of molecules. This behavior is depicted in Figure 4.13 where, both, the Euclidean distance and d_{dilate} are normalized to the interval $[0, 1]$. As the size of molecules is small and ranges approximately $6 - 9 px$, lower values in images reach higher in one or two dilation steps and d_{dilate} completely fails for this particular task. The R^2 measure is 0.2427 for $3 \times 3 px$ structuring element, while d'_{dilate} becomes constant for $5 \times 5 px$ structuring element failing to discern between consecutive frames.

Obtained results clearly show that d_{dilate} cannot be used for this purpose, while the newly proposed d'_{dilate} is applicable to the problem of single molecule tracking. Single particle tracking is a complex problem composed of several steps and its solution is beyond the scope of this paper. Herein, we show that d'_{dilate} has a potential to be applied to challenging real problems. A benefit of using d'_{dilate} for this particular purpose is, for example, when movements in a specific direction should be followed. The proposed distances can easily be adjusted to be more sensitive to movements in a specific direction by choosing a suitable structuring element.

4.5.3 Satellite images

Morphological concepts and morphological distances are proved highly successful in geographical information science for comparing specific phenomena based on their

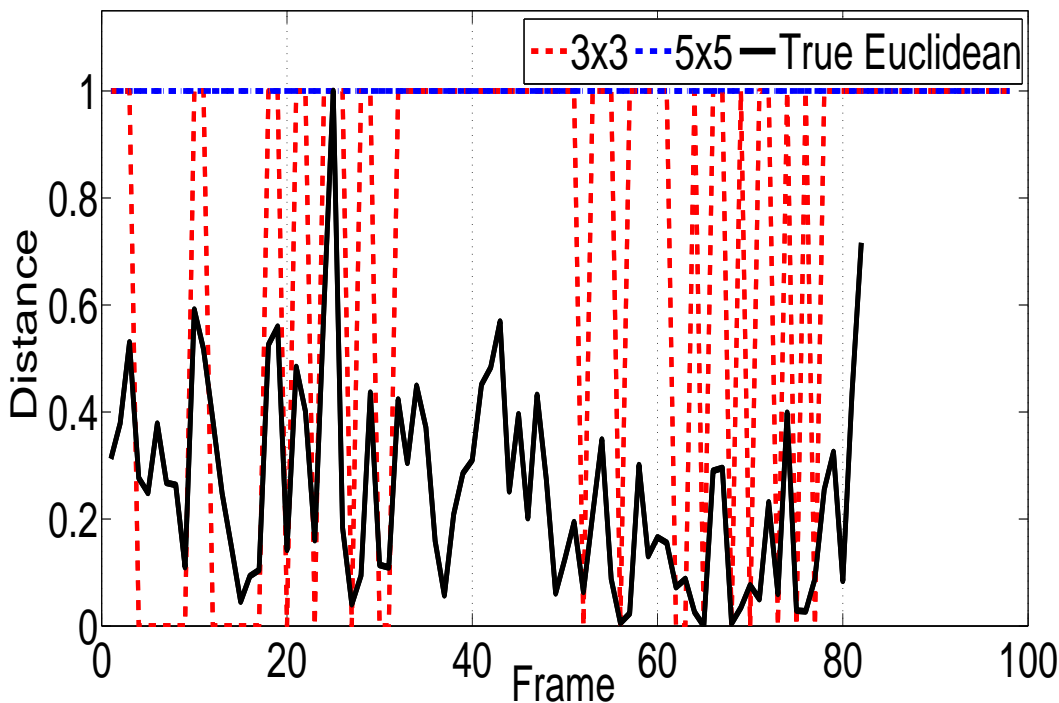


Figure 4.13: The d_{dilate} between consecutive frames for structuring elements 3×3 and 5×5 versus the Euclidean (true) distance between the position of molecules for all frames. Increasing the size of structuring elements lead to the same results as presented for 5×5 .

digital image representation [90, 92–94]. We evaluate them on satellite images of separation of a large iceberg from Larsen-C Ice Shelf taken from a digital surface model. The model is constructed by the Japan Aerospace Exploration Agency (JAXA) and is publicly available at <http://www.eorc.jaxa.jp> [50]. The images f_1, f_2, f_3, f_4 of separating iceberg on different dates (time frames) are given in Figure 4.14. The physical phenomena of interest are cracking of the ice across the ice shelf and movements of the iceberg. Consequently, a distance used for comparison should be sensitive to these changes. In order to easily follow the behavior of a distance with the changes, we give short description of the process from [50]. The trace of a crack occurs in Figure 4.14(a). In Figure 4.14(b) the crack expands in the vertical direction and iceberg separates from its shelf. The iceberg moves to the left slightly narrowing the crack in Figure 4.14(c) because the sea ice was thickening in the period between frames pushing the iceberg. As the sea ice thins, the crack strongly expands and the iceberg moves toward the sea in

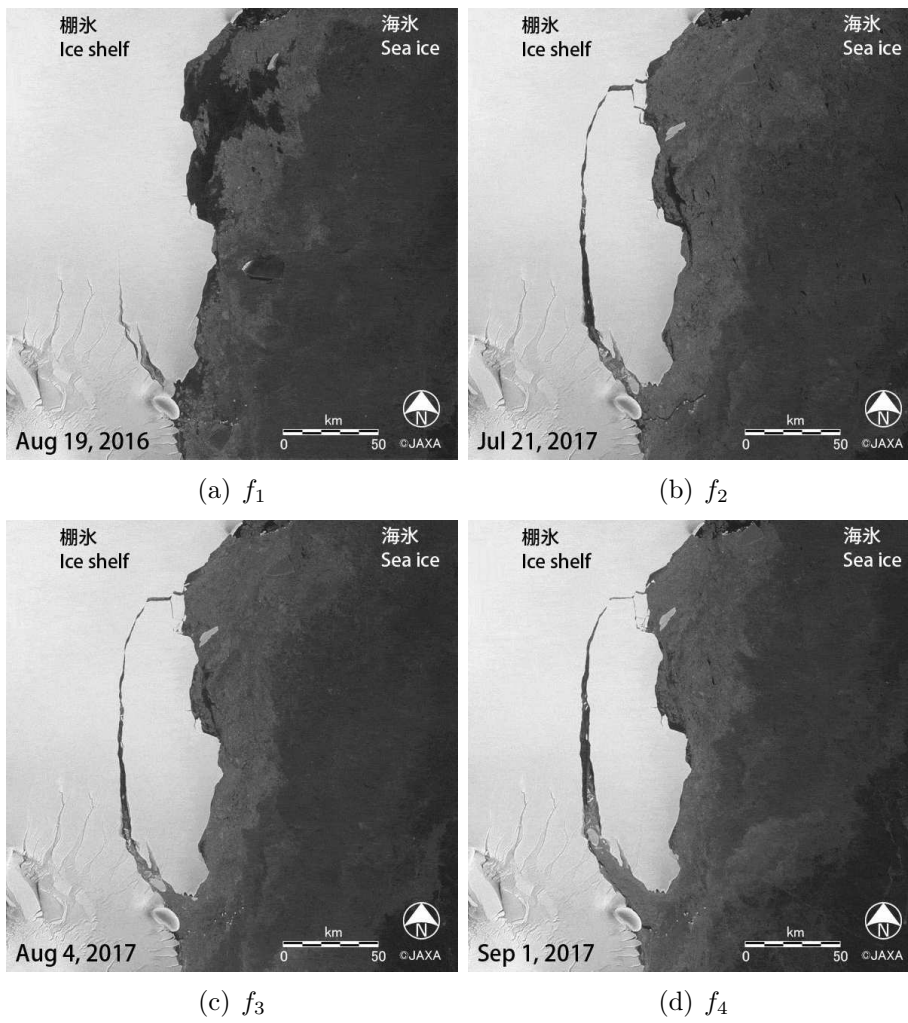


Figure 4.14: Four image frames of separation of a large iceberg from Larsen-C Ice Shelf

Figure 4.14(d) representing the last frame.

We compute L_1 , d_{erode} , d_H , d_D and d'_{dilate} for every pair of frames. To compute morphological distances, we use 3×3 flat structuring element. We use euclidean L_2 distance between points to compute d_H and fuzzyfication in accordance with Equation 2.34 to compute set distances on gray scale images, where α -cuts are observed over all 256 gray levels. To simplify comparison, we normalize obtained values for every distance to the interval $[0, 1]$. The results for d_{SPD} , d_{erode} , d_H , d_D are given in Figure 4.15.

From 4.15(a), we conclude that the differences in pixels values across spatial coordinates follow well the phenomena of interest and provide useful information on

L_1	f_1	f_2	f_3	f_4
f_1	0	0.81	0.77	1
f_2	0.81	0	0.55	0.83
f_3	0.77	0.55	0	0.72
f_4	1	0.83	0.72	0

(a) d_{SPD}

d_{erode}	f_1	f_2	f_3	f_4
f_1	0	0.67	0.33	1
f_2	0.67	0	0.33	0.33
f_3	0.33	0.33	0	0.33
f_4	1	0.33	0.33	0

(b) d_{erode}

d_H	f_1	f_2	f_3	f_4
f_1	0	0.86	0.64	1
f_2	0.86	0	0.50	0.91
f_3	0.64	0.50	0	0.84
f_4	1	0.91	0.84	0

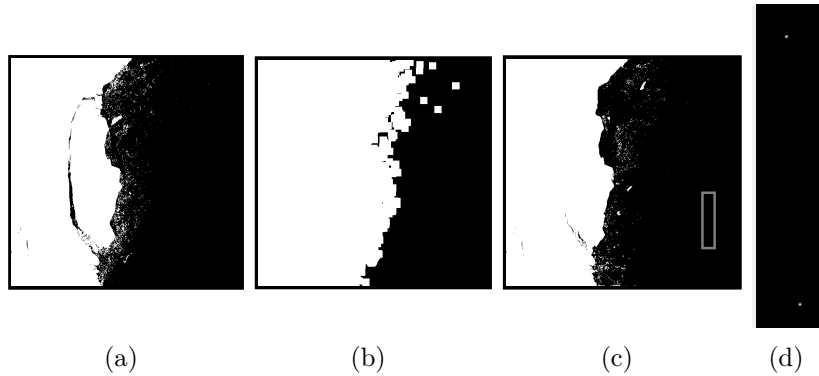
(c) d_H

d_D	f_1	f_2	f_3	f_4
f_1	0	0.69	0.58	0.76
f_2	1	0	0.63	0.84
f_3	0.91	0.54	0	0.89
f_4	0.91	0.73	0.65	0

(d) d_D

Figure 4.15: Different distances computed for image frames from Figure 4.14

changes. For instance, f_1 is at the largest distance from f_4 , then from f_2 and then from f_3 . Still, the pixels values of f_2 are more similar to f_1 than to f_4 , mainly due to non relevant pixels representing open sea. Due to this, $d_{SPD}(f_1, f_2) < d(f_2, f_4)$ neglecting the occurrence of the crack. The same problem is present for d_H and cannot be overcome using any of these two distances. d_{erode} before normalization takes values 1, 2, 3, 4 showing very low sensibility to changes. It completely fails to provide any information on f_3 . The question is whether we can adjust a distance to be more sensitive to the appearance of the cracks than on the differences in the gray values.

Figure 4.16: (a) An α -cut of f_2 and (b) its 10 dilations. After these dilations, the same α -cut of f_1 given in (c) is not covered due to small points in the region framed by rectangle and given in (d) enlarged

d'_{dilate}	f_1	f_2	f_3	f_4
f_1	0	0.89	0.85	1
f_2	0.89	0	0.69	0.88
f_3	0.85	0.69	0	0.80
f_4	1	0.88	0.80	0

(a)

d'_{dilate}	f_1	f_2	f_3	f_4
f_1	0	0.85	0.81	1
f_2	0.85	0	0.64	0.87
f_3	0.81	0.64	0	0.77
f_4	1	0.87	0.77	0

(b)

Figure 4.17: d'_{dilate} for constant structuring function on 3×3 flat structuring element ((a)) and 3×1 flat structuring element ((b))

Observing rows in table presented in Figure 4.15(d) we conclude that values of d_D follow the process in the preferable manner in the sense that the highest values are $d_D(f_i, f_1)$, $i \in \{2, 3, 4\}$. The opposite conclusion is made if we observe columns as d_D is not symmetric. This asymmetry means that ${}^\alpha f_2$ should much more be dilated to cover ${}^\alpha f_1$ than vice versa for majority of α -cuts. In sequel, we briefly discuss the reason for asymmetry in more details, and show that d_D cannot be used to make relevant conclusions.

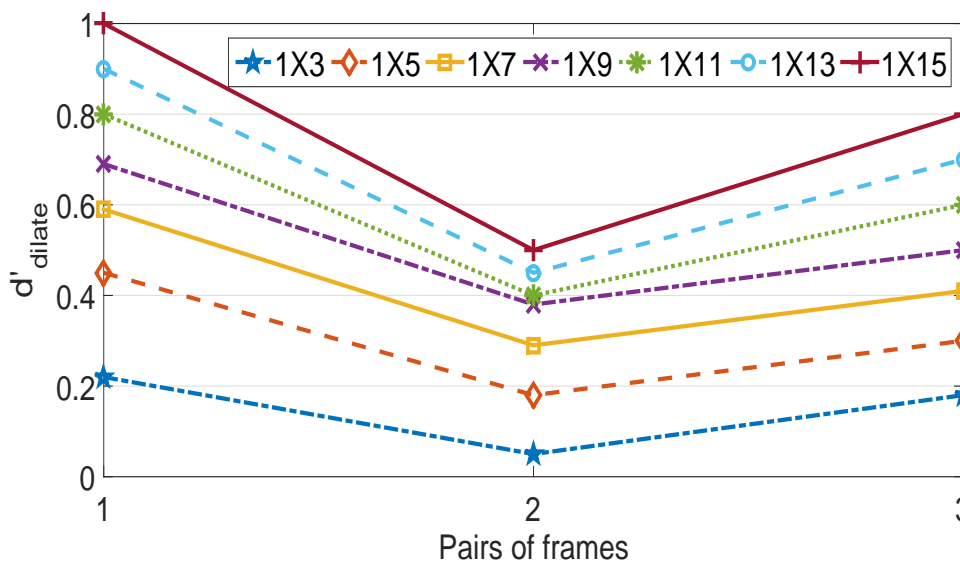


Figure 4.18: d'_{dilate} between consecutive frames for $1 \times 3, 1 \times 5, \dots, 1 \times 15$ structuring element

To illustrate the computation of $d_D(f_2, f_1)$ we give Figure 4.16 where ${}^\alpha f_2$ and ${}^\alpha f_1$ are given for $\alpha = 100$ in Figure 4.16(a) and Figure 4.16(c), respectively. In Figure 4.16(b) is given ${}^\alpha f_2 \oplus 10O$, where O is the used structuring element for

which is valid ${}^{\alpha}f_2 \oplus 10O \not\geq^{\alpha} f_1$. High values of $d_D(f_i, f_1)$, $i \in \{1, 2, 3\}$, leading to conclusion that it is strongly affected by the crack, are due to small points representing sea ice which are not visible in the figure. The points are in the area marked with rectangle in Figure 4.16(c). The enlarged area is given in Figure 4.16(d) where two white pixels on which $d_D(f_i, f_1)$ exclusively depends are visible. We emphasize that it is not possible to overcome the problem by choosing any structuring element.

Now, let us consider Figure 4.17 where the results for d'_{dilate} are given. d'_{dilate} ranks pairs of frames as preferred when 3×3 flat structuring element and a constant structuring function is used. For 3×1 flat structuring element, it ranks pairs the same as d_{SPD} because is less sensitive to vertical changes.

If we want to make d'_{dilate} more sensitive to the vertical crack, we can use structuring element of the size $1 \times 3, 1 \times 5, \dots, 1 \times 15$. In Figure 4.18 we give results for these sizes of structuring element for d'_{dilate} between consecutive frames. The results show that the enlargement of structuring element causes d'_{dilate} to be more sensitive to changes, at the same time following them properly. $d'_{dilate}(f_1, f_2) > d'_{dilate}(f_3, f_4) > d'_{dilate}(f_2, f_3)$ indicating the strongest change when the ice shelf cracks, then weaker change comparing to that when the iceberg made a larger move and the weakest when the ice shelf made a small move.

Chapter 5

Conclusion and discussion

The focus of the thesis has been on improving utilization of the digital image data for comparing objects based on their shape. We considered both tasks crucial for comparing objects from their digital image representations: shape quantification and comparing complete image data comprising shape.

Results provided in Chapter 3 support the idea that the theoretical framework and practical methods developed for utilizing pixel coverage by an object can be used to overcome problems of lacking precision and accuracy resulting from binary approaches in shape analysis. Presented method for estimation of Feret's diameter from digital image representation developed in this framework reduces the maximal absolute error of estimation. Particular weight is in the high reduction of the error observed in real imaging conditions as well as on synthetically generated data. The maximal absolute error over different positions is reduced on average 174 times when estimated for different sizes of synthetically generated ellipses. For low resolution microscopic images of cells, mean square error is reduced 5.96 times on the average and the presented method performs better at the lowest magnification than the evaluated binary method at the highest evaluated magnification. Besides the high reduction of the maximal absolute error, usability of the obtained results contribute the fact that Feret's diameter, as an basic shape property, can be used for computing a number of shape descriptors used in shape analysis. Classic diameter, perimeter and elongation are just some of them.

Evaluation of the performance of the proposed method in combination with different curvature estimators is worth further exploration. Also, the obtained results clearly indicate that the better performance of all the shape descriptors computed from Feret's diameter can be achieved and their usage in practical applications should be explored.

The distances proposed in Chapter 4 are a significant step in adjusting distances to a certain geometrical property of shapes under consideration. Although the idea of extraction of relevant geometrical structure from an image by choosing

a structuring element arises naturally when comparing complete image data comprising shape, the existing morphological distances have strong deficiencies that prevent their more extensive usage. The deficiencies of d_H and d_D related to sensitivity to outliers is resolved by proposing d_{dilate} . However, we prove Proposition 4.3.1 from which follows that d_{dilate} can not be computed for a large number of pairs of digital images. Also, we show on toy examples, synthetic and real data that it is possible that dissimilarity between objects which are compared grows strongly, while the value of d_{dilate} does not change. The distances proposed in Chapter 4 resolve the described problems. They are less sensitive to outliers and more to relevant data in digital images and their value increase with increasing dissimilarity between objects. At the same time they provide higher possibility than the other morphological distances to be adjusted to a certain shape property by choosing a structuring element. The improvement is confirmed on toy examples and synthetic and real data.

The concept presented in Chapter 4 provides many directions that are worth further exploration. In particular, it would be interesting to explore selection of values of structuring function to deal with different image properties created by imaging conditions. The selection of a structuring function for every concrete application is a separate issue. Also, a concrete selection of a structuring function for every concrete application is a separate problem. As our distances have the ability of adjustment to a specific situation, usage of machine learning methods for this purpose is a good possibility.

Bibliography

- [1] J. Angulo. Morphological bilateral filtering and spatially-variant adaptive structuring functions. In *Proceedings of the International Symposium on Mathematical Morphology*, pages 212–223. Springer, Berlin, 2011.
- [2] J. Angulo and S. Velasco-Forero. Stochastic morphological filtering and bellman-maslov chains. In *Proceedings of the International Symposium on Mathematical Morphology*, pages 171–182. Springer, 2013.
- [3] E. Aptoula and S. Lefèvre. A comparative study on multivariate mathematical morphology. *Pattern Recognition*, 40(11):2914–2929, 2007.
- [4] V. Berinde and M. Pacurar. The role of the Pompeiu-Hausdorff metric in fixed point theory. *Creative Mathematics Informatics*, 22(2):35–42, 2013.
- [5] S. Beucher, J. M. Blosseville, and F. Lenoir. Traffic spatial measurements using video image processing. In *Proc.SPIE*, volume 0848, 1988.
- [6] S. Bhardwaj and A. Mittal. A survey on various edge detector techniques. *Procedia Technology*, 4:220 – 226, 2012.
- [7] I. Biederman. Recognition-by-components: A theory of human image understanding. *Psychological Review*, 94:115–147, 1987.
- [8] I. Biederman and G. Ju. Surface versus edge-based determinants of visual recognition. *Cognitive Psychology*, 20(1):38–64, 1988.
- [9] T. Birsan and D. Tiba. One hundred years since the introduction of the set distance by Dimitrie Pompeiu. In *Proceedings of System Modeling and Optimization*, pages 35–39. Springer, 2006.
- [10] A. Bogomolny. On the perimeter and area of fuzzy sets. *Fuzzy Sets and Systems*, 23(2):257 – 269, 1987.

- [11] N. Bouaynaya and D. Schonfeld. Theoretical foundations of spatially-variant mathematical morphology part ii: Gray-level images. *IEEE Transactions on Pattern Analysis and Machine Intelligence*, 30(5):837–850, 2008.
- [12] J. Chanussot, I. Nyström, and N. Sladoje. Shape signatures of fuzzy star-shaped sets based on distance from the centroid. *Pattern Recognition Letters*, 26(6):735 – 746, 2005.
- [13] N. Chenouard, I. Smal, F. De Chaumont, M. Maška, I. F. Sbalzarini, Y. Gong, J. Cardinale, C. Carthel, S. Coraluppi, M. Winter, et al. Objective comparison of particle tracking methods. *Nature Methods*, 11(3):281–289, 2014.
- [14] K. C. Ciesielski, X. Chen, J. Udupa, and G. Grevera. Linear time algorithms for exact distance transform. *Journal of Mathematical Imaging and Vision*, 39(3):193–209, 2011.
- [15] K. C. Ciesielski, R. Strand, F. Malmberg, and P. Saha. Efficient algorithm for finding the exact minimum barrier distance. *Computer Vision and Image Understanding*, 123:53–64, 2014.
- [16] D. Coeurjolly and R. Klette. A comparative evaluation of length estimators of digital curves. *IEEE Transactions on Pattern Analysis and Machine Intelligence*, 26(2):252–258, 2004.
- [17] D. Coeurjolly, J.-Q. Lachaud, and T. Roussillon. Multigrid convergence of discrete geometric estimators. In *Digital Geometry Algorithms. Theoretical Foundations and Applications to Computational Imaging*, pages 395–424. Springer, 2012.
- [18] O. Cuisenaire. Locally adaptable mathematical morphology using distance transformations. *Pattern Recognition*, 29(3):405–416, 2006.
- [19] V. Čurić. *Distance Functions and Their Use in Adaptive Mathematical Morphology*. PhD thesis, Uppsala University, 2014.
- [20] V. Čurić and C. L. Hendriks. Saliency adaptive structuring elements. *IEEE Journal of Selected Topics in Signal Processing*, 6(7):809 – 819, 2012.
- [21] V. Čurić, A. Landström, M. J. Thurley, and C. L. Hendriks. Adaptive mathematical morphology - A survey of the field. *Pattern Recognition Letters*, 47:18 – 28, 2014.

- [22] V. Čurić, J. Lindblad, and N. Sladoje. Distance measures between digital fuzzy objects and their applicability in image processing. In *14th International Workshop on Proceedings of Combinatorial Image Analysis, IWCIA 2011*, pages 385–395. LCNS, Springer, 2011.
- [23] J. Debayle and J. Pinoli. General adaptive neighborhood image processing part i: Introduction and theoretical aspects. *Journal of Mathematical Imaging and Vision*, 25(2):195–222, 2006.
- [24] J. Debayle and J. C. Pinoli. Spatially adaptive morphological image filtering using intrinsic structuring elements. *Image Analysis & Stereology*, 24(3):145–158, 2005.
- [25] M. M. Deza and E. Deza. *Encyclopedia of Distances*. Springer Verlag Berlin Heidelberg, 2009.
- [26] S. Dražić. Advanced morphological distances based on dilation and erosion. *Fundamenta Informaticae*. Accepted.
- [27] S. Dražić, J. Lindblad, and N. Sladoje. Precise estimation of the projection of a shape from a pixel coverage representation. In *Proceedings of International Symposium on Image and Signal Processing and Analysis*, pages 569–574. IEEE, 2011.
- [28] S. Dražić, J. Lindblad, and N. Sladoje. Estimation of Feret’s diameter from pixel coverage representation of a shape. *Pattern Recognition Letters*, 80:37–45, 2016.
- [29] B. N. Duncan, A. I. Prados, L. N. Lamsal, Y. Liud, D. G. Streetse, P. Gupta, E. Hilsenrathb, R. A. Kahn, J. E. Nielseng, A. J. Beyersdorfh, S. P. Burtonh, A. M. Fiorei, J. Fishmanj, D. K. Henzek, C. A. Hostetlerh, N. A. Krotkova, P. Leel, M. Linn, S. Pawsona, G. Pfistern, K. E. Pickeringa, R. B. Pierceo, Y. Yoshida, and L. D. Ziembah. Satellite data of atmospheric pollution for U.S. air quality applications: Examples of applications, summary of data end-user resources, answers to faqs, and common mistakes to avoid. *Atmospheric Environment*, 94:647–662, 2014.
- [30] T. Eiter and H. Mannila. Distance measures for point sets and their computation. *Acta Informatica*, 34(2):109–133, 1997.
- [31] A. X. Falcao, J. Stolfi, and R. D. A. Lotufo. The image foresting transform: Theory, algorithms, and applications. *IEEE Transactions on Pattern Analysis and Machine Intelligence*, 26(1):19–29, 2004.

- [32] J. Fan, G. Zeng, M. Body, and M. S. Hacid. Seeded region growing: an extensive and comparative study. *Pattern Recognition Letters*, 26(8):1139 – 1156, 2005.
- [33] C. Fouard and M. Gedda. An objective comparison between gray weighted distance transforms and weighted distance transforms on curved spaces. In *Proceedings of Discrete Geometry for Computer Imagery*, volume 4245, pages 259–270. LNCS, Springer, 2006.
- [34] V. D. Gesù and V. Starovoitov. Distance-based functions for image comparison. *Pattern Recognition Letters*, 20(2):207 – 214, 1999.
- [35] M. Ginovart, R. Carbó, M. Blanco, and X. X. Portell. Digital image analysis of yeast single cells growing in two different oxygen concentrations to analyze the population growth and to assist individual-based modeling. *Frontiers in Microbiology*, 8:2628–2649, 2018.
- [36] R. C. Gonzalez and R. E. Woods. *Digital Image Processing*. Addison-Wesley Longman Publishing Co., Inc., Boston, MA, USA, 2001.
- [37] J. A. Goode and M. B. Matson. Embolisation of cancer: what is the evidence? *Cancer Imaging*, 4(2):133–141, 2004.
- [38] F. Hausdorff. *Grundzüge der mengenlehre*, 1914. Viet. Leipzig.
- [39] W. G. Hayward. Effects of outline shape in object recognition. *Journal of Experimental Psychology: Human Perception and Performance*, 24(2):427–440, 1998.
- [40] H. J. A. M. Heijmans and P. Meer. *Shape in Picture: Mathematical Description of Shape in Grey-level Images*. Springer Berlin Heidelberg, Berlin, DE, 1994.
- [41] H. J. A. M. Heimans and C. Ronse. The algebraic basis of mathematical morphology. i. dilations and erosions. *Comput. Vision Graph. Image Process.*, 50(3):245–295, 1990.
- [42] C. Hendriks Luengo, L. van Vliet, B. Rieger, G. van Kempen, and M. van Ginkel. *DIPimage: a scientific image processing toolbox for MATLAB. Quantitative Imaging Group, Faculty of Applied Sciences. Delft, The Netherlands: Delft University of Technology*, 2015.
- [43] H. J. A. M. Heumans, P. Nacken, A. Toet, and L. Vincent. Graph morphology. *Journal of Visual Communication and Image Representation*, 3(1):24–38, 1992.

- [44] B. Hubbard, A. Luckman, D. W. Ashmore, K. Bernd, P. K. Munneke, M. Philippe, D. Jansen, A. Booth, H. Sevestre, J. L. Tison, M. O’Leary, and I. Rutt. Massive subsurface ice formed by refreezing of ice-shelf melt ponds. *Nature Communications*, 9, 2016.
- [45] A. Huhle, D. Klaue, H. Brutzer, P. Daldrop, S. Joo, O. Otto, U. F. Keyser, and R. Seidel. Camera-based three-dimensional real-time particle tracking at khz rates and Ångström accuracy. *Nature Communications*, 6, 2017.
- [46] M. N. Huxley. Exponential sums and lattice points. In *Proceedings of the London Mathematical Society*, pages 471 – 502. Oxford University Press, 1990.
- [47] M. N. Huxley and J. Žunić. *On the Number of Digitizations of a Disc Depending on Its Position*, pages 219–231. Springer Berlin Heidelberg, 2005.
- [48] C. Igathinathane, S. Melin, S. Sokhansanj, X. Bi, C. Lim, L. Pordesimo, and E. Columbus. Machine vision based particle size and size distribution determination of airborne dust particles of wood and bark pellets. *Powder Technology*, 196(2):202–212, 2009.
- [49] V. Ilić, J. Lindblad, and N. Sladoje. Signature of a shape based on its pixel coverage representation. In *Proceedings of 19th International Conference on Discrete Geometry for Computer Imagery, DGCI 2016*, pages 181–193. LCNS, Springer, 2016.
- [50] Japan Aerospace Exploration Agency. JAXA Global ALOS portal. <http://www.eorc.jaxa.jp/>. Last accessed: April 2018.
- [51] S. B. Joshi, T. Okabe, R. O. Roswell, G. Weissman, C. F. Lopez, J. Lindsay, A. D. Pichard, N. J. Weissman, R. Waksman, and W. G. Weigold. Accuracy of computed tomographic angiography for stenosis quantification using quantitative coronary angiography or intravascular ultrasound as the gold standard. *American Journal of Cardiology*, 104(8):1047–1051, 2009.
- [52] J. Ju, E. D. Kolaczyk, and S. Gopal. Gaussian mixture discriminant analysis and sub-pixel land cover characterization in remote sensing. *Remote Sensing of Environment*, 84(4):550 – 560, 2003.
- [53] V. V. Kindratenko. On using functions to describe the shape. *Journal of Mathematical Imaging and Vision*, 18(3):225–245, 2003.
- [54] N. Kiryati and A. Bruckstein. Gray-levels can improve the performance of binary image digitizers. In *Computer Vision and Pattern Recognition, 1988*.

- Proceedings CVPR '88., Computer Society Conference on*, pages 562–567, 1988.
- [55] R. Klette and A. Rosenfeld. *Digital Geometry: Geometric Methods for Digital Picture Analysis*. Elsevier, 2004.
- [56] R. Klette and J. Žunić. Errors in calculated moments of convex sets using digital images. In *Proceedings of SPIE's International Symposium on Optical Science, Engineering and Instrumentation*, pages 3811 – 3811. SPIE, 1999.
- [57] R. Klette and J. Žunić. ADR shape descriptor - distance between shape centroids versus shape diameter. *Computer Vision and Image Understanding*, 116(6):690 – 697, 2012.
- [58] R. Klette and J. Žunić. Multigrid convergence of calculated features in image analysis. *Journal of Mathematical Imaging and Vision*, 13(3):173–191, 2000.
- [59] B. Kulesa, D. Jansen, A. J. L. E. C. King, and P. Sammonds. Marine ice regulates the future stability of a large antarctic ice shelf. *Nature Communications*, 5, 2014.
- [60] B. Landau, L. Smith, and S. Jones. Object shape, object function, and object name. *Journal of Memory and Language*, 38(1):1–27, 1998.
- [61] K. V. Leemput, F. Maes, D. Vandermeulen, and P. Suetens. A unifying framework for partial volume segmentation of brain mr images. *IEEE Transactions on Medical Imaging*, 22(1):105–119, 2003.
- [62] R. Lerallut, E. Decenciere, and F. Meyer. Image processing using morphological amoebas. In *Proceedings of the International Symposium on Mathematical Morphology*, pages 13–25. Springer, 2005.
- [63] B. Li, E. Chang, and Y. Wu. Discovery of a perceptual distance function for measuring image similarity. *Multimedia Systems*, 8(6):512–522, 2003.
- [64] J. Lindblad and N. Sladoje. Coverage segmentation based on linear unmixing and minimization of perimeter and boundary thickness. *Pattern Recognition Letters*, 33(6):728–738, 2012.
- [65] J. Lindblad and N. Sladoje. Linear time distances between fuzzy sets with applications to pattern matching and classification. *IEEE Transactions on Image Processing*, 23(1):126–136, 2014.
- [66] M. Lindén, V. Ćurić, A. Boucharin, D. Fange, and J. Elf. Simulated single molecule microscopy with smeaol. *Bioinformatics*, 32(15):2394–2395, 2016.

- [67] S. Loncaric. A survey of shape analysis techniques. *Pattern Recognition*, 31(8):983 – 1001, 1998.
- [68] R. B. M. Sonka, V. Hlavac. *Image Processing, Analysis and Machine Vision*. Springer, New York, USA, 1993.
- [69] F. Malmberg, J. Lindblad, N. Sladoje, and I. Nyström. A graph-based framework for sub-pixel image segmentation. *Theoretical Computer Science*, 412(15):1338–1349, 2011.
- [70] M. Marwan, T. Pflederer, T. Schepis, M. Seltmann, D. Ropers, W. G. Daniel, and S. Achenbach. Coronary vessel and luminal area measurement using dual-source computed tomography in comparison with intravascular ultrasound: Effect of window settings on measurement accuracy. *Journal of Computer Assisted Tomography*, 35(1):113 – 118, 2011.
- [71] G. Matheron. *Random Sets and Integral Geometry*. Willey, New York, NY, USA, 1975.
- [72] G. H. Merkus. *Particle size measurements: Fundamentals, Practice, Quality*, volume 17. Springer, New York, USA, 2009.
- [73] W. J. Meyer and H. Minkowski. *Minkowski addition of convex sets*. University of Wisconsin–Madison, Madison, WI, USA, 1969.
- [74] J. Moosman, A. Ershov, V. Altapova, T. Baumbach, M. S. Prasad, C. Labonne, X. Xiao, J. Kashef, and R. Hofmann. X-ray phase-contrast in vivo microtomography probes new aspects of xenopus gastrulation. *Nature*, 497(7449):374–377, 2013.
- [75] J. J. Moreau. Fonctionnelles convexes. *Seminaire Jean Leray*, 2:1–108, 1966–1967.
- [76] K. I. Mortensen, L. S. Churchman, J. A. Spudich, and H. Flyvbjerg. Optimized localization analysis for single-molecule tracking and super-resolution microscopy. *Nature Methods*, 7(5):377–381, 2010.
- [77] R. Moshavegh, B. E. Bejnordi, A. S. Mehnert, P. Malm, and E. Bengtsson. Automated segmentation of free-lying cell nuclei in pap smears for malignancy-associated change analysis. In *Proceedings of Annual International Conference of the Engineering in Medicine and Biology Society, EMBC*, pages 5372–5375. IEEE, 2012.

- [78] W. J. Niessen, K. L. Vincken, J. Weickert, B. M. T. H. Romeny, and M. A. Viergever. Multiscale segmentation of three-dimensional mr brain images. *International Journal of Computer Vision*, 31(2-3):185–202, 1999.
- [79] I. Niiniluoto. *Truthlikeness*. Springer Netherlands, Dordrecht, NL, 1987.
- [80] J. Ning, L. Zhang, D. Zhang, and C. Wu. Interactive image segmentation by maximal similarity based region merging. *Pattern Recognition*, 43(2):45 – 456, 2010.
- [81] T. Pavlidis. *Algorithms for graphics and image processing*, volume 1. Computer Science Press, Rockville, USA, 1982.
- [82] D. Pompeiu. *Sur la continuité des fonctions de variables complexes*. PhD thesis, Faculté des sciences de Toulouse, 1905.
- [83] J. Rodernik. Adaptivity and group invariance in mathematical morphology. In *Proceedings of International Conference on Image Processing*, pages 2253–2256. IEEE, 2009.
- [84] C. Ronse and M. Tajine. Discretization in hausdorff space. *Journal of Mathematical Imaging and Vision*, 12:219–242, 2000.
- [85] A. Rosenfeld. The fuzzy geometry of image subsets. *Pattern Recognition Letters*, 2(5):311 – 317, 1984.
- [86] P. L. Rosin. Techniques for assessing polygonal approximations of curves. *IEEE Transactions on Pattern Analysis and Machine Intelligence*, 19(6):659–666, 1997.
- [87] P. L. Rosin and C. L. Mumford. A symmetric convexity measure. *Computer Vision and Image Understanding*, 103(2):101–111, 2006.
- [88] P. L. Rosin and J. Žunić. Measuring squareness and orientation of shapes. *Journal of Mathematical Imaging and Vision*, 39(1):13–27, 2011.
- [89] P. L. Rosin and J. D. Žunić. Measuring rectilinearity. *Computer Vision and Image Understanding*, 99(2):175–188, 2005.
- [90] B. S. D. Sagar. Visualization of spatiotemporal behavior of discrete maps via generation of recursive median elements. *IEEE Transactions on Pattern Analysis and Machine Intelligence*, 32(2):378–384, 2010.
- [91] B. S. D. Sagar and S. L. Lim. Morphing of grayscale DEMs via morphological interpolations. *IEEE Journal of Selected Topics in Applied Earth Observations and Remote Sensing*, 8(11):5190–5198, 2015.

- [92] B. S. D. Sagar and S. L. Lim. Ranks for pairs of spatial fields via metric based on grayscale morphological distances. *IEEE Transactions on Image Processing*, 24(3):908–918, 2015.
- [93] B. S. D. Sagar, N. Rajesh, S. A. Vardhan, and P. Vardhan. Metric based on morphological dilation for the detection of spatially significant zones. *IEEE Geoscience and Remote Sensing Letters*, 10(3):500–504, 2013.
- [94] B. S. D. Sagar and J. Serra. Spatial information retrieval, analysis, reasoning and modelling. *International Journal of Remote Sensing*, 31(22):5747–5750, 2010.
- [95] J. A. Saghri and H. Freeman. Analysis of the precision of generalized chain codes for the representation of planar curves. *IEEE Transactions on Pattern Analysis and Machine Intelligence*, 3(5):533–539, 1981.
- [96] P. K. Saha, F. W. Wehrli, and B. R. Gomberg. Fuzzy distance transform: Theory, algorithms, and applications. *Computer Vision and Image Understanding*, 86(3):171 – 190, 2002.
- [97] P. Salembier. Study on nonlocal morphological operators. In *Proceedings of the International Conference on Image Processing*, pages 2269–2272. IEEE, 2009.
- [98] J. M. Saxton. Single-particle tracking: connecting the dots. *Nature Methods*, 5:671–672, 2008.
- [99] J. M. Saxton. A particle tracking meet. *Nature Methods*, 11:247–248, 2014.
- [100] F. Schaff, M. Bech, P. Zaslansky, C. Jud, M. Liebi, M. Guizar-Sicairos, and F. Pfeiffer. Six-dimensional real and reciprocal space small-angle x-ray scattering tomography. *Nature*, 527(7578):353–356, 2015.
- [101] J. Serra. Les structures gigognes: morphologie mathématique et interprétation métallogénique". *Mineralium Deposita*, 3(2):135–154, 1968.
- [102] J. Serra. *Image Analysis and Mathematical Morphology*. Academic Press, Inc., London, UK, 1982.
- [103] J. Serra. Hausdorff distances and interpolations. In *Proceedings of the Fourth International Symposium on Mathematical Morphology and Its Applications to Image and Signal Processing*, pages 107–114. Kluwer Academic Publishers, 1998.

- [104] M. Sezgin and B. Sankur. Survey over image thresholding techniques and quantitative performance evaluation. *Journal of Electronic Imaging*, 13:146–165, 2004.
- [105] N. Sladoje. *On Analysis of Discrete Spatial Fuzzy Sets in 2 and 3 Dimensions*. PhD thesis, Swedish University of Agricultural Sciences, Centre for Image Analysis Uppsala, 2005.
- [106] N. Sladoje and J. Lindblad. *Estimation of Moments of Digitized Objects with Fuzzy Borders*, pages 188–195. Springer Berlin Heidelberg, 2005.
- [107] N. Sladoje and J. Lindblad. High-precision boundary length estimation by utilizing gray-level information. *IEEE Transactions on Pattern Analysis and Machine Intelligence*, 31(2):357–363, 2009.
- [108] N. Sladoje and J. Lindblad. Pixel coverage segmentation for improved feature estimation. In *Proceedings of International Conference on Image Analysis and Processing*, volume 5716, pages 929–938. LNCS, Springer, 2009.
- [109] N. Sladoje and J. Lindblad. The coverage model and its use in image processing. In *Selected Topics on Image Processing and Cryptology (Ed. Miodrag Mihaljević), Zbornik radova (Collection of Papers)*, volume 15, pages 39–117. Mathematical Institute of the Serbian Academy of Sciences and Arts, Belgrade, Serbia, 2012.
- [110] N. Sladoje, I. Nyström, and P. K. Saha. Perimeter and area estimations of digitized objects with fuzzy borders. In *Proceedings of 11th International Conference on Discrete Geometry for Computer Imagery, DGCI 2003*, pages 368–377. LCNS, Springer, 2003.
- [111] N. Sladoje, I. Nyström, and P. K. Saha. Measurements of digitized objects with fuzzy borders in 2d and 3d. *Image and Vision Computing*, 23(2):123 – 132, 2005.
- [112] F. Sloboda, B. Zařko, and J. Stoer. *Advances in Digital and Computational Geometry*, chapter On approximation of planar one-dimensional continua. Springer, Singapore, 1998.
- [113] C. S. Smith, N. Joseph, B. Rieger, and K. A. Lidke. Fast, single-molecule localization that achieves theoretically minimum uncertainty. *Nature Methods*, 7(5):373–375, 2010.
- [114] P. Soille. *Morphological Image Analysis: Principles and Applications*. Springer Verlag New York, Inc., Secaucus, NJ, USA, 2003.

- [115] P. Stähr, H. J. Ruprecht, T. Voigtländer, P. Kearney, R. Erbel, L. Koch, S. Krass, R. Brennecke, and J. Meyer. Importance of calibration for diameter and area determination by intravascular ultrasound. *The International Journal of Cardiovascular Imaging*, 12(4):221 – 230, 1996.
- [116] V. Starovoitov. Towards a measure of diversity between grey-scale images. In *Proceedings of International Conference on Computer Analysis of Images and Patterns*, pages 14–221. Springer, Berlin, Heidelberg, 1995.
- [117] P. Stelldinger. Topologically correct surface reconstruction using alpha shapes and relations to ball-pivoting. In *Proceedings of 19th International Conference on Pattern Recognition, ICPR 2008.*, pages 1–4. IEEE, 2008.
- [118] P. Stelldinger and U. Köthe. Towards a general sampling theory for shape preservation. *Image and Vision Computing*, 23(2):237–248, 2005.
- [119] S. R. Sternberg and J. Serra. Grayscale morphology. *Computer Vision, Graphics, and Image Processing*, 35(3):333 – 355, 1986.
- [120] M. Stojmenovic, A. Nayak, and J. Zunic. Measuring linearity of a finite set of points. In *Proceedings of IEEE Conference on Cybernetics and Intelligent Systems*, pages 1–6. IEEE, 2006.
- [121] D. Stoyan and H. Stoyan. *Fractals, random shapes and point fields: methods of geometrical statistics*, volume 1. Wiley, New York, NY, USA, 1995.
- [122] M. Tajine and C. R. *Topological Properties of Hausdorff Discretizations*, pages 41–50. Springer USA, 2000.
- [123] M. T. Tomkowiak, A. N. Raval, M. S. V. Lysel, T. Funk, and M. A. Speidela. Calibration-free coronary artery measurements for interventional device sizing using inverse geometry x-ray fluoroscopy: In vivo validation. In *Proceedings of SPIE—the International Society for Optical Engineering*. International Society for Optical Engineering, 2014.
- [124] S. Velasco-Forero and J. Angulo. On nonlocal mathematical morphology. In *Proceedings of the International Symposium on Mathematical Morphology*, pages 219–230. Springer, 2013.
- [125] J. Verly and R. Delanoy. Adaptive mathematical morphology for range imagery. *IEEE Transactions on Image Processing*, 2(2):272–275, 1993.

- [126] J. Vidal, J. Crespo, and V. Maojo. Recursive interpolation technique for binary images based on morphological median sets. In *Proceedings of International Symposium on Mathematical Morphology: 40 years*, pages 53–56. Springer, 2005.
- [127] L. Vincent. Special issue on advances in mathematical morphology graphs and mathematical morphology. *Signal Processing*, 16(4):365 – 388, 1989.
- [128] A. Žunić. Shape diameter for object analysis. *Information Processing Letters*, 136:76 – 79, 2018.
- [129] J. Wagner and J. MacHer. Automated spore measurements using microscopy, image analysis, and peak recognition of near-monodisperse aerosols. *Aerosol Science and Technology*, 46(8):862–873, 2012.
- [130] W. H. Walton. Feret’s statistical diameter as a measure of particle size. *Nature*, 162:329–330, 1948.
- [131] M. Wang, Z. Zhang, J. Zhu, W. Sheng, P. Lian, F. Liu, S. Cai, and Y. Xu. Tumour diameter is a predictor of mesorectal and mesenteric lymph node metastases in anorectal melanoma. *Colorectal Disease*, 15(9):1086–1092, 2013.
- [132] L. Zadeh. Fuzzy sets. *Information and Control*, 8(3):338 – 353, 1965.
- [133] D. Zhang and G. Lu. Review of shape representation and description techniques. *Pattern Recognition*, 37(1):1 – 19, 2004.
- [134] D. Žunić and J. D. Žunić. Shape ellipticity from hu moment invariants. *Applied Mathematics and Computation*, 226:406–414, 2014.
- [135] J. D. Žunić. Shape descriptors for image analysis. In *Selected Topics on Image Processing and Cryptology (Ed. Miodrag Mihaljević), Zbornik radova (Collection of Papers)*, volume 15, pages 5 – 38. Mathematical Institute of the Serbian Academy of Sciences and Arts, Belgrade, Serbia, 2012.
- [136] J. D. Žunic and P. L. Rosin. A new convexity measure for polygons. *IEEE Transactions on Pattern Analysis and Machine Intelligence*, 26(7):923 – 934, 2004.